UNIVERSITÉ DE LORRAINE NORTHWESTERN POLYTECHNICAL UNIVERSITY

DISSERTATION

Presented at
Université de Lorraine and Northwestern Polytechnical University

Jiangkun FAN 樊江昆

To obtain the doctor's degree of
University of Lorraine and Northwestern Polytechnical University

SPECIAL FIELD: Engineering Sciences
OPTION: Materials Science

Microstructural study of the β→α phase transformation induced by thermo-mechanical treatments in metastable β Ti-5553 alloy

To be defended on the 27th July, 2016 in front of the jury:

Qiaoyan SUN	Professor	Xi'an Jiaotong University, China	Reviewer & Jury member
Werner SKROTZKI	Professor	Technische Universität Dresden, Germany	Reviewer & Jury member
Pingxiang ZHANG	Professor	Northwest Institute for Nonferrous Metal Research, China	Jury member
Tadao WATANABE	Professor	Tohoku University, Japan	Jury member
Claude ESLING	Professor	Université de Lorraine, France	Invited
Jinshan LI	Professor	Northwestern Polytechnical University, China	Supervisor
Yudong ZHANG	Doctor HDR	Université de Lorraine, France	Supervisor
Hongchao KOU	Professor	Northwestern Polytechnical University, China	Co-Supervisor
Lionel GERMAIN	Doctor HDR	Université de Lorraine, France	Co-Supervisor

Laboratoire d'Étude des Microstructures et de Mécanique des Matériaux, LEM3
Ile du Saulcy 57012 Metz Cedex 1

Acknowledgements

This work was financed by the Programme PHC Cai Yuanpei (No. 30249RD) and National Natural Science Foundation of China (No. 51371143). The work presented in this thesis is accomplished at LEM3 (former LETAM, University of Lorraine, France) and the State Key Laboratory of Solidification Processing (Northwestern Polytechnical University, China). I had the honor to work with numerous colleagues in the two laboratories and I would like to give my hearted thanks for their kind help.

First of all, I would like to sincerely thank all the jury members for taking time out of their busy schedules to achieve the defense of my dissertation. Special gratitude to Professor Werner SKROTZKI and Professor Qiaoyan SUN for their evoluation of my dissertation and for the constructive suggestions and comments.

I sincerely extend my deepest gratitude to my advisors, Dr. Yudong Zhang and Dr. Lionel Germain at University of Lorraine, Professor Jinshan Li and Professor Hongchao Kou at Northwestern Polytechnical University, who granted me this project. Without their endless encouragement and support, this work would not have been completed. I have benefited tremendously from their knowledge and experiences, their persistence and strive for excellence. Special thanks to Dr. Yudong Zhang and Professor Jinshan Li for their constant and selfless help in my academic study and daily life.

I would like to express my gratefulness to Professor Claude ESLING and Dr. Nathalie SIREDEY for their helpful and inspiring discussions as they shared their knowledge with me. I also would like to express my gratitude to all the technicians at LEM3 who have offered their technical assistance to my work.

I am grateful to all the staffs and friends who shared their experiences with me and offered helps to my study, including Dr. Zhangzhi SHI, Dr. Yajun ZHAO, Dr. Cai CHEN, Dr. Laurent WEISS, Mr. Haile YAN, Ms. Xiaorui LIU, Ms. Jing WEN, Mr. Shun XU, Mr. Naifu ZOU, Mr. Chunyang ZHANG, Ms. Chunqing LIN and Mr. Ke HUA.

I should finally like to express my gratitude to my beloved parents who have always been helping me out of difficulties and supporting me without a word of complaint and caring me all of my life.

Abstract

Metastable β titanium alloys are important structural materials for aeronautical applications due to their high strength to density ratio, good ductility and workability and excellent hardenability. Despite the efforts in resolving the complex microstructural evolution related to thermomechanical processes and in gaining knowledge on the produced phases and their contribution to the resultant mechanical properties, there are still some controversial and unresolved issues.

The aim of the present PhD work is to determine precisely the metastable nature of β phase and to characterize finely the characteristics of the β→α transformation during high and low temperature thermomechanical treatments. Investigations were performed on a Ti-5553 alloy with the single β phase initial microstructure obtained by solution treatment followed by quenching using scanning and transmission electron microscopy (SEM/TEM) coupled to crystallographic orientation measurements and chemical analyses.

It was demonstrated experimentally that the structure of the β phase in the metastable titanium alloy is not "pure" body centered cubic. Diffraction diagrams presents streaking of the β diffraction spots and additional spots at the 1/2, the 1/3 and 2/3 diffraction positions. Also, striations are observed in TEM images. From this experimental evidence and crystallographic calculations, it was proved that atomic displacements on the $\{110\}_\beta$ and $\{112\}_\beta$ planes formed a structure between that of the parent β phase and that of the α or ω phase, demonstrating pre-phase transformation tendency.

The study of the precipitation during thermomechanical processing at higher temperature in the α+β region revealed that discontinuous equiaxed or short rod shaped α precipitates (1~2μm) mainly form on the high angle and low angle β grain boundaries but seldom in β grain interiors, forming the "necklace" microstructure. The Burgers orientation relationship (BOR) between the α and β phases is destroyed gradually by the deformation. The BOR deviation of grain boundary α is larger than that of intragranular α. The deviation from the BOR increases

both with the increasing strain and decreasing strain rate.

During the deformation at the lower temperature in the α+β region, the α precipitates exhibit different morphologies: such as lamellar α, equiaxed α and irregular α depending on their localization. Within the slip bands, equiaxed α/β grains which do not respect the BOR are present. However, between the bands, lamellar α and β phases maintaining the BOR are distributed alternately. In that last case a strong variant selection is observed as only the two or three variants that form are those which can accommodate the macroscopic deformation. Comparatively, in absence of compression all 12 variants are formed.

The β→α phase transformation is retarded during the hot compression at higher temperature region, which is attributed to the competition between softening and phase transformation. On the contrary, it is promoted during compression at lower temperature region due to the more inducted deformation defects acting as α phase nucleation sites and due to accelerating growth of α precipitates and retarded softening.

Dislocation slip is the leading deformation mechanism for the Ti-5553 alloy. Under the lower temperature deformation condition, single or multiple-slip bands with two or three different activated slip systems would form during the hot deformation process. Identification of these slip systems have been done by trace analysis.

These results provide new insights into the structural nature of β metastable phase and valuable reference for β→α phase transformation during thermo-mechanical treatment in metastable β titanium alloys.

***Keywords**:* Metastable β titanium alloy; Ti-5553; thermo-mechanical treatments; β→α phase transformation; variants selection; crystallography

Résumé

Les alliages de titane β métastables sont des matériaux de structure essentiels pour les applications aéronautiques de part leurs très bonnes propriétés mécaniques. En effet, ils présentent une résistance spécifique élevée, une bonne ductilité et forgeabilité et une excellente réponse aux traitements thermiques. Toutefois, il existe encore aujourd'hui à leur sujet des controverses et des questions ouvertes et ce, malgré les efforts pour comprendre les mécanismes d'évolution microstructurale au cours de traitements thermo-mécaniques et pour déterminer les phases en présence et leur contribution aux les propriétés mécaniques résultantes.

Ce travail de thèse a pour objectif de déterminer la nature de la phase β et de caractériser la transformation β→α à haute et basse températures par des caractérisations fines en microscopie électronique à balayage et à transmission couplées à des mesures d'orientations cristallographiques et de composition chimique. L'alliage étudié est un Ti-5553 avec une microstructure initiale 100% β obtenue par mise en solution et trempe.

Il a été démontré expérimentalement que la structure de la phase β métastable n'est pas purement cubique centrée. Les points de la phase β dans les clichés de diffraction présentent un allongement (streaking) et des points supplémentaires sont visibles aux positions de diffraction 1/2, 1/3 et 2/3. Par ailleurs, les images MET ont un aspect en moiré. A partir de ces résultats et de calculs crystallographiques, il a été prouvé que des déplacements atomiques sur les plans $\{110\}_\beta$ et $\{112\}_\beta$ forment une structure intermédiaire entre celle de la phase β parente et celles des phases α et ω, prouvant que la phase β a intrinsèquement initié une transformation.

L'étude de la précipitation au cours du procédé thermomécanique dans le domaine α+β a révélé que des précipités α discontinus, équiaxes ou légèrement allongés (1~2μm) se forment aux joints β de forte et de faible désorientation mais rarement au coeur des grains β produisant ainsi une microstructure en "collier". La relation d'orientation de Burgers (ROB) entre les phases α et β est progressivement détruite par la déformation. L'écart à la ROB est plus marqué

pour les précipités α qui se forment au joint de grains qu'à l'intérieur des grains. L'écart à la ROB augmente aussi avec la déformation, mais diminue avec la vitesse de déformation.

Au cours des déformations en bas du domaine α+β, les précipités α ont une mropholgie qui dépend de leur position. Au coeur des bandes de glissement, les grains α/β sont équiaxes et ne respectent pas la ROB. Entre les bandes de glissement, la microstructure est lamellaire où les phases α/β alternent et respectent la ROB. Dans ce dernier cas, une forte sélection de variantes a été observée: Seuls les deux ou trois variants favorisant l'accomodation de la déformation se sont formés. A titre de comparaison, dans l'état non déformé, les 12 précipités sont présents.

La transformation β→α est retardée en cours de compression à haute température. Ceci est attribué à une compétition entre adoucissement et transformation de phase. Au contraire, celle-ci est favorisée au cours de la compression à plus basse température du fait que les défauts cristallins induits par la déformation jouent le role de sites de germination et que la croissance des précipités soit accéléré alors que l'adoucissement soit ralenti.

Dans le Ti-5553, le mécanisme de déformation dominant est le glissement des dislocations. Dans les déformations en bas du domaine α+β, du glissement simple ou multiple avec deux ou trois systèmes de glissement activés. L'identification de ces systèmes a pu être effectuée par des analyses de traces.

Cette thèse a résolu la nature de la phase β metastable et constitue un travail de référence pour l'étude de la transformation β→α au cours de traitement thermomécanique.

Mots clés: Alliages de titane β métastables; Ti-5553; Traitements thermo-mécaniques; transformation de phase α→β; Sélection de variantes; Cristallographie

摘要

亚稳β钛合金由于具有高比强度、良好的塑性加工性能、优异的淬透性等综合性能而成为航空应用领域重要的结构材料。尽管近年来国内外学者对亚稳β钛合金热机械工艺及其组织演变做了大量的研究，也探究了合金析出相特征与机械性能之间的关系，但仍然存在一些具有争议和没有解决的问题。

本博士学位论文选用经过固溶淬火处理得到的初始组织为全β相的 Ti-5553 合金，采用扫描电子显微镜和透射电子显微镜(SEM/TEM)以及成分检测和晶体学计算等分析和表征方法对亚稳β钛合金β相的亚稳特性本质和高低温区域热力耦合作用下β→α动态相变行为做了深入的研究。

研究结果表明，亚稳β钛合金中β相并不全是理想的原子整齐排列的体心立方 BCC 结构，存在大量的介于β相和α与ω相之间的结构，呈现一种过渡态的预相变特点。由于原子错排，{110}β和{112}β发生畸变，从而导致 SAED 衍射图谱中出现处在 1/2, 1/3 和 2/3 位置的弱斑，β衍射斑的变形以及 TEM 照片中条纹组织的出现。

α+β 相区较高温区域热变形后显微组织结果及分析表明，β 晶粒大角晶界和小角晶界上析出不连续的等轴状或者短棒状的α相(1~2 nm)，形成“项链”组织。α相和β相之间的 Burgers 取向关系在热力耦合作用下逐渐遭到破坏。晶界α相与 Burgers 取向的偏差大于晶内α相。随着应变的增大和应变速率的降低，偏差逐渐增大。

而α+β相区较低温区域热变形过程中，析出大量具有几种不同形貌的α相，比如片层α，等轴α和不规则α。在滑移带中心区域，等轴α相和β相具有非 Burgers 取向关系。而滑移带之间的α/β片层结构由α相和β相相互间隔排列并保持 Burgers 取向关系。与单纯热处理工艺条件下 12 种α相变体在β晶内等几率出现不同，热力耦合作用条件下亚稳β钛合金局部β基体中只有两种或者三种α相变体形核。热力耦合作用下只有能够协调宏观变形的α相变体形核析出。

在高温区域热力耦合作用下，β→α相转变被显著抑制，这是由于相转变过程与热变形软化过程的竞争机制导致。相反，在低温区域热力耦合作用条件下，由于变形引入大

量晶体缺陷作为 α 相形核点和加速 α 相生长以及迟缓的热变形软化过程，β→α 相转变得到了明显的促进。

位错滑移是 Ti-5553 合金主要的变形机制。在低温压缩变形过程中，形成单滑移带或者具有两种或者三种不同滑移系的多滑移带。采用迹线分析法确定了变形试样中三种不同的滑移系。

这些结果可以为亚稳 β 钛合金中 β 相结构的本质特点提供新的理解，也可以为亚稳 β 钛合金热力耦合作用下 β→α 相转变行为提供具有价值的参考。

关键词：亚稳 β 钛合金；Ti-5553；热力耦合；β→α 相变；变体选择；晶体学

Contents

Chapter 1 Background and literature review

1.1 Introduction

In this chapter a general background of titanium and its alloys is reviewed. The chapter begins with an overview of titanium metallurgy, and the phases and phase transformation of metastable β titanium alloy. Then the hot deformation mechanism of metastable β titanium alloy is introduced. Finally, the main content of the present work are outlined.

1.2 Titanium and Titanium alloys

1.2.1 Titanium

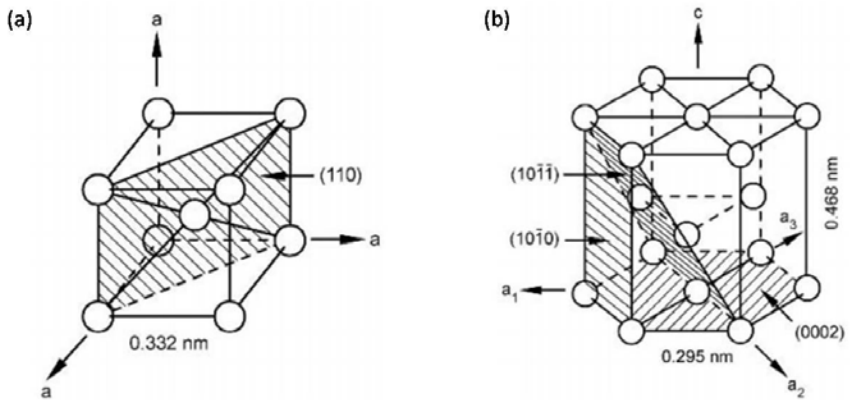

Fig. 1.1 Crystal structures of (a) , body centered cubic (BCC) unit cell of β phase with the spheres representing (0, 0, 0) and (1/2, 1/2, 1/2) atomic positions and the parameters for pure Ti a=b=c=3.32Å; α=β=γ= π/2 and (b) hexagonal closed packed (HCP) unit cell of α phase with the spheres representing (0, 0, 0) and (1/3, 2/3, 1/2) atomic positions and the lattice parameters for pure Ti a=b= 2.95Å; c= 4.68Å; α=β=π/2; γ=2π/3. [1]

Titanium (Ti) is the 22nd element in the periodic table of elements. It is a transition metal element with the atomic mass 47.867. Its electronic configuration is $1s^2 2s^2 2p^6 3s^2 3p^6 3d^2 4s^2$ [2]. Generally, it is light, strong, lustrous and corrosion resistant presenting a white silvery metallic colour. It melts at about 1678ºC and undergoes an allotropic transformation at about 882ºC (β

transus, T_β). The high temperature β phase exists above 882ºC, and possesses a body centred cubic (BCC) with a≈3.32 Å and belonging to space group Im-3m (229) (Fig. 1.1(a)). The low temperature 'α' phase possesses a hexagonal close packed (HCP) structure with a≈2.95Å and c≈4.68 Å and belonging to space group P63/mmc (194)) (Fig. 1.1(b)). The c/a ratio is 1.587, which is less than the ideal value of 1.633. [3, 4]

1.2.2 Categories of titanium alloys

Historically, a separation in the development of titanium alloys existed between the west (USA, Europe and Japan) and the east (predominantly in the former Soviet Union). This has led to the development of independent alloy systems. Several theories were used to classify the titanium alloys, such as according to β stability coefficient (K_β) and molybdenum equivalence ($[Mo]_{eq}$) and phases composition. In titanium alloys, the additional elements could be divided into α phase stabilizer, β phase stabilizer and neutral elements. Species such as Al, O, C, N raise the T_β and are termed as α stabilizers among which O, N and C readily form interstitial solid solutions with Ti. Neutral elements, such as Sn, Zr and Hf are almost all soluble in solid Ti but do not alter the β to α transition temperature. The effectiveness of these alloying elements has been expressed in terms of aluminium equivalency ($[Al]_{eq}$). It is defined as [5]: $[Al]_{eq}=Al+0.17Zr+0.33Sn+10O$. As for the other alloy elements, Mo, V, Cr, Fe, Ta, Mn, Ni, Cu and Si, they are β phase stabilizers that could lower the T_β. Similar to Al equivalency, Mo equivalency is used to compare the different effect of β phase stabilizers in various multi-component systems [6]: $[Mo]_{eq}=Mo+0.28Nb+0.22Ta+0.44W+1.6Cr+1.54Mn+0.67V+2.9Fe+1.25Ni+\ldots-Al$. In general, a $[Mo]_{eq}$ value of approximately 10.0 is required to stabilize the β phase upon quenching [7].

In general, titanium alloys are classified into four main categories: α, α+β, metastable β and β alloys, depending on the phases present at room temperature [3, 8]. The change of the type of titanium alloys as a function of β stabilizer content is shown schematically in Fig. 1.2. α alloys have only a very small fraction of β phase stable at room temperature. With the increase of the β-stabilizer content, more β phase can be stabilized at room temperature. Such alloys are

termed as α+β alloy. Martensite α' or α" phase could be present in their as-quenched state. Metastable β titanium alloys are obtained when the content of β stabilizers is increased to the range between β_c and β_s. Here, β_c is the minimum level of β stabilizer to completely retain β upon quenching from β domain, and β_s is the minimum amount of β stabilizer to obtain to have 100% of β phase at room temperature at thermodynamic equilibrium. Many phases may be found in metastable β alloys at room temperature. 100% β phase can be retained by quenching whereas at thermodynamical equilibrium α and β phases are both stable. Upon quenching, aging or deformation the ω phase may be formed. With the further increase of β stabilizers beyond β_s, β titanium alloys are obtained. For these alloys, only the β phase is stable at room temperature, therefore they can not be precipitate hardened making them less interesting for industrial applications.

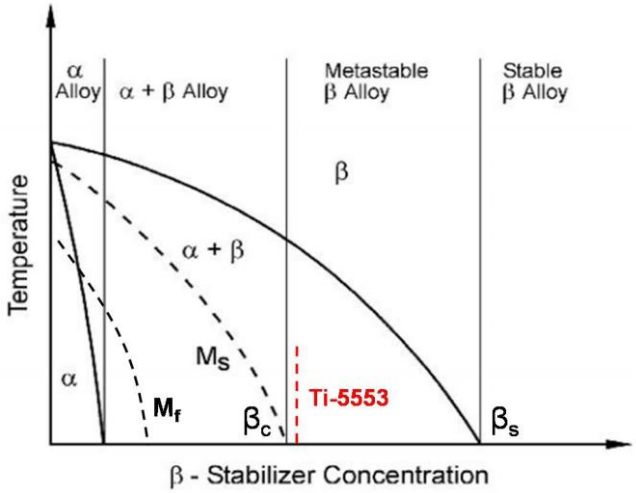

Fig. 1.2 Pseudo-binary phase diagram of titanium alloys with the decomposition products of the β phase where the location of Ti-5Al-5V-5Mo-3Cr is indicated. Here, β_c is the critical minimum β stabilizer amount for near β or metastable β alloys to completely retain β on quenching from β phase field and β_s is the minimum amount of β stabilizers for stable β alloys; T_β, RT, M_s and M_f refer to the T_β, room temperature, martensite start and finish temperatures, respectively. [1]

Metastable β alloys, such as Ti-5Al-5V-5Mo-1Cr-1Fe (VT22), Ti-7Mo-3Nb-3Cr-3Al (Ti-7333) and Ti-5Al-5Mo-5V-3Cr (Ti-5553), usually have good response to heat treatment, high weldability, superior strength-ductility combination and good workability than α+β alloy [9, 10, 11]. The microstructure and mechanical properties of metastable β alloys are sensitive

to temperature and deformation processes. It is also worth mentioning that like near α alloy there are also near β alloys that have an amount of β stabilizers between the α+β and the β alloys. Ti-5553 alloy has been defined as a near β alloy in some literature, however, the accurate affiliation should be metastable β alloy due to the fact that no martensite appears after fast cooling [12].

1.2.3 Ti-5553 alloy

Ti-5553, initially developed based on a Russian alloy system termed VT22 to substitute Ti-1023 and steel components, has excellent combination of high strength and good ductility at room temperature, and deep hardenability [13, 14, 15, 16]. Ti-5553, as marked with the red dotted line in Fig. 1.2, has applications in the field of aerospace, such as landing gear components [15, 17]. For example, the Boeing 787 utilizes Ti-5553 for landing gear applications similar to the Ti-1023 applications in Boeing 777 and Airbus A380, as shown in Fig. 1.3. For Boeing 787, an innovation is the use of the Ti-5553 alloy to fabricate the inner cylinders for the landing gear. Another significant application is the damage-tolerant "BASCA" (β annealed, slow cooled and aged) heat treatment condition which has 1100 MPa of minimum tensile strength level and have been implemented for critical fittings in the wing.

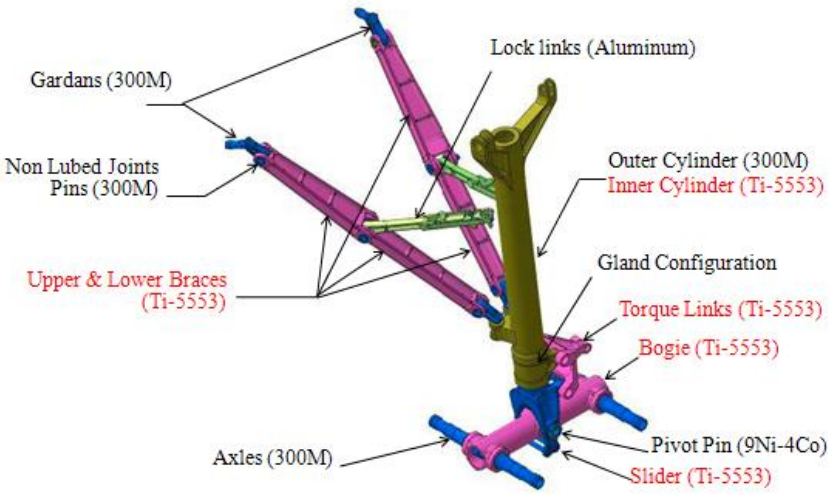

Fig. 1.3 Boeing 787 utilizes Ti-5553 for wing and nacelle application. [18]

Actually, the aforementioned three titanium alloys (Ti-5553, VT22 and Ti-1023) as well as

300M steel are still used for landing gears of aircrafts. However, Ti-1023 is somewhat difficult to melt and its mechanical properties decrease with increasing thickness. Ti-5553 offers practical improvements over Ti-1023 for large section components due to its deep hardenability and improved formability. Unlike Ti-1023 alloy that must be quenched, Ti-5553 can be air cooled from the solution treatment temperature and still provide higher strength with larger section sizes because it contains the slow diffusing element Mo. Ti-5553 with section sizes as thick as 150mm exhibits only minor decreases in strength after solution treatment followed by ageing (STA) compared with Ti-1023 for which the maximum section size is 76mm [19]. Thus, for very large landing gears, the sections exceed the maximum hardened size attainable in water quenched alloys such as Ti-1023. Moreover, prior to heat treatment, forging must be extensively performed to reduce the section size. Distortion and fracture by quenching is often a concern when heattreating such long and slender components, which complicates the manufacturing process. VT22 was extensively used in Russian for airframes in Ilyushin, Tupolev, Antonov, and Yakovlev aircraft [20]. Another similar alloy often referred to as VT22-1, having a nominal composition Ti-5Al-5V-5Mo-3Cr-1Zr (Ti-55531), is still investigated in Europe. Studies on these alloy systems, in particular Ti-5Al-5V-5Mo-3Cr, are still ongoing.

Table 1.1 Typical room temperature mechanical properties of metastable β titanium alloys. [21]

Alloy	Solution treatment and aging conditions:		Section size, mm	Typical mechanical properties				
				Ultimate strength, MPa	Yield strength, MPa	Elongation, %	Reduction of area,%	K_{1C}, MPa√m
Ti-1023	STA	Age 482-524°C, 8h, AC	32-140	1287	1202	7.7	26.7	56.5
	STA	752-774°C,2h,WQ+482-538°C,8h,AC	≥254	1256	1182	5.7	13.1	/
	STA	Age 510-566°C, 8h,AC	≤76	1141	1078	13.3	33.4	73-92
	STOA	Overage 566-621°C,8h,AC	≤76	1024	937	18.8	50.5	97-119
Ti-5553	STA	804°C,1h,AC+610°C,8h,AC	178	1294	1218	7	21	48.8
	STA	804°C,1h,AC+660°C,8h,AC	178	1163	1100	13	32	58.4
	STA	832°C,1h,AC+610°C,8h,AC	178	1332	1218	5	9	52.1
	STA	804°C,1h,AC+660°C,8h,AC	178	1189	1104	9	21	65.1

Typical room temperature tensile properties of some of the aforementioned alloys are

presented in Table 1.1 [21], compressive and shear strength are given in Table 1.2 [21]. The comparison indicates an excellent combination of high strength and good ductility in Ti-5553 alloy but has lower fracture toughness than Ti-1023. In view of static strength, Ti-5553 has a higher tensile strength/density ratio when compared with that of the other incumbent landing gear alloys. For components or sections of components designed by static strength, Ti-5553 allows a weight reduction.

Table 1.2 Room temperature compressive, shear and bearing strength of metastable β titanium alloys. [21]

Alloy	Heat treatment condition	Product form	Compressive yield strength, MPa	Shear ultimate strength, MPa	Bearing, e/D=1.5		Bearing, e/D=2	
					Ultimate strength, MPa	Yield strength, MPa	Ultimate strength, MPa	Yield strength, MPa
Ti-1023	STA 730°C,1h,AC+580°C,8h,AC	Bar	963	670	1650	1310	2002	1560
Ti-5553	STA[a] 804°C,3h,AC+610°C,8h,AC	Billet	1276	731	/	/	/	/
	STA[b]	Casting	1138	670	/	/	2248	1931

[a] Properties of 178 mm Ti-5553 billet. Corresponding tensile properties: 1294MPa ultimate strength, 1218MPa yield strength, 7% elongation, 21% reduction of area; fracture toughness 49 MPa√m; [b] Properties of cast bulkhead component heat treated to 1158MPa ultimate tensile strength, 1055MPa yield strength, 9% elongation, and 93.9 and 106.4 MPa√m fracture toughness.

Fig. 1.4 presents a comparison of the strength/density ratio and fracture toughness, for the alloys of choice used in landing gear design [22]. Depending on the size and service duty expected, aluminum alloy 7175 in the T7451 temper or ultrahigh strength steel 300M heat treated to a minimum tensile strength of 1930MPa, are the most common landing gear alloys. However, these alloys often experience corrosion degradation and must be overhauled periodically. To prevent in-service corrosion, the titanium alloy of choice is Ti-1023 in the solution treated and aged (STA) condition. Although titanium components are typically lighter and do not require maintenance due to corrosion, their acquisition cost is typically 10~15 times that of equivalent components made from ultra high strength steels. Considering the strength/density ratio in the design of a component, using titanium alloy Ti-5553, against "ultra high strength steels" 300M steel, would result in an advantage of more than 4%. Such significant advantage often justifies the additional expense. Note that the fracture toughness for

all these alloys under these treated conditions is relatively low, thus they would be considered unacceptable for design of aircraft structural members other then landing gears.

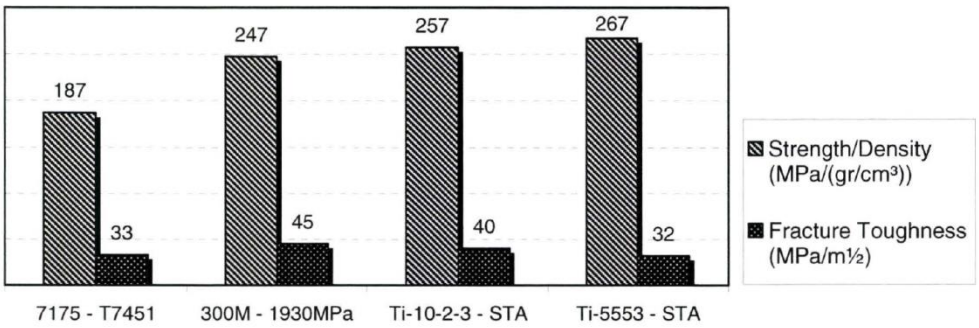

Fig. 1.4 Comparison of strength/density and fracture toughness for common landing gear alloys against Ti-5553. Note: STA refers to solution treated and aged corresponding to the "peak strength" condition. [22]

Compared with the most commonly used α+β alloy Ti-6Al-4V (Ti-64), the metastable β alloy Ti-5553 can exhibit higher strength, as summarized in Fig. 1.5(a). In addition, Ti-5553 alloy also exhibits outstanding high-cycle fatigue property compared with Ti-64 alloy, as shown in Fig. 1.5(b).

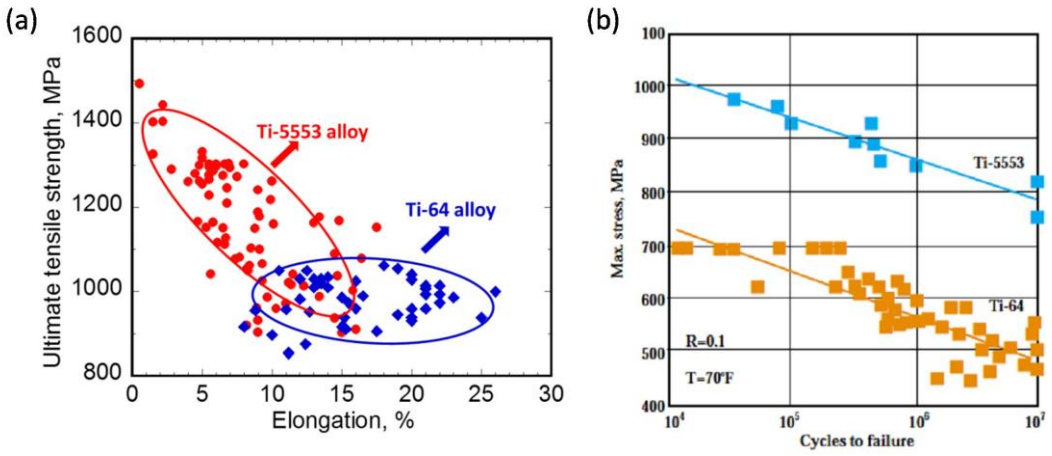

Fig. 1.5 (a) Ultimate tensile strength and elongation of Ti-5553 alloy compared with Ti-64 alloy [23]. (b) High-cycle fatigue property of Ti-5553 alloy compared with Ti-64 alloy [15].

The strength, ductility and fracture toughness of Ti-5553 could be modified in a wide range by varying its microstructure. Especially the size and distribution of α precipitates formed within β parent phase matrix is critical factor to manipulate mechanical properties of Ti-5553.

Therefore, understanding microstructural evolution, especially α precipitation process, in Ti-5553 under specific heat treatment is critical to control its mechanical properties.

1.3 Phase transformations in metastable β titanium alloys

In the metastable β alloys, there are several phases and phase transformation involved. These phases can be classified into β, α, α", ω and β'. Indeed, the supersatured β matrix is usually unstable and could easily transform to other more stable phases, i.e. β→α+β (diffusional/displacive transformation), β→ω+β (shuffle transformation), β→β+β' (phase separation), and β→α"+β (martensitic transformation). ω, α" and β' are called intermediate phases which could assist the nucleation of final stable α phase [1].

1.3.1 β to α transformation

The α phase is described in ***Section 1.2.1***. As we know that in titanium alloys, the excellent combination of mechanical properties could be obtained by the homogeneous nucleation and subsequent growth of finely dispersed α phase in the β matrix [24]. Thus, the characteristics and mechanisms of nucleation and growth of α phase have been extensively investigated. The α precipitates are usually classified according to their morphology and size. For example, the α precipitates that form while cooling from the β phase are usually coarse in nature. Metallurgists named it as primary α (α_p). Another finer α precipitates would nucleate between α_p during the subsequent aging process at lower temperatures, and metallurgists refer to the latter as secondary α (α_s).

The α phase can be precipitated when the alloys are cooled at low cooling rates from temperatures above T_β or upon aging at the α precipitation temperature range. A layer α phase firstly nucleates and grows along previous β grain boundaries (α_{GB}). Upon further cooling, parallel Widmanstätten α plates (α_{WGB}) nucleate from that α_{GB} and grow into the interior of β grain [25, 26]. A Widmanstätten α colony correspond to a single crystallographic variant (Fig. 1.6(a)) [27]. α precipitates with multiple crystallographic variants obtained by fast cooling are called basketwave α (Fig. 1.6(b)) [28]. When a titanium alloy is solution treated in the α+β

region, the equiaxed α_p would be retained forming the equiaxed microstructure (Fig. 1.6(c) [27]. During aging at a lower temperature, nanoscale acicular or lenticular secondary α (α_s) will nucleate between the α_p particles and fill the retained β phase (Fig. 1.6(d)) [24].

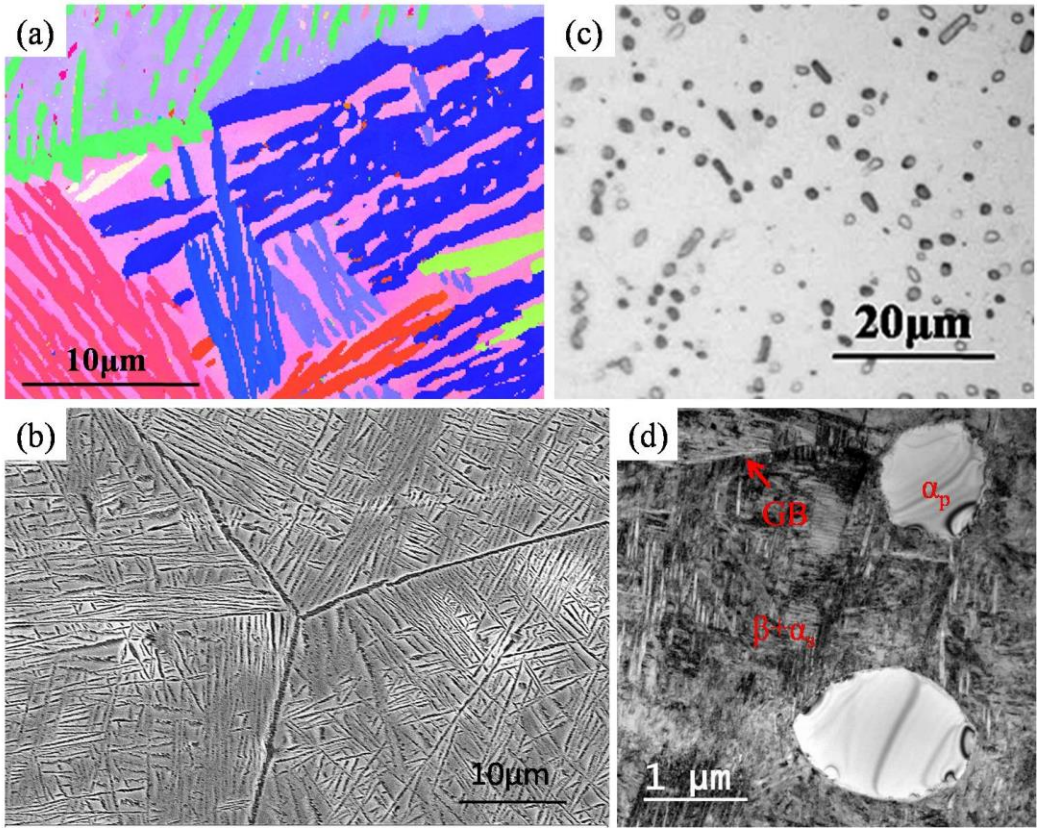

Fig. 1.6 Morphologies of α phase in metastable β titanium alloy Ti-7333: (a) solution treated at 900°C for 30min and cooled in furnace [27] (b) 880℃ aged for 2 h and cooled in furnace under 2℃ /min to 600°C and aged for 6 h then cooled in air [28] (c) solution treated at 800°C for 30min and water quenched [27] (d) 820°C aged for 50min and cooled in air to and aged for 520°C for 6h and cooled in air [24].

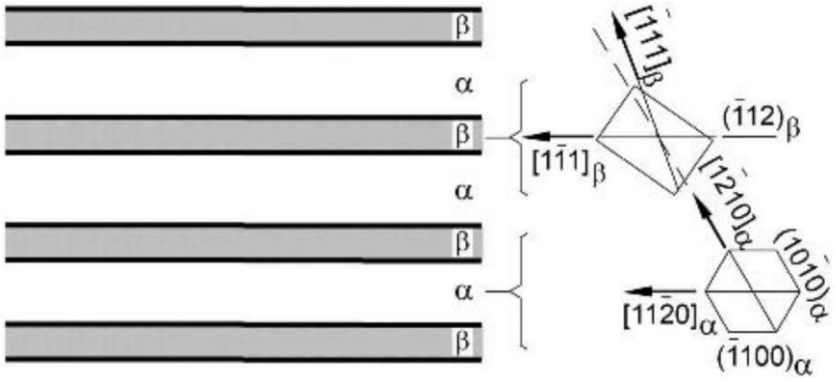

Fig. 1.7 Schematic diagram of the Burgers orientation relationship between α and β phases [3, 29].

As shown in Fig. 1.7, in general, α phase strictly maintains the Burgers orientation relationship (BOR) with the β phase, represented by: $\{0001\}_\alpha \parallel \{110\}_\beta$, $\langle 11\bar{2}0\rangle_\alpha \parallel \langle 111\rangle_\beta$ [30]. Due to crystal symmetry, differently orientated α might and are known as variants. The six distinct $\{110\}_\beta$ planes and the two distinct $\langle 111\rangle_\beta$ directions on each $\{110\}_\beta$ of BCC β can generate a maximum of 12 crystallographic variants of α, as summarized in Table 1.3 [31].And the axis/angle pairs for all 6 possible α/α boundaries in a single β grain are shown in Table 1.4 [32]. Except the BOR, several other ORs between BCC/HCP structures have been observed in titanium alloys, namely, Pitsch-Schrader OR [33] ($(110)_\beta \parallel (0001)_\alpha$, $[001]_\beta \parallel \langle\bar{2}110\rangle_\alpha$) and Potter OR [34] ($(110)_\beta \parallel (0\bar{1}11)_\alpha$, $[1\bar{1}1]_\beta \parallel [\bar{2}110]_\alpha$)

Table 1.3 Orientation variants resulting from β→α phase transformation under BOR. [31]

Variant No.	Corresponding plane $(hkl)_\beta \| (hkil)_\alpha$	Corresponding direction $[uvw]_\beta \| [uvtw]_\alpha$
1	$(011)_\beta \| (0001)_\alpha$	$[\bar{1}\bar{1}1]_\beta \| [2\bar{1}\bar{1}0]_\alpha$
2		$[1\bar{1}1]_\beta \| [2\bar{1}\bar{1}0]_\alpha$
3	$(\bar{1}01)_\beta \| (0001)_\alpha$	$[1\bar{1}1]_\beta \| [2\bar{1}\bar{1}0]_\alpha$
4		$[111]_\beta \| [2\bar{1}\bar{1}0]_\alpha$
5	$(0\bar{1}1)_\beta \| (0001)_\alpha$	$[111]_\beta \| [2\bar{1}\bar{1}0]_\alpha$
6		$[\bar{1}11]_\beta \| [2\bar{1}\bar{1}0]_\alpha$
7	$(101)_\beta \| (0001)_\alpha$	$[\bar{1}11]_\beta \| [2\bar{1}\bar{1}0]_\alpha$
8		$[\bar{1}\bar{1}1]_\beta \| [2\bar{1}\bar{1}0]_\alpha$
9	$(\bar{1}10)_\beta \| (0001)_\alpha$	$[\bar{1}\bar{1}1]_\beta \| [2\bar{1}\bar{1}0]_\alpha$
10		$[111]_\beta \| [2\bar{1}\bar{1}0]_\alpha$
11	$(110)_\beta \| (0001)_\alpha$	$[1\bar{1}1]_\beta \| [2\bar{1}\bar{1}0]_\alpha$
12		$[\bar{1}11]_\beta \| [2\bar{1}\bar{1}0]_\alpha$

Generally, intragranular α (α_I) precipitates develop into plate shape during growth due to their orientation relationship with the β matrix, the coherency state and the associated anisotropy in interfacial energy [35], elastic strain energy [36] and growth kinetics. The tips of

α plates are thought to have an incoherent α/β interface and the broad faces are thought to be either coherent or semi-coherent [37, 38]. Lengthening and thickening of precipitates have been investigated by Aaronson et al. [39, 40, 41] and is believed to follow a ledge mechanism, where lengthening occurs by the addition of atoms at the incoherent risers of ledges at the tips of the plates and thickening results from the movement of growth ledges across the broad semi-coherent interfaces [42]. The habit plane of the α phase is $[\overline{11}\ 11\ 13]_\beta$ and the growth direction is $[3\bar{3}5]_\beta$, respectively [43, 44].

Table 1.4 Axis/angle pairs for all 6 possible α/α boundaries in a single β grain. [32]

Type	Axis/angle pairs	P_{random} (%)
1	I (Identity)	/
2	$[11\bar{2}0]$/60°	18.2
3	$[\overline{10}\ \bar{7}\ 17\ 3]$/60.83°	36.4
4	$[\overline{10}\ 5\ 5\ 3]$/63.26°	18.2
5	$[7\ \overline{17}\ 10\ 0]$/90°	18.2
6	[0001]/10.53°	9.1

In an ideal case, all variants occur with equal probability during β→α phase transformation. Theoretically, one can detect up to 12 α variants in one β grain, [45]. However, much stronger α textures than expected appeared frequently in practice, and have been related to variant selection mechanisms [46, 47, 48, 49]. For α_{GB}, three variant selection rules might be obeyed by α_{GB} (as shown in Fig. 1.8) [47]: Ⅰ, the variant selection of the α_{GB} is made to maintain as close as possible the BOR with both adjacent β grains. Such a α_{GB} variant should have low energy α/β interfaces with respect to both β grains and thus a low nucleation barrier. Ⅱ, the major low energy facet $\{112\}_\beta \parallel \{\bar{1}100\}_\alpha$ of the selected α variant should have the minimum deviation from the grain boundary plane (GBP). Ⅲ, the matching of the close-packing directions (i.e. $\langle 2\bar{1}\bar{1}0\rangle_\alpha \parallel \langle 111\rangle_\beta$) of the selected variant makes the smallest deviation angle from the GBP, i.e. $\langle 2\bar{1}\bar{1}0\rangle_\alpha \parallel \langle 111\rangle_\beta$ tends to be parallel to or be included in

the GBP.

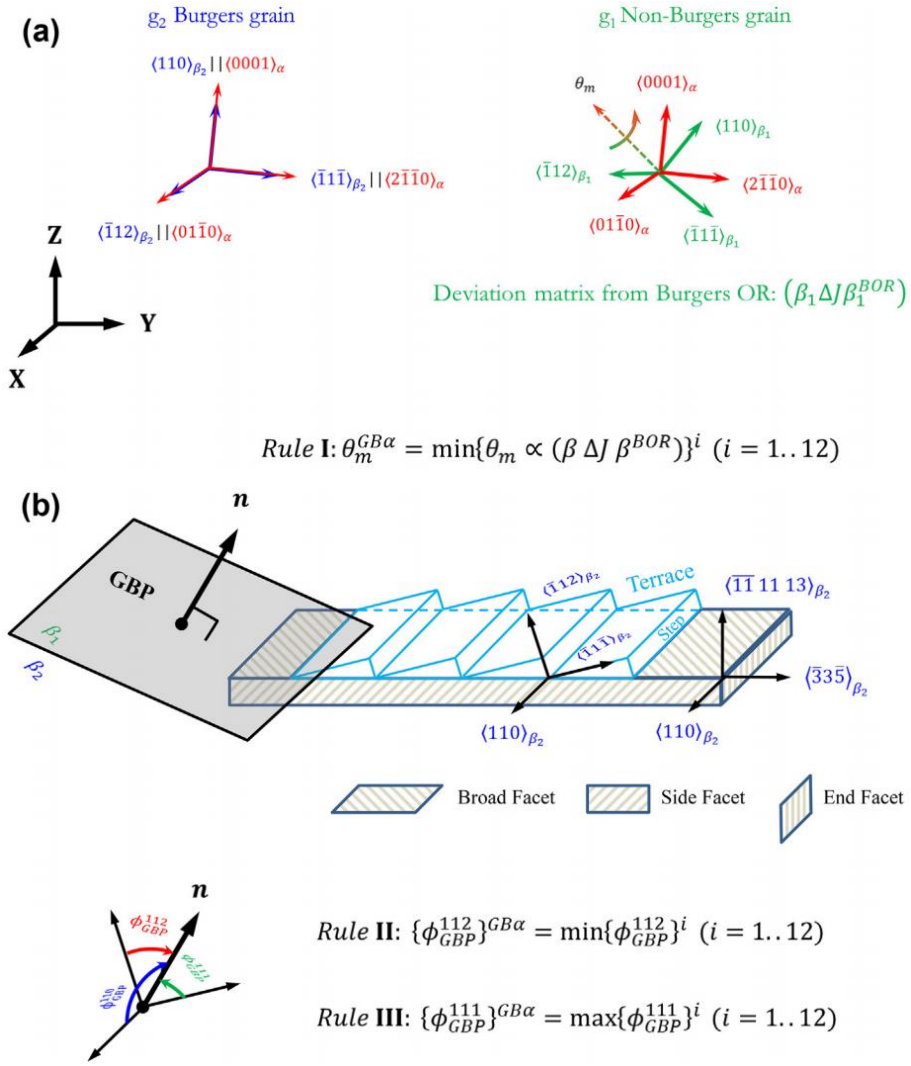

Fig. 1.8 Schematic illustration of different empirical rules concerning the influence of grain boundary parameters, misorientation and grain boundary plane (GBP) inclination, on variant selection of grain boundary α,α_{GB}. $\boldsymbol{\theta}_m$ is the disorientation angle associated with the deviation matrix ($\beta\Delta J\beta^{BOR}$) that is a quantitative measure of the deviation of the orientation relationship (OR) between the α_{GB} and the non-Burgers grain from the BOR. φ_{GBP}^{112} are the inclination angles between the GBP and one of the $\{112\}_\beta$ planes and φ_{GBP}^{111} are the inclination angles between the GBP and one of the $\langle 111\rangle_\beta$ directions. X, Y, Z represents the sample reference frame where orientations of matrix β grains and grain boundary plane inclinations are expressed. [47]

Actually, the microstructural composition of titanium alloys is also dominated significantly by the deformation processes. R. Shi et al. [50] develop a three-dimensional quantitative phase field model to predict variant selection and microstructural evolution in

Ti-6Al-4V under the influence of both external and internal stresses. It is found that, for a given undercooling, the development of a transformation texture (also called microtexture) of the α phase due to variant selection during precipitation is determined by the interplay between externally applied stress or strain and internal stress generated by the precipitation reaction itself. Thus, the variant selection mechanism during thermomechanical processing might be much more complicated and severely restricted by the nature of the defects such as subgrain boundaries, stacking faults, dislocations and slip bands [44]. For instance, dislocations belonging to the $\{112\}\langle 111\rangle$ slip systems would favour the nucleation and the growth of a single α variant whose orientation relationship is described by the components of the specific slip system [44, 51]. The variant selection in subgrain boundary nucleation can be influenced by the nature of subgrain boundary plane. The low-energy, parallel close packed planes are nearly parallel to the subgrain boundary plane. This variant selection is the same as the already described one for the nucleation on high-angle grain boundaries [51]. There also exists an obvious tension/compression asymmetry in variant selection behavior, i.e. the types and numbers of variants produced under tensile and compressive stresses are different. For example, pre-straining obtained via uniaxial tensile and compressive stress along $[010]_\beta$ will result in a selection of 8 and 4 out of the 12 variants, respectively. It suggests that the variant selection is sensitive to the initial stress state and has a tension-compression asymmetry [50].

Moreover, the introduction of lattice defects into the matrix by thermomechanical processing increases such nucleation sites and consequently raises the nucleation rate of the product phase. The morphology of the precipitated α phase could be also changed during hot deformation [52], even the orientation relationship between α and β phases could be destroyed [53]. Because of these complications, limited work exists in the literature on β→α variant selection during thermomechanical processing. Thus, it is important to clarify the rules of microstructural evolution under the thermomechanical process.

1.3.2 β to ω transformation

The occurrence of the ω phase (HCP, hexagonal close-packed with a≈4.646Å and

c≈2.82Å; space group P6/mmm (191)) was first reported in 1954 by Frost et al. [54] in Ti-V alloys, and then metastable ω phase was found in the other group IV transition metals (such as Zirconium and Hafnium). The finding of transitional ω phase enriches the research on α phase nucleation, as the formation of α has been found to be assisted by ω phase (the so-called ω-assisted nucleation mechanism), though it might cause embrittlement in some titanium alloys [55, 56, 57]. The expectation is that dispersive distribution of fine α phase could be obtained via the ω-assisted nucleation. Two types of ω phases, athermal and isothermal, usually appear as small cuboidal or ellipsoidal particles with nanoscale size in titanium alloys. Moreover, deformation-induced ω phase could form in the β-stabilized alloys upon shock loading. Some studies [58, 59, 60] have reported the presence of the deformation-induced ω phase in metastable titanium alloys upon deformation at room temperature. Banerjee et al. [61] proposed that the deformation-induced ω phase is almost the same as the athermal ω phase. They thought that the formation condition of deformation-induced ω phase in the shock loading experiment is equivalent to athermal treatment, because the duration of the shock loading is typically in the order of a few μs, thus diffusive atom movement is negligible.

In general, the athermal ω phase forms during quenching from the high temperature β phase field to the room temperature, whereas the isothermal ω phase precipitates after aging treatment at temperatures below approximately 550℃ [57, 62, 63]. The athermal ω phase is formed by a diffusionless transformation, while the isothermal transformation is accompanied by chemical composition changes during which the solutes concentrate in β phase [64]. The athermal ω phase formation has been commonly viewed as a result of β decomposition via a shuffle transformation and alternate collapses of $\{111\}_\beta$ crystal planes during cooling. Typically, the shuffle transformation during cooling causes an incomplete transformation to ω, but the transformation may be completed during aging treatments, from trigonal symmetry (space group P3m1 (156)) to hexagonal symmetry (space group P6/mmm (191)) [65, 66]. Both structures contain 3-atoms/unit cell and can be derived from the parent bcc structure by simple atom movement. The equivalent positions are: 0, 0, 0; 2/3, 1/3, 1/2; 1/3, 2/3, 1/2 for ideal hexagonal, and 0, 0, 0; 2/3, 1/3, 1/2+z; 1/3, 2/3, 1/2−z ($0<z<0.167$) for incomplete

transformation structure. When z=0, ω structure is an ideal structure with hexagonal symmetry, and when z=1/6, the structure has cubic symmetry. The morphology of ω particles depends on the composition of titanium alloys and ω/β misfit. Moreover, the well-documented orientation relationship between ω and β phases is: $(111)_\beta \parallel (0001)_\omega$ and $[1\bar{1}0]_\beta \parallel [11\bar{2}0]_\omega$ [67].

1.3.3 β to α'' transformation

The martensite α'' is an orthorhombic phase (Cmcm space group) with lattice parameter between that of β phase and that of α phase, which usually exhibit acicular morphology [68, 69, 70]. It often forms during deformation (strain-induced phase transformation) and more rarely during athermal β→α'' transformation. Thus, the strain-induced α'' phase was often investigated in metastable β titanium alloys. Martensitic transformation is a diffusionless transformation where no composition changes occur between parent β phase and α'' phase. α'' forms in alloys with higher solute content. However, with increasing β phase stabilizer amount, Ms (α'') temperature decreases rapidly and therefore α'' phase is more difficult to form. α'' phase and β matrix possess the orientation relationship of $(100)_{\alpha''}//(110)_\beta$ and $[111]_{\alpha''}//[111]_\beta$ [71]. Duerig et al. [72] evaluated the lattice constants of α'' and found: a = 3.01 Å, b = 4.83 Å, c = 4.62 Å. He also proposed a schematic that relates the BCC structure of β phase to the orthorhombic structure of α'' phase.

1.3.4 β to β' transformation

The β' phase, the solute lean BCC structure phase, could form in the solute rich β titanium alloys by the generic spinodal mechanism. It exhibits the same BCC structure as β phase, but has different composition [73]. β and β' are coherent, and distributed homogeneously in the matrix. The morphology of β' phase could be determined by the differences of chemical composition and the misfit between β and β' phases. In some papers, β' is used to indicate solute rich BCC structure phase. β_1 and β_2 are also used to represent solute lean and solute rich BCC phases [1, 74, 75]. This phase separation occurs by traditional nucleation and growth or spinodal decomposition [1] at temperatures between 200 and 500°C in a form of very fine scaled precipitates that can only be resolved by transmission electron microscopy (TEM). As S.

Nag et al. showed, the decomposition of β into β+β' for Timetal 555 appears to be by spinodal decomposition when aging is below 600°C [76]. Spinodal decomposition could occur faster by homogeneously diffusing a distance of 5 to 10nm as long as the composition and temperature conditions are satisfied [77].

1.3.5 Metastable phase decomposition

The aforementioned metastable phases, such as ω, α'' and β', are the non-equilibrium phases that can be formed due to insufficient time given for long range diffusion of atoms needed to rearrange themselves from one stable phase to another. However, uniformly distributed fine scaled α phase formed in titanium alloys by low temperature ageing are usually associated with an assisted nucleation event. The nucleation sites for the α phase also include the β/ω, β/α'' and β/β' interfaces [74]. Furuhara et al. [78] have reported the inter orientation relationship between β, ω and α phases as $(0\bar{1}1)_\beta \parallel (0001)_\alpha \parallel (\bar{1}\bar{1}20)_\omega$ and $[111]_\beta \parallel [11\bar{2}0]_\alpha \parallel [0001]_\omega$, indicating that α forms at the interface of the ω and β phases. Actually, fine homogeneous α could formed via nucleation within ω [55], at the ω/β interface [56] or near this interface [57]. A consensus that could be reached is that α phase grows by consuming the ω phase. Similarly, α'' and β' could be decomposed during the subsequent ageing treatment [76].

To sum up, despite the efforts in deconvoluting the complicated phase transformation stages of the metastable β Ti alloys and in identifying the product phases, the supersaturated metastable structure of β phase has not been well understood until now. There are still some characteristics of β frequently observed in TEM diffraction patterns and in TEM bright and dark field images remaining un-interpreted. For example, weak diffraction spots appearing at the exact 1/2 β diffraction positions in addition to those of α can be found in papers dealing with metastable Ti alloys [12, 57]. The structure producing such diffraction spots has not been explained. Striations with blurred edges appearing in β phase have also been frequently observed in TEM bright and dark field images [79, 80, 81]. These striations have been interpreted either as stacking faults [79] or as spinodal decomposition zones [81]. However, such interpretations have not been experimentally sustained.

1.4 Hot deformation behaviour of metastable β titanium alloys

β titanium alloys are usually subjected to various thermomechanical processes before the final desired products are obtained [82]. Hot working of titanium alloys is generally considered in relation to the T_β, due to the significantly different deformation characteristics of the HCP α and BCC β phases. The β phase features rapid diffusion rates (a hundred or more times faster than α in alloy) and a relatively low temperature dependence of flow stress [83]. Below the T_β, the presence of the α phase in the more ductile β microstructure influences flow behaviour as the α crystal structure possesses fewer slip systems and can produce difficult slip transfer [84].

1.4.1 Stress-strain behaviour and constitutive equation

Actually, the hot deformation process is a competition between dynamic hardening and dynamic softening. The flow stress usually increases with the increased of strain and decreased of strain rate. Flow stress reflects the deformation resistance of materials during plastic deformation. Higher deformation resistance corresponds to larger external force needed during plastic deformation. Thus, it is an easy and effective way to evaluate the workability of the titanium alloys by comparing their flow stresses [85]. Moreover, It is well accepted that the relationship between the flow stress (σ), strain rate ($\dot{\varepsilon}$) and temperature (T) during hot deformation is generally expressed in the form of Arrhenius type equation given by Sellars and McTegart [86], i.e. $\dot{\varepsilon} = A[\sinh(\alpha\sigma)]^n \exp[-Q/(RT)]$. A and α are constants, Q is the activation energy, R is the gas constant, n is the stress exponent (n=1/m, m is the strain rate sensitivity).

1.4.2 Dynamic recovery and dynamic recrystallization

Due to the increased atomic mobility at high temperature, softening processes, such as dynamic recovery (DRV) and dynamic recrystallization (DRX) would occur during high temperature deformation. During DRV, the dislocations move through glide, climb or cross-slip [87], which could help to relieve some of the residual stresses present during deformation. Through further rearrangement they will commonly form low-angle grain or subgrain boundaries. The DRX can be classified as: (i) discontinuous dynamic recrystallization (DDRX),

during which the nucleation and growth of new grains operate through a bulging mechanism with relatively low stacking fault energy [88]; (ii) continuous dynamic recrystallization (CDRX), which involves a transformation of low angle boundaries into high angle boundaries of the subgrains with relatively high stacking fault energy [89].

In metastable β titanium alloys, the DRV/DRX occur mainly in β phase because the deformation is mainly coordinated by β phase has more slip systems. Abundant studies indicated that the DRX in metastable β titanium alloys is CDRX [90, 91]. However, in β and metastable β titanium alloys, it is generally accepted that the predominating softening mechanism of the β phase is DRV [11]. The main softening tendency of β phase from DRV to DRX with the increase of deformation temperature [85, 91]. Both increasing the temperature and decreasing the strain rate seem to promote the DRX process [92].

1.4.3 Fragmentation and globularization of α lamellar

The lath or long rod shaped α at the grain boundaries could be gradually fragmented and spheroidized to globular particles, which was associated primarily with the classical boundary splitting (dynamic) followed by a further spheroidization of α particles by means of termination migration (static) [63, 93, 94, 95]. The kinetics of α plate fragmentation during deformation also depends upon the nature of the α/β interphase boundaries [96]. Loss of coherency of the α/β interphase boundaries with increasing stress intensifies dynamic fragmentation of the lamellar microstructure due to (1) the hindering of dislocation movement across non-coherent α/β interfaces and (2) a concomitant increase in the interphase boundary energy.

Moreover, the deformation and consequently the globularization of α lamellar structure have been reported to be quite heterogeneous [97]. The extent of the lamellae globularization has been related to the orientation of their ***c***-axes with respect to the applied strain. For example, Bieler observed that globularization is difficult in colonies having their ***c***-axes parallel to the compression direction as the prismatic and basal slip systems cannot be activated. By contrast, a high rate of globularization was observed in regions where basal and prismatic slips were possible, i.e. in colonies with ***c***-axes at 15–75° from the compression axis. Thus, the

heterogeneous deformation/globularization could explain the differences observed in the α_p texture intensity and morphology from one macrozone to the other [98].

1.4.4 Slip, twin and induced martensite

It has been reported that the deformation mechanisms in the β titanium alloy include [99] (1) dislocation slip, (2) $\{332\}\langle 113\rangle$ twinning and (3) stress-induced martensitic transformation. Banerjee et al. [100] summarized the variety of inelastic responses of the β phase to stress, shown in Fig. 1.9. It can be seen that dislocation slip transforms to $\{112\}\langle 11\bar{1}\rangle$ type twinning and $\{332\}\langle 11\bar{3}\rangle$ type twinning with the decrease of the stability of the β phase [101, 102, 103]. At the same time, the stress-induced phase transformation also often occurs in these alloys.

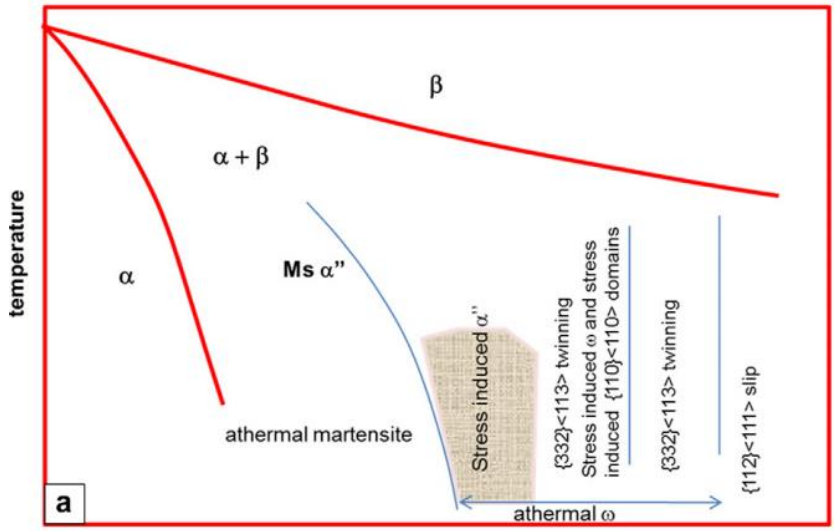

Fig. 1.9 A schematic diagram of the effect of β alloys content on β phase deformation mechanism. [100]

The actual deformation behaviour of single phase metastable β titanium alloys strongly depends on the degree of stability of the β phase [104]. However, this stability is associated with the content of the β-stabilizing element. As the β phase stability increases, the deformation mode changes from twinning/stress-induced martensitic transformation to slip, as shown in Fig. 1.10. In titanium alloys, the molybdenum equivalency ($[Mo]_{eq}$) is selected as a common criterion to assess the stability of the β phase in titanium alloys [105]. It is defined as the amount of β-stabilizing elements relative to the amount of molybdenum required for the same degree of

β phase stability. It has been empirically observed that the β phase is not stable enough to suppress α" martensitic transformation if the $[Mo]_{eq}$ is less than 10wt. % [106]. In fact, extensive investigations [60, 107, 108, 109, 110] have been carried out on the stress-induced martensitic transformation during elastic process in the metastable β titanium alloys. Similar to a number of BCC metals (Fe, Mo, W, V, etc.), the metastable β titanium alloy has BCC structure at as-quenched state, and dislocation slip is the important deformation mode. The slip systems in BCC structure have well been evidenced. For the BCC structure, even though the most densely packed planes are the {110} planes, slip can also operate on the {112} and {123} planes, all with the same ⟨111⟩ Burgers vector, giving rise to 48 slip systems [111]. Furthermore, cross- and multiple- slip are often observed in this structure. S. Hanada et al. [112] reported that dislocation slip is the leading deformation mechanism for the β alloys, which can be attributed to the fact that the addition of enough β-stabilizing elements inhibits the occurrence of stress-induced martensitic transformation and twinning [104].

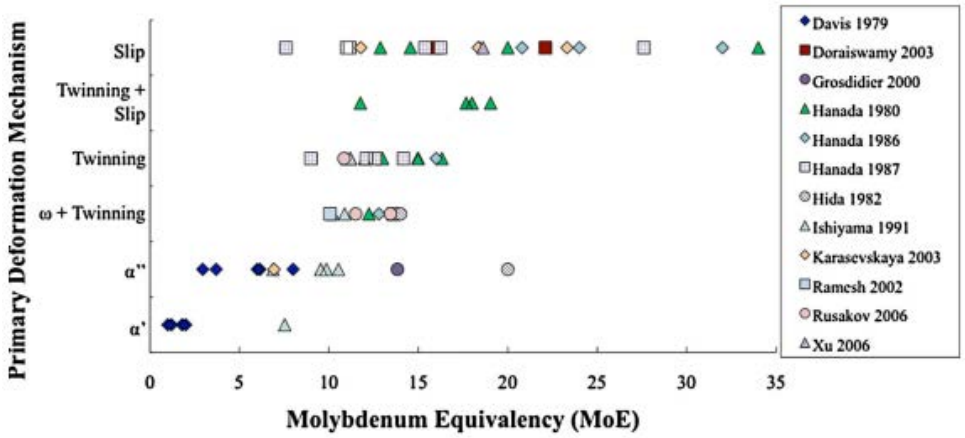

Fig. 1.10 The experimental results that were reported for stress-induced deformation mechanisms as a function of $[Mo]_{eq}$ value for a broad range of alloy compositions, microstructures, and test methods. [113]

As discussed above, extensive studies of the deformation behavior of titanium alloys have been paid great attention in the past decade. However, the dynamic β→α phase transformation during the thermomechanical process was often overlooked. Actually, the phase transformation and deformation process interact each other significantly due to the different coordination behaviour between the α/β phases. Abundant defects, such as dislocations and slip bands, would be induced during deformation, which would give an obvious effect on the nucleation

behaviour and variant selection mechanism of α phase. The dynamic nucleation behaviour of α phase during the hot deformation should be investigated in detail.

1.5 Content of the present work

As aforementioned, despite the efforts in resolving the complex microstructural evolution related to thermomechanical process of the metastable β titanium alloys and in gaining knowledge on the produced phases as well as their correlations with the resultant mechanical properties, there are still some controversial and unresolved issues. Firstly, the nature of supersaturated β matrix is still not entirely revealed, although extensive studies of the decomposition of metastable β phase have attracted great attention in the past decades. Secondly, the dynamic nucleation behavior of α phase in metastable β alloys have not been fully assessed and exploited during the coupled thermomechanical process, including morphology, nucleation site, transformation amount and variant selection mechanism of α phase. The microstructural evolution might be much more complicated and dependent on the treatment due to the interplay between the stress field and the thermal field. Lastly, as a representative metastable titanium alloy, the transformation characteristics of Ti-5553 alloy deformed in different temperature regions are still not fully revealed. Based on such an observation, the present PhD work is dedicated to work out the metastable nature of β phase at room temperature and the β→α phase transformation characteristics during high and low temperature deformation, using Ti-5553 alloy. The main content of the work is outlined as follows:

(1) Preparation of Ti-5553 alloy through specific thermal and coupled thermomechanical treatment to obtain the required specimens of the present thesis work.
(2) Revelation of the origins of some microstructural features of β phase revealed by TEM observations, including additional weak reflections in SAED patterns and striations in TEM bright/dark field images, and their intrinsic links with the metastable nature of β phase.

(3) Morphological and crystallographic characterizations to evidence the features of α precipitates nucleated dynamically during coupled thermomechanical process at two specific temperatures (high and low).

(4) Depicting the β to α transformation mechanisms under the two coupled thermal and mechanical conditions and working out variant selection roles of α formation during low temperature deformation.

This work is expected to provide new insights into the nature of the β phase and useful information on β to α transformation during coupled thermomechanical processes.

Chapter 2 Materials, experimental procedures and crystallographic calculations

2.1 Introduction

In this chapter, the experimental procedures for the alloy preparation, specimen preparation and treatments methods as well as the microstructural characterizations of the Ti-5553 alloy are firstly introduced. Then the crystallographic calculation methods for the corresponding results analyses were presented. The whole experimental procedures are outlined in Fig. 2.1.

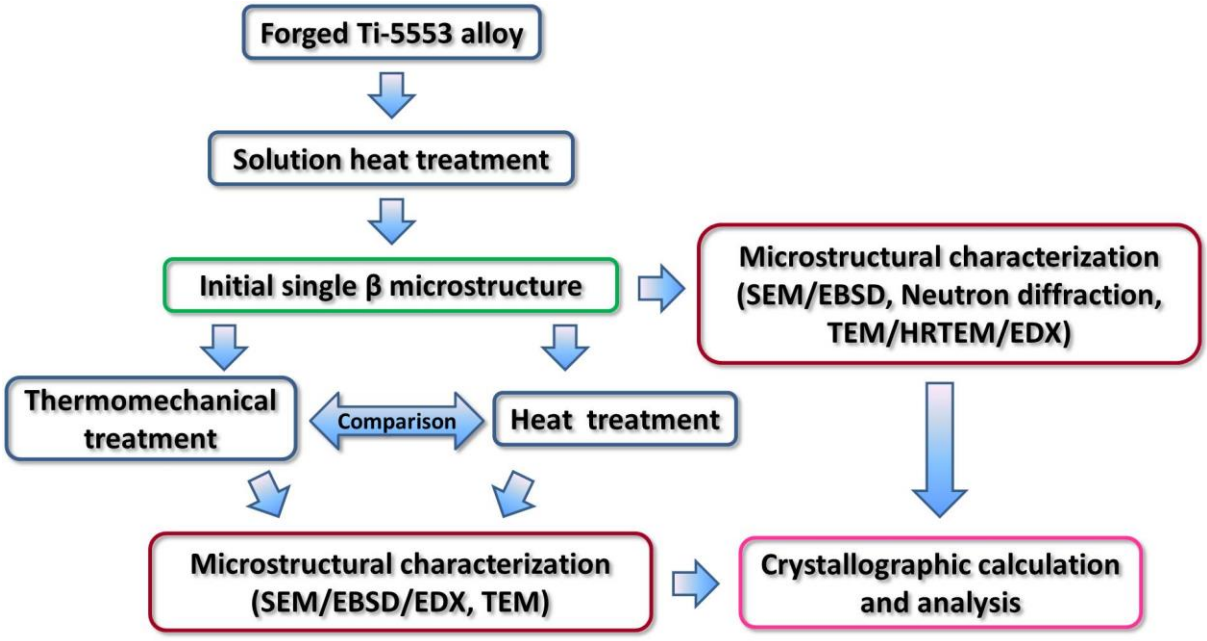

Fig. 2.1 Flow chart of the experimental procedures of the present work.

2.2 As received material

The as-received material is forged Ti-5553 in a bar shape with a diameter of 280mm. It was forged in a temperature range with the starting temperature in the β region and the finishing temperature in the α+β region. The chemical composition of the alloy determined by coupled plasma atomic emission spectrometry (ICP-AES) is given in Table 2.1. The β transus

temperature (T_β) determined by metallographic analyses is approximately 870°C.

Table 2.1 Chemical composition of the Ti-5553 used in the present work (wt. %).

Ti	Al	Mo	V	Cr	Fe
Bal.	5.27	4.99	4.80	2.76	0.42

2.3 Sampling

As Fig. 2.2 shows, all the heat treatment and hot compression samples were in cylindrical shape and cut out of the ½ radius region with their axis parallel to that of the forged bar by wire electrical discharge machining. The samples were further mechanically grounded to remove the cutting traces with SiC papers up to 400 grit.

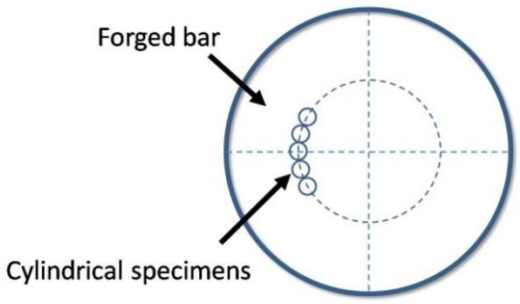

Fig. 2.2 Schematic diagram of sampling positions in the forged bar.

2.4 Thermal and thermo-mechanical treatments

Two groups of treatments were applied to produce microstructures for the study of the structure modulation of β phase of the Ti-5553 alloy and for the study of impact of deformation on β to α phase transformation. For the first study, the specimens were solution treated with various procedures and some specimens were further aged in the α+β temperature zone. For the second study, two kinds of treatments were applied after the specimens were solution treated to obtain single β as initial microstructure. One is thermal mechanical treatments realized by hot compressions in the α+β zone; the other is mere thermal treatments processed with the same thermal procedures of the thermal mechanical treatments. The latter is to produce reference state for the deformed state of the alloys to differentiate the effect of deformation on the β to α

phase transformation of the alloy.

For the only heat treated specimens, the heat treatments were performed using the OTF-1200X tube furnace. The samples were loaded into the furnace when the set temperature of the furnace was reached. Because all of the examinations do not involved the edge of specimen, vacuum atmosphere was not chose.

2.4.1 Heat treatment for the study of structure modulation of β phase

The specimens were solution treated at 1000°C and 900°C, respectively, for 30min and then cooled with three cooling rates, i.e., water quenching (WQ), air cooling (AC) and liquid nitrogen quenching (LNQ). The detailed cooling manners are given in Table 2.2. Three of the 900°C solutionized and water quenched specimens were further aged at 800°C, 600°C and 350°C, respectively and quenched in water. The detailed heat treatment parameters are displayed in Table 2.3.

Table 2.2 Detailed solution treatment parameters. WQ: water quenching; AC: air cooling and LNQ: liquid nitrogen quenching.

Temperature (°C)	Time (min)	Cooling
900	30	WQ/AC/LNQ
1000		WQ

Table 2.3 Aging treatment parameters after solution treatment at 900°C.

Temperature (°C)	Time (min)	Cooling
600/800	30	WQ
350	120	

2.4.2 Treatments for study of influence of hot deformation on phase transformation

2.4.2.1 Solution treatment

To obtain the initial single β microstructure, the cylindrical specimens were solution treated at 900°C for 30min followed by water quenching, as shown in Fig. 2.3.

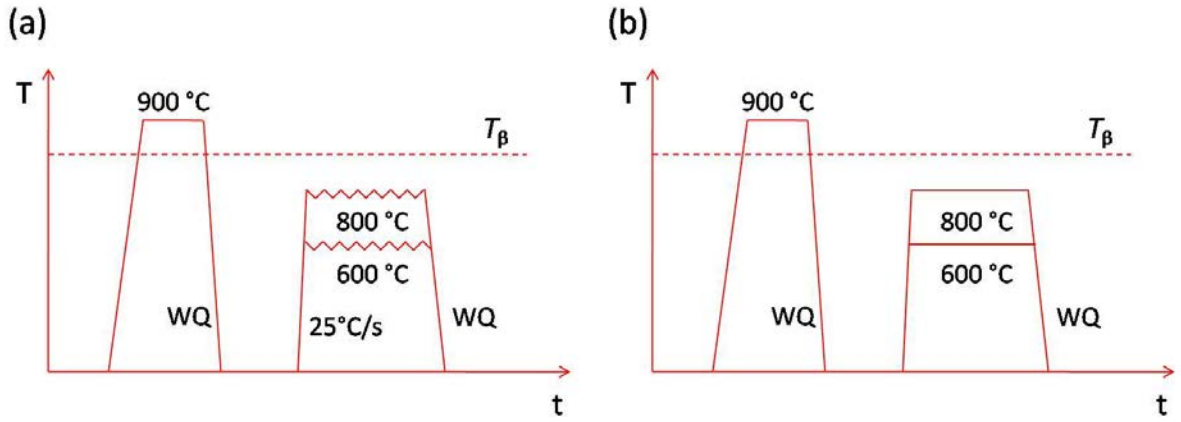

Fig. 2.3 Schematic illustration of the (a) thermomechanical coupling and (b) heat treatment processes.

2.4.2.2 Thermal mechanical and thermal treatments

Compression was applied isothermally at two temperatures, 800°C and 600°C, as shown in Fig. 2.3, using a Gleeble-3500 thermo-mechanical simulator (Fig. 2.4 (a)). At each temperature, the hot compression was performed at two different strain rates to two different strains. The detailed deformation parameters are given in Table 2.4.

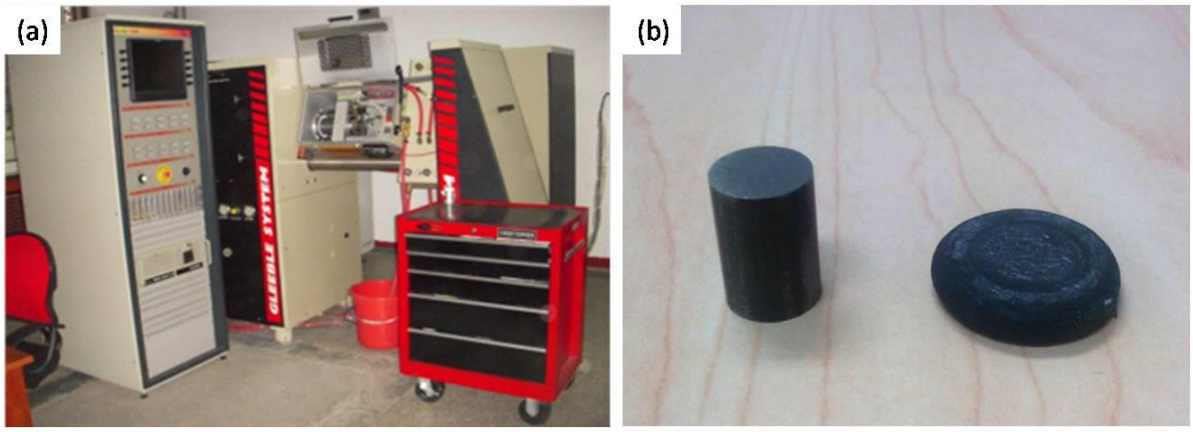

Fig. 2.4 (a) Gleeble-3500 thermo-simulator system; (b) Samples before and after thermo-simulator compression test.

Prior to each compression, the specimens were heated to the isothermal temperatures at a rate of 25°C/s and then held for 10s before the commencement of the deformation to ensure a homogeneous temperature field. The deformation temperature was measured by a thermocouple welded to the surface of the central part of the cylinder. Graphite foils were put between the anvil and the specimen in order to reduce the friction, to improve deformation

homogeneity, and to prevent sticking. The deformation strain, temperature and strain rate were automatically controlled and recorded by the Gleeble-3500 thermal simulator system. After compression, all specimens were immediately cooled in water in order to retain the deformed microstructures.

Table 2.4 Detailed hot compression parameters.

Temperature (°C)	Strain rate (s^{-1})	Strain	Corresponding isothermal holding time (min)	Cooling
800	0.0005	0.7	23	WQ
	0.0005	1.2	40	
	0.001	1.2	11.5	
600	0.001	0.7	11.5	
	0.01	0.7	1.2	
	0.001	1.2	20	

As references, the same number of specimens with the same initial microstructure were heat treated at 800°C and 600°C, respectively, under the same thermal conditions as those of the hot compressions. The detailed treatment parameters are given in Table 2.5.

For the only heat treated specimens, the heat treatments were performed using the OTF-1200X tube furnace. The samples were loaded into the furnace when the set temperature of the furnace was reached.

Table 2.5 Detailed Heat treatment parameters.

Temperature (°C)	isothermal holding time (min)	Cooling
800	23	WQ
	40	
	11.5	
600	11.5	
	1.2	
	20	

2.5 Microstructural characterization methods

The characteristics of microstructural evolution were studied in the aspect of morphology, size, distribution, chemical composition and crystallography from macroscopic scale to nano scale. Depending on the spatial resolution and features of specific microstructures, different characterization techniques, including optical microscopy, electron microscopy and neutron diffraction, scanning electron microscope (SEM) and transmission electron microscope (TEM) are used to thoroughly characterize the structure of β and the phase transformation under deformation conditions.

2.5.1 Sample preparation by mechanical polishing

All the specimens were cut in two halves parallel to the specimen cylindrical axis by wire electrical discharge cutting. Microstructural examinations were performed in the centre of the surfaces indicated by "***A***" in Fig 2.5.

For bulk specimens, the sample surfaces were first mechanically ground using SiC papers with grit sizes from 80 to 4000. In order to achieve the surface quality required for optical microscopic, SEM and EBSD examinations, the samples were electro-polished with a solution of 20% perchloric acid in methanol using a voltage of 25V for 10s at 5°C. For the SEM/EDX analyses, further polishing with oxide polishing suspension (OPS) was carried out in order to remove the surface relieves. The OPS polishing was conducted using an automatic polishing machine (Struers Tegramin-25) at a rotation speed of 200~300 rpm for 20 min. The polished specimens were rinsed with tap water for 5min and cleaned in ethanol in an ultrasonic bath for 15 min.

For TEM thin foils samples with a thickness of 1mm were cut from the bulk specimens and discs with a diameter of 3mm diameter were punched off the thin plates. Then, the samples were mechanically thinned using 800 and 2000 grit SiC papers to attain a final thickness of approximate 60μm. The prepared samples were finally electro-polished with a Struers

Tenupol-5 twin-jet electropolisher at –35°C in a solution of 20% perchloric acid in methanol at a voltage of 10V to perforation.

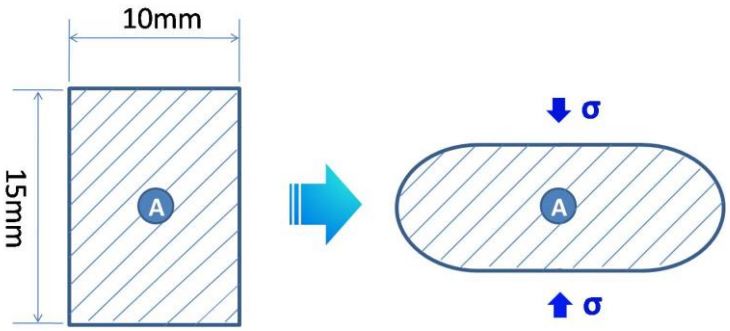

Fig. 2.5 Samples for microstructural examinations inheat treated specimens (left) andhot compressed specimens (right). The region of interest is indicated by "***A***".

2.5.2 Optical microscopic examination

The OLYMPUS/PMG3 optical microscope (OM) was used to examine the microstructure at low magnifications of the treated alloy. After mechanical polishing, the samples were cleaned in alcohol for 5~10 minutes using ultrasonic cleaning device and chemically etched with a modified solution of 10 Vol.% HF, 10 Vol.% HNO_3 and 80 Vol.% H_2O.

2.5.3 Neutron diffraction

Neutron diffraction measurements were performed at room temperature, using the texture and stress diffractometer STRESS-SPEC at Heinz Maier-Leibnitz Zentrum (MLZ), Germany, to determine the phase constituents and the lattice parameters of the β phase in the solution treated specimen and the those of the α/β phases in aging treated specimen. Monochromatic neutrons (0.1689 nm) were obtained using the Ge (311) monochromator. Diffraction patterns in the 2θ range from 35° to 100° were acquired. The incident beam size was 15mm. During the measurement, the cylindrical specimen of φ10mm×15mm was continuously rotated around the axis of the cylinder. A standard Si powder was measured to obtain the instrumental parameters. The lattice constants of the corresponding phases were refined, using the JANA software package [114].

2.5.4 Scanning Electron Microscopic examinations

Mesoscaled microstructures were examined with a Jeol JSM-6500F and a Zeiss Supra-40 Field Emission Gun Scanning Electron Microscopes (FEG-SEM).

2.5.4.1 Imaging

Imaging was performed in the Backscattered Electron (BSE) and Secondary Electron (SE) modes.

2.5.4.2 Electron Back-Scattered Diffraction (EBSD)

In order to identify the crystallographic features of the microstructural constituents in the treated specimens, EBSD measurements were performed using the Jeol JSM-6500F FEG SEM operated at 20 kV accelerating voltage and quipped with an Oxford EBSD camera and the Aztec online acquisition software package (Oxford Instruments). The measurements were conducted in two modes: beam controlled mode and manual mode.

2.5.4.3 Energy Dispersive X-ray Spectrometric analyses (EDX)

The distributions of the alloying elements in the heat treated and hot deformed microstructures were examined using the Zeiss Supra-40 SEM equipped with a Bruker-QUANTAX SDD- EDX detector and the software Esprit (Bruker), v 1.9.4. Chemical composition mappings were acquired in the areas of 47 μm×100 μm each, with one a step size of 1μm. At each measuring point, the X-ray spectra of Ti, Al, Mo, V, Cr and Fe were recorded.

2.5.5 Transmission Electron Microscopic examination

2.5.5.1 Imaging and electron diffraction

Nano scaled and atomic scaled microstructures were analyzed by transmission electron microscopy (TEM), using a Philips CM 200 TEM, a JEOL JEM-ARM200F high resolution TEM (HRTEM) and an FEI Tecnai G2 F30 HRTEM operated at 200 kV. The crystal structural

analyses were conducted by examining the selected area electron diffraction patterns. The crystallographic orientations of the microstructural constituents were determined by indexing the TEM Kikuchi line patterns, using a home-made software package, Euclid Phantasies (EP), [115, 116] and expressed in a triplet of Euler angles in Bunge notation [117]. The observed traces of the striations in β matrix were identified with trace analysis. To avoid accidental match, at least three specimen tilts were utilized to verify each identified plane.

2.5.5.2 Energy Dispersive X-ray Spectrometric analysis

High-angle annular dark field (HAADF) images were acquired Chemical compositions were analyzed by TEM Energy Dispersive X-ray Spectrometry (EDS) in line and area scanning modes, using an FEI Tecnai G2 F30 HRTEM with an inner and an outer collecting angle of 50 mrad and 180 mrad, respectively. The X-ray spectra of Ti, Al, Mo, V, Cr and Fe were collected and recorded.

2.6 Crystallographic calculation

2.6.1 Basics

Some basic crystallographic calculations and presentations used in the present PhD work are introduced in the following sections.

2.6.1.1 Coordinate systems and coordinate transformation

Five different reference frames were used in these calculations and are defined in the following: the sample coordinate system, the two Bravais lattice bases of the cubic β phase and the hexagonal α phase and the two orthonormal intermediate coordinate systems attached to the lattice bases of the β and α phases.

The sample coordinate system was chosen as AD or CD (Axial Direction or Compression Direction) and RD1/RD2 (two arbitrary Radial Directions as the analyses have been often performed in the centre of the samples). Sometimes it was convenient to use a reference frame,

XYZ, corresponding to the acquired microstructure: X being from left to right, Y from bottom to top and Z out of the plane.

The sample coordinate system and the Bravais lattice basis are related by two coordinate transformations. The first transformation is from the sample coordinate system to the orthonormal crystal coordinate system. This relation between the two coordinate systems is often called crystallographic orientation. It can be expressed with the Euler angles $(\varphi_1, \phi, \varphi_2)$ in Bunge notation [118, 119], which can be directly determined by EBSD measurements. The definition and rotation sequence of the three Euler angles is illustrated in Fig. 2.6. The sequential coordinate transformation matrices are given in Eq. (2-1, 2-2 and 2-3).

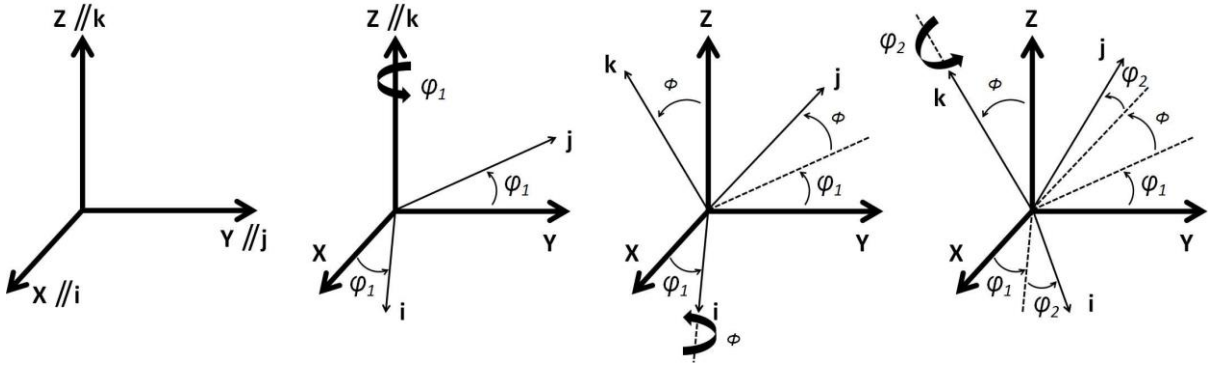

Fig. 2.6 Definition and rotation sequence of Euler angles in Bunge notation.

$$\mathrm{M}_{\varphi_1} = \begin{bmatrix} \cos\varphi_1 & \sin\varphi_1 & 0 \\ -\sin\varphi_1 & \cos\varphi_1 & 0 \\ 0 & 0 & 1 \end{bmatrix} \tag{2-1}$$

$$\mathrm{M}_{\phi} = \begin{bmatrix} 1 & 0 & 0 \\ 0 & \cos\phi & \sin\phi \\ 0 & -\sin\phi & \cos\phi \end{bmatrix} \tag{2-2}$$

$$\mathrm{M}_{\varphi_2} = \begin{bmatrix} \cos\varphi_2 & \sin\varphi_2 & 0 \\ -\sin\varphi_2 & \cos\varphi_2 & 0 \\ 0 & 0 & 1 \end{bmatrix} \tag{2-3}$$

By multiplication of these three matrices in proper sequence, the final expression is obtained that links the sample coordinate system with the orthonormal crystal coordinate system.

$$\mathrm{M}_E=\begin{bmatrix} \cos\varphi_1\cos\varphi_2-\sin\varphi_1\sin\varphi_2\cos\phi & -\cos\varphi_1\sin\varphi_2-\sin\varphi_1\cos\varphi_2\cos\phi & \sin\varphi_1\sin\phi \\ \sin\varphi_1\cos\varphi_2+\cos\varphi_1\sin\varphi_2\cos\phi & -\sin\varphi_1\sin\varphi_2+\cos\varphi_1\cos\varphi_2\cos\phi & -\cos\varphi_1\sin\phi \\ \sin\varphi_2\sin\phi & \cos\varphi_2\sin\phi & \cos\phi \end{bmatrix} \quad (2\text{-}4)$$

The second transformation is from the orthonormal crystal coordinate system to the Bravais lattice basis. In the present study, there are two phases: β and α. For β phase, $a=b=c$, $\alpha=\beta=\gamma=90^{\circ}$, thus the coordinate transformation matrix from the orthonormal crystal coordinate system to the lattice basis is

$$M_C^{\beta}=\begin{bmatrix} a & 0 & 0 \\ 0 & a & 0 \\ 0 & 0 & a \end{bmatrix} \quad (2\text{-}5)$$

For α phase, $a=b\neq c$, $\alpha=\beta=90^{\circ}$, $\gamma=120^{\circ}$, the coordinate transformation is

$$M_C^{\alpha}=\begin{bmatrix} \frac{\sqrt{3}}{2}a & 0 & 0 \\ -\frac{1}{2}a & a & 0 \\ 0 & 0 & c \end{bmatrix} \quad (2\text{-}6)$$

In general, let the vector $[uvw]$ be in the lattice basis (abc) and the same vector $[xyz]$ in the sample coordinate system (ijk). Since, the coordinate transformation does not change the length and direction of the vector, it follows that

$$ua+vb+wc=xi+yj+zk \quad (2\text{-}7)$$

The coordinate transformation can be made by:

$$\begin{bmatrix} x \\ y \\ z \end{bmatrix} = M_E M_C^{\alpha/\beta} \begin{bmatrix} u \\ v \\ w \end{bmatrix} \tag{2-8}$$

2.6.1.2 Stereographic projection and traces determination

The stereographic projection is a particular mapping that projects a sphere onto a plane, which can be used to project a vector (or a plane normal) to the equatorial plane, as shown in Fig. 2.7, and is one of the projection methods to plot pole figures. To calculate the projection of a crystalline plane to the sample surface in the sample coordinate system, the vector normal to the plane has to be expressed in the macroscopic coordinate system set with the sample surface as the equatorial plane. For instance, a vector normal to the plane (hkl) is $V_P = (hkl)^*$. The corresponding vector in the sample coordinate system V_S can be calculated using Eq. (2-9).

$$V_S = M_E S_i M_C G^* V_P \tag{2-9}$$

Here, M_E is the Euler angle matrix, M_C is the coordinate transformation matrix from the orthonormal crystal coordinate system to the Bravais lattice basis. S_i is one of the rotational symmetry matrices of the crystal system represented in **Appendix**, G^* is the metric tensor in reciprocal space.

As presented in Fig. 2.7(a), vector ***OP*** represents the vector V_S ($OP = V_S$). ***P*** is the intersection of vector ***OP*** with the sphere and is defined as the pole of plane (hkl). Let the line connecting point ***P*** and the South Pole ***S*** be line ***PS***. Line ***PS*** intersect the equatorial plane at point ***P'***. ***P'*** is the stereographic projection of pole ***P***. On the equatorial plane, ***P*** is expressed with the polar angle θ and the azimuth angle ϕ (θ , ϕ), where

$$\theta = \arccos\left(\frac{ON \cdot OP}{|ON| \cdot |OP|}\right) \tag{2-10}$$

and

$$\varphi = \frac{\pi}{2} - \arccos\left(\frac{OE \cdot OP'}{|OE| \cdot |OP'|}\right) \tag{2-11}$$

Line ***HK*** vertical to vector ***OP'*** in the equatorial plane represents the trace of plane (*hkl*) (Fig. 2.7(b)).

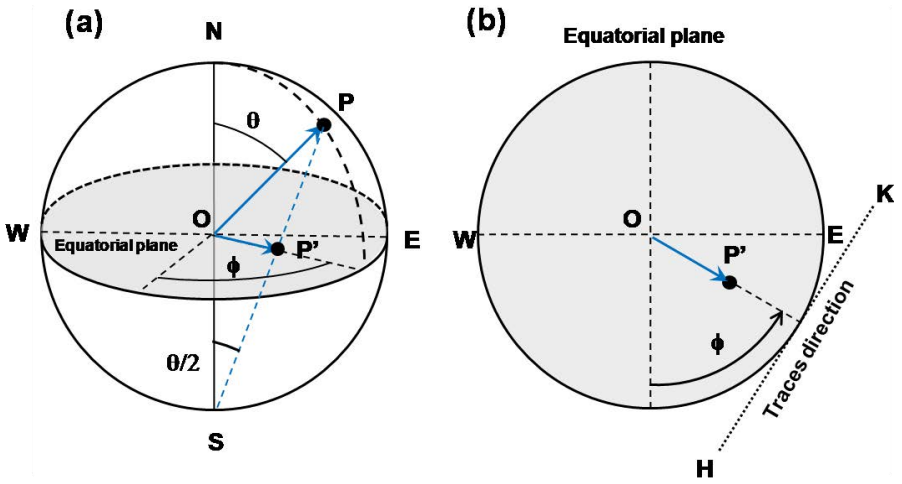

Fig. 2.7 Illustration of stereographic projection, where, ***P*** is the pole of vector ***OP*** on the sphere and ***P'*** is its stereographic projection of the equatorial plane and Line ***HK*** is the trace of the plane that is normal to ***OP***. [120]

2.6.1.3 Misorientation

The misorientation between two crystals can be defined by sets of rotations from one of the symmetrically equivalent coordinate systems of one crystal to one of equivalent coordinate systems of the other crystal. It can be calculated, using the experimentally determined orientations of the concerning crystals with respect to the macroscopic sample coordinate system, as illustrated in Fig. 2.8. In the case of EBSD orientation determination under the convention of Oxford-Channel 5, the orientations of the crystals are characterized

by a set of Euler angles $(\varphi_1, \phi, \varphi_2)$ in Bunge's convention [118]. In the present study, this method was employed to calculate the misorientation between two α variants.

From the Fig. 2.8, the misorientation matrix ΔM going from crystal A to crystal B can be defined as follows:

$$\Delta M = S_i^{-1} M_A^{-1} M_B S_j \tag{2-12}$$

where M_A and M_B are the Euler angle matrices from the sample coordinate system to the respective orthonormal coordinate system set to the crystal lattice basis, S_i and S_j are the rotational symmetry matrices.

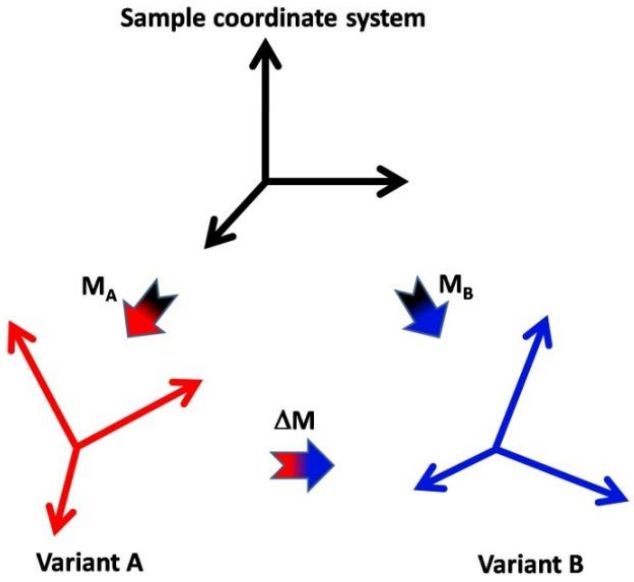

Fig. 2.8 Schematics of misorientation between two α variants. (Change Variant A to crystal A and Variant B to crystal B)

Misorientation expressed in angle and rotation axis is of particular interest for the present work, as it brings first information about orientation relationship between crystals. The determination of the angle and axis is explained as follows [121]. If we denote the misorientation matrix

$$\Delta M = \begin{bmatrix} g_{11} & g_{12} & g_{13} \\ g_{21} & g_{22} & g_{23} \\ g_{31} & g_{32} & g_{33} \end{bmatrix} \tag{2-13}$$

The misorientation angle θ and rotation $\mathrm{r}(\mathrm{r}_1, \mathrm{r}_2, \mathrm{r}_3)$ expressed in the orthonormal coordinate system can be calculated:

$$\theta = \arccos\left(\frac{g_{11} + g_{22} + g_{33} - 1}{2}\right) \tag{2-14}$$

(1) $\theta = 180^\circ$

$$r = (\mathrm{r}_1, \mathrm{r}_2, \mathrm{r}_3) = \left(\pm\sqrt{\frac{g_{11}+1}{2}}, \pm\sqrt{\frac{g_{22}+1}{2}}, \pm\sqrt{\frac{g_{33}+1}{2}}\right)$$
$$\text{with} \quad r\begin{pmatrix} |\mathrm{r_m}| = \max\left(|\mathrm{r_i}|, \mathrm{i} = 1,2,3\right) \\ \mathrm{r_m} > 0, \text{by convention} \\ \forall \mathrm{i} \neq \mathrm{m}, \mathrm{sgn}(\mathrm{r_i}) = \mathrm{sgn}(\mathrm{g_{im}}) \end{pmatrix} \tag{2-15}$$

(2) $\theta = 0^\circ$

$$r = (\mathrm{r}_1, \mathrm{r}_2, \mathrm{r}_3) = (1, 0, 0) \tag{2-16}$$

(3) $\theta \neq 180^\circ$ and $\theta \neq 0^\circ$

$$r = (\mathrm{r}_1, \mathrm{r}_2, \mathrm{r}_3) = \left(\frac{g_{23} - g_{32}}{2\sin\theta}, \frac{g_{31} - g_{13}}{2\sin\theta}, \frac{g_{12} - g_{21}}{2\sin\theta}\right) \tag{2-17}$$

2.6.2 Trace analysis in TEM observation

In the present work, slip planes and some planar defects were identified with trace analysis method, using the known orientation of the crystal. The analysis was carried out by first calculating the theoretical trace orientation of all possible rational indexed crystalline planes of

the corresponding phase in TEM or SEM screen reference system using the determined crystallographic orientation and second matching them with the observed traces [122]. The plane having best matched trace with the observed one was determined as the plane giving rise to the planar defects or the slip plane.

For the determination by TEM examination, the calculation is realized by first constructing the coordinate transformation matrix from the screen coordinate system to the crystal basis that is decomposed into following three steps: the transformation from the image coordinate system to the sample holder coordinate system, the transformation from the sample coordinate system to the orthonormal crystal coordinate system and transformation from the orthonormal crystal coordinate system to the Bravais lattice basis of the crystal. For BCC structure, the third step is not necessary. Thus the transformation matrix, $M_{I\to C}$, from the TEM image coordinate system to the crystal basis for BCC crystals can be obtained:

$$M_{I\to C} = M_{I\to S} \cdot M_{S\to C} \tag{2-18}$$

Where $M_{I\to S}$ is the coordinate transformation matrix from the image coordinate system to the sample holder position. $M_{S\to C}$ is the coordinate transformation matrix from the sample holder coordinate system to the crystal coordinate system. The transformation from the image coordinate system to the sample holder coordinate system depends on the operation that includes the magnetic rotation (if it is not corrected by the TEM) and the tilts of the sample holder. The coordinate transformation from the sample holder position to the crystal system can be performed based on the experimentally determined orientation of the crystal with respect to the sample holder. The orientation of the crystal was directly determined, in the present work, by indexing the Kikuchi line pattern using the software Euclid Phantasies (EP) [115, 116]. Three Euler angles representing the three rotations transforming the sample holder coordinate system to the crystal reference linked to the crystal lattice basis are given by the software.

Secondly, with the transformation matrix, the coordinates of the plane normal in the image

coordinate system can be calculated and then the coordinates of the intersection of the plane with the screen can be calculated by vector production of the plane normal and the screen normal. Finally the calculated trace is compared with the observed ones.

2.6.3 Deduction of orientation of β phase from orientation relationship and measured orientation of α phase

During the β→α transformation, one initial β grain could transform into several differently orientated α variants under a specific orientation relationship between the two phases. Normally, the orientation relationship (OR) is expressed with a pair of parallel planes of the respective β and α phase and a pair of in plane directions of the two phases. As illustrated in Fig. 2.9, plane $\boldsymbol{P}(hkl)_\beta$ of the β phase is parallel to plane $\boldsymbol{P'}(hkl)_\alpha$ of the α phase. The direction $[uvw]_\beta$ in plane $\boldsymbol{P}$ of β phase is parallel to the direction $[uvw]_\alpha$ in plane $\boldsymbol{P'}$ of α phase. To derive the transformation matrix from the β phase crystal reference frame to that of the α phase under the defined orientation relationship, an orthonormal coordinate system is needed that can be set based on OR parallel plane and the OR direction in either phase.

As shown in Fig. 2.9, the orthonormal reference frame is set such that the basis vector $\mathbf{e}_2$ is parallel to the crystal direction $[uvw]_\beta$ and $[uvw]_\alpha$. The basis vector $\mathbf{e}_3$ is parallel to the normal direction of plane $\boldsymbol{P}$ and $\boldsymbol{P'}$($\mathbf{n}\left(hkl\right)_\beta$ and $\mathbf{n}\left(hkl\right)_\alpha$). The axis $\mathbf{e}_1$ is parallel to the vector cross product of $[uvw]_\beta$ and $\mathbf{n}\left(hkl\right)_\beta$, and of $[uvw]_\alpha$ and $\mathbf{n}\left(hkl\right)_\alpha$. Under the given orientation relationship, the following relation holds:

$$M_E^\beta S_i^\beta M_C^\beta T_\beta = M_E^\alpha S_j^\alpha M_C^\alpha T_\alpha \tag{2-19}$$

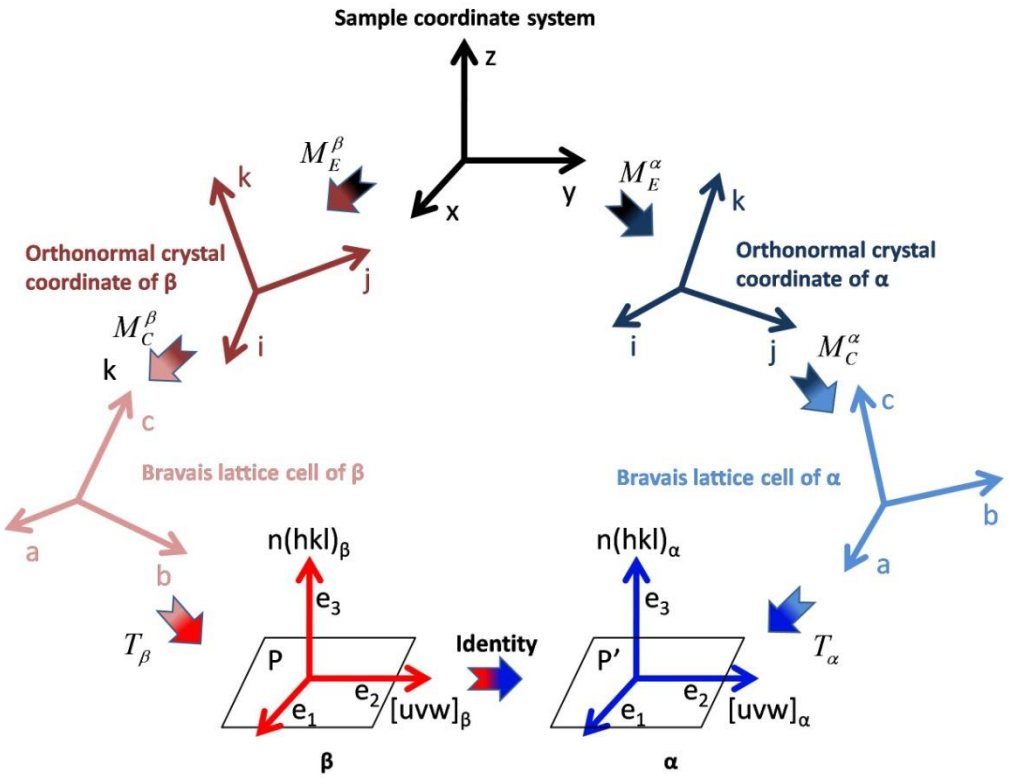

Fig. 2.9 Schematic illustration of the orientation relationship (OR) between β and α.

Knowing the orientation of the α variants, the orientation of the β phase with respect to the sample coordinate system expressed in matrix can be calculated with Eq. (2-20)

$$M_E^\beta = M_E^\alpha S_j M_C^\alpha T_\alpha (T_\beta)^{-1} (M_C^\beta)^{-1} (S_i)^{-1} = M_E^\alpha S_j M_C^\alpha T_{\alpha\to\beta} (M_C^\beta)^{-1} (S_i)^{-1} \qquad (2\text{-}20)$$

Where, M_E^α is the Euler angle matrix of α phase, which can be determined by SEM-EBSD. S_i and S_j are the rotational symmetry elements of cubic crystal system (β) and hexagonal crystal system (α), respectively. $T_{\alpha\to\beta}$ is the coordinate transformation matrix from α lattice basis to that of β. T_β and T_α are the respective transformation matrix from the Bravais lattice basis of β phase and α phase to the orthonormal OR reference system. M_C^β and M_C^α are the transformation matrix from the orthonormal crystal coordinate system to the respective Bravais lattice basis of β phase and α phase.

With Eq. (2-20), the orientation of the β phase from the measured orientations of the α variants can be derived if the OR between the two phases is known. In practice, one α orientation can produce several β orientations, due the crystal symmetry. For an unambiguous determination, several (up to 4) α variants that are inherited from one β may be needed. In this case, the common β orientation produced by the orientations of the selected variants is the realistic orientation of the β phase.

2.6.4 Transformation deformation gradient tensor

The β→α transformation could be considered as a displacive transformation realized by coordinated atomic movements from BCC structure to HCP structure. As shown in Fig. 2.10, the transformation can be regarded as the deformation of the lattice cell of β chosen based on the OR reference frame to the lattice cell of α based on the OR reference frame by homogeneous lattice distortion. To analysis the lattice distortion during β phase transformation, an orthonormal coordinate system (i-j-k) is set to the OR basis, as shown in Fig. 2.10.

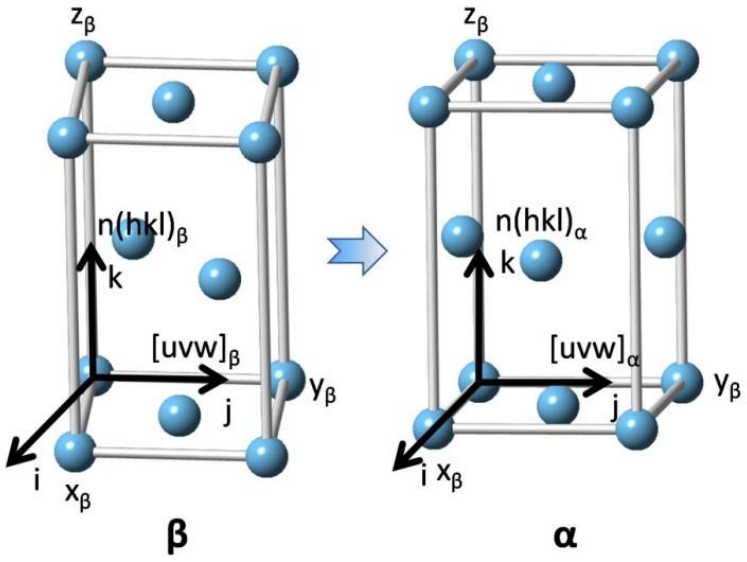

Fig. 2.10 Schematics of β→α transformation through homogeneous lattice distortion.

Under Burgers OR (BOR), the lattice cell of β in Fig. 2.10 is monoclinic, whereas that of

α is orthorhombic. By examining the correspondences of the basis vectors of the lattice cell before transformation and after transformation, the lattice distortion can be established. Before transformation the basis vectors can be expressed with Eq. (2-21) and those after transformation can be expressed with Eq. (2-22).

$$\begin{cases} x_\beta = x_{\beta x} \cdot i + x_{\beta y} \cdot j + x_{\beta z} \cdot k \\ y_\beta = y_{\beta x} \cdot i + y_{\beta y} \cdot j + y_{\beta z} \cdot k \\ z_\beta = z_{\beta x} \cdot i + z_{\beta y} \cdot j + z_{\beta z} \cdot k \end{cases} \tag{2-21}$$

$$\begin{cases} x_\alpha = x_\alpha \cdot i + 0 \cdot j + 0 \cdot k \\ y_\alpha = 0 \cdot i + y_\alpha \cdot j + 0 \cdot k \\ z_\alpha = 0 \cdot i + 0 \cdot j + z_\alpha \cdot k \end{cases} \tag{2-22}$$

Then the transformation deformation gradient tensor expressed in the reference frame of $(i\text{-}j\text{-}k)$ can be obtained as follows:

$$A = \begin{bmatrix} e_{11} & e_{12} & e_{13} \\ e_{21} & e_{22} & e_{23} \\ e_{31} & e_{32} & e_{33} \end{bmatrix} = \begin{bmatrix} \dfrac{x_\alpha}{x_\beta} & \dfrac{-y_{\beta x}}{y_\beta} & \dfrac{-z_{\beta x}}{z_\beta} \\ \dfrac{-x_{\beta y}}{x_\beta} & \dfrac{y_\alpha}{y_\beta} & \dfrac{-z_{\beta y}}{z_\beta} \\ \dfrac{-x_{\beta z}}{x_\beta} & \dfrac{-y_{\beta z}}{y_\beta} & \dfrac{z_\alpha}{z_\beta} \end{bmatrix} \tag{2-23}$$

The components of the deformation gradient tensor represent dilatations and shears. The components $e_{ij}\left(i = j\right)$ stand for the normal strain that represent the dilatation along *i* directions normal to the plane perpendicular to *j*. The components $e_{ij}\left(i \neq j\right)$ are shear strains that indicate the shears in *i* direction and in the plane normal to *j*.

2.7 Related analyzing software

Quantitative measurements of α area fraction were carried out using the Image-Pro-Plus

analysis software [123]. The atomic correspondences and single crystal electron diffraction were analyzed and simulated using the Crystalmaker software package [124]. The numerical calculations were programmed with the Matlab [125].

Chapter 3 Distortion induced striations in β phase

3.1 Introduction

Despite the efforts in resolving the complex phase transformations (i.e. β→α, β→β+ω, β→β+β', and β→α'') and in gaining knowledge on the produced phases as well as their correlations with the resultant mechanical properties [49, 126, 127, 128, 129, 130, 131], there are still some frequent β associated features visible in TEM diffraction patterns and in bright/dark field images remaining un-addressed [12, 57, 79, 80, 81].

In this chapter, motivated by such observations, the striations of β phase in Ti-5553 alloy revealed by TEM diffraction contrast have been studied in depth from macroscopic scale by in-volume neutron diffraction to atomic scale by high resolution TEM (HRTEM). A thorough investigation was made with an aim to elucidate the origin of the striations of the β phase and to clarify its structural characteristics.

3.2 Detailed specimen parameters

The specimens were solution treated at 1000°C and 900°C, respectively, for 30min and then cooled with three cooling rates, i.e. water quenching (WQ), air cooling (AC) and liquid nitrogen quenching (LNQ). The detailed cooling manners are given in Table 3.1.

Table 3.1 Detailed solution treatment parameters. WQ: water quenching; AC: air cooling and LNQ: liquid nitrogen quenching.

Temperature (°C)	Time (min)	Cooling
900	30	WQ/AC/LNQ
1000		WQ

Three of the 900°C solutionized and water quenched specimens were further aged at 800°C, 600°C and 350°C, respectively and quenched in water. The detailed heat treatment parameters

are displayed in Table 3.2. Finally, the characterizations of microstructural evolution on micro-/nano-scale, phase nucleation and orientation relationship of these specimens were analyzed by SEM, EBSD and TEM.

Table 3.2 Aging treatment parameters after solution treatment at 900°C.

Temperature (°C)	Time (min)	Cooling
600/800	30	WQ
350	120	

3.3 Results and discussion

3.3.1 Microstructural characteristics

The microstructure of the present (α+β) forged Ti-5553 is characterized by the typical constituents of metastable β titanium alloys, consisting of large globular and rod-like α particles, as shown in Fig. 3.1(a). Between coarse α phase, fine needle shaped α precipitates can be seen in the magnified micrograph (Fig. 3.1(b)). Both are distributed homogeneously in the β matrix.

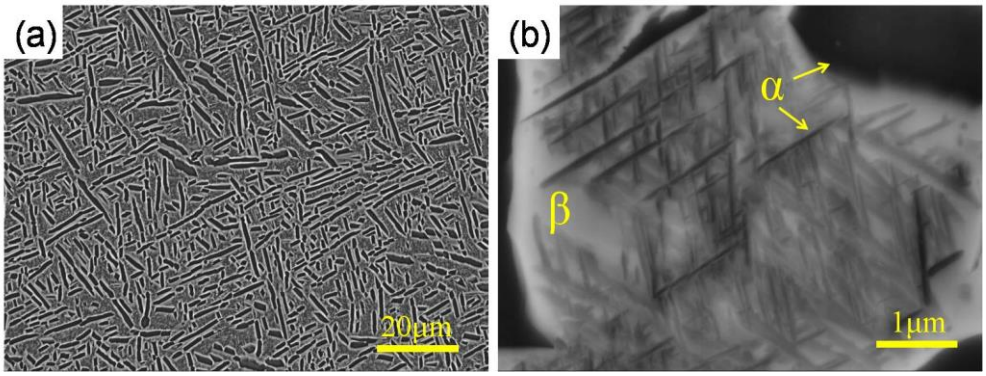

Fig. 3.1 SEM backscattered electron (BSE) micrographs of As-forged of Ti-5553 alloy. There are two morphologies of the α phase: (a) large globular and rod-like and (b) fine needle shaped α between coarse α.

After the specimen was solution treated at 900°C for 30 min and quenched in water, all α constituents dissolve into the β matrix, as shown in Fig. 3.2(a). Only equiaxed β grains with an average grain size of ~350 μm are present. This is confirmed by the in-volume neutron diffraction analysis. The diffraction pattern is shown in Fig. 3.2(b). Only the β phase having BCC structure with lattice constant a=3.2355Å is identified.

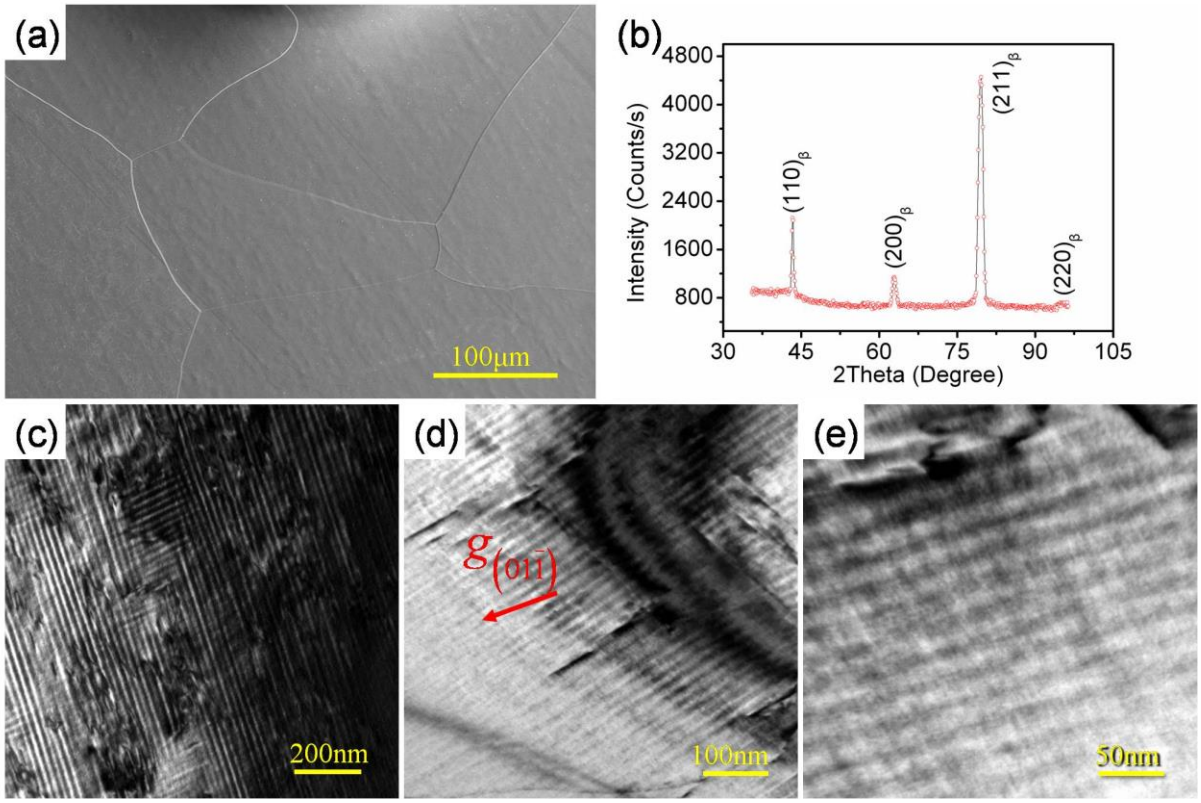

Fig. 3.2 (a) SEM secondary electron (SE) micrograph of Ti-5553 alloy after solution treatment (holding at 900°C for 30 minutes and quenching in water), showing single β phase having equiaxed grains. (b) Neutron diffraction pattern. (c) TEM bright field micrograph showing the striated structure in β grains. (d) TEM bright field micrograph showing the improved contrast of the striations cross the $(01\bar{1})_\beta$ extinction contour (the dark thick lines), where the deviation of the $(01\bar{1})_\beta$ reflecting plane from the Bragg position, s_g, is zero and the two beam condition is approximately met. The reciprocal vector $\mathbf{g}_{(01\bar{1})}$ is indicated. (e) Magnified TEM bright field micrograph showing fine strips within the striations.

However a close examination by TEM revealed that large amount of striations with two grey levels are distributed alternatively within all the β matrix, as shown in Fig. 3.2(c). The inter-striation spacing (the width of one pair of dark and light bands) is about several tens of nanometers. The length direction of the striations is not fixed but dependent on the orientation of the crystal. The striations are oriented in more than one direction, forming tweed pattern. They are particularly contrasted in the vicinity of extinction contours, for example the $(01\bar{1})_\beta$ extinction contour in Fig. 3.2(d). In fact within the extinction contours, the two beam condition and the zero deviation of the reflecting plane from the Bragg position (s_g=0) are approached. Although the contrast of the striations can be distinguished, the edges of each striation are not

sharply defined, not like in the case of dislocations or stacking faults where the contrast change is sharp [132]. Moreover within the striations, the contrast is not constant, as shown in Fig. 3.2(e), the magnified image of an area in Fig. 3.2(d). Fine strips are found to run in two directions. The fact that these fine structures become contrasted in the area very close to the extinction contour where the s_g=0 and the two beam condition are approximately satisfied indicates that these contrasts are of crystallographic origin. Dislocations with higher contrast can also be seen in the striated regions. Comparing Fig. 3.2 with Fig. 3.1, we can see that the striated structure does not bear any morphological or distributional resemblances to the two scaled α particles in the as-forged microstructure. This fact rules out the possibility that the striations are the residual α regions that did not fully transform to β during solution treatment.

The effects of other solution treatment parameters, like temperature and cooling rate were further studied. A higher temperature (1000°C) followed by WQ and other two cooling manners (AC and LNQ) after treated at 900°C were performed. As shown in Fig. 3.3, the occurrence of the striations is independent either of the solution temperature or the cooling manner. Fine parallel striations can be observed in all the three samples, similar to the microstructure in Fig. 3.2. This indicates that the striations are an intrinsic character of the β phase. Moreover, the spacing between the striations is always of the same order of magnitude.

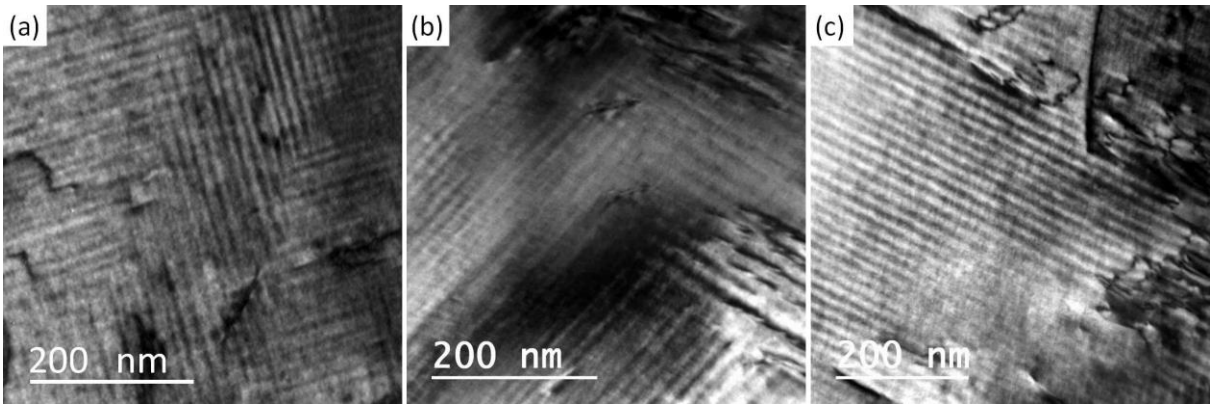

Fig. 3.3 TEM bright field micrographs of Ti-5553 alloy solution treated at (a) 900°C for 30 min followed by air cooling, (b) 900°C for 30 min followed by quenching in liquid nitrogen and (c) 1000°C for 30 min followed by water quenching.

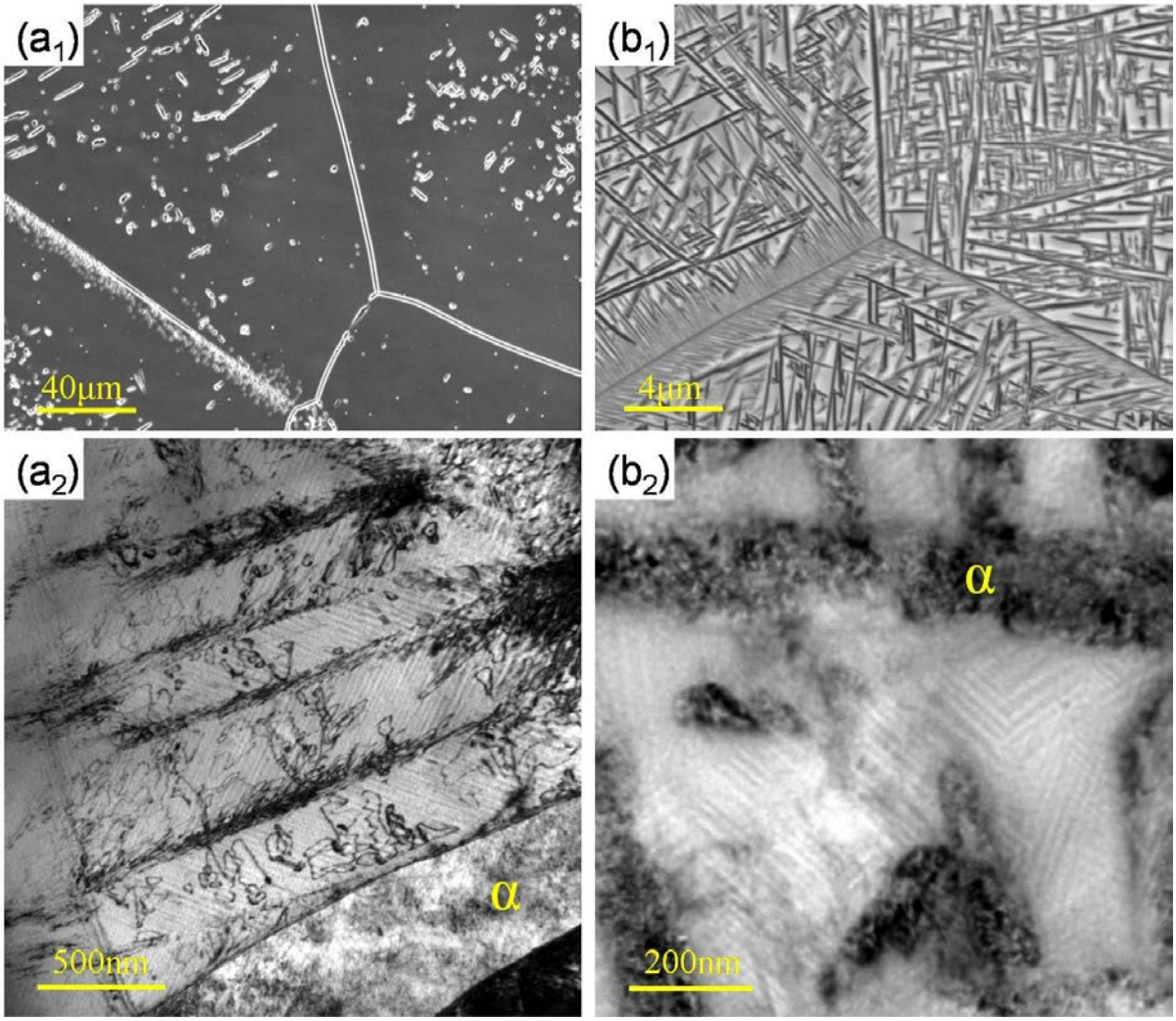

Fig. 3.4 (a_1) SEM secondary electron (SE) and (a_2) TEM micrograph of Ti-5553 alloy aged at 800°C for 30 min. (b_1) SEM secondary electron (SE) and (b_2) TEM micrograph of Ti-5553 alloy aged at 600°C for 30 min.

Considering that the β phase is obtained by fast cooling after solution treatment, the oversaturation of α stabilizing elements in the β phase, like Al, may have some influence on the formation of the striated structure. To verify this possibility, the two aged specimens (aged at 800°C and 600°C, respectively) were examined. The microstructures obtained using SEM and TEM are shown in Fig. 3.4. It is seen that with the decreasing ageing temperatures, the amount of α phase increases. The precipitation sites and morphologies of the α phase for the two ageing conditions are typical of those of metastable β titanium alloys [83, 133]. When ageing temperature is high (Fig. 3.4(a_1)), α phase forms mainly at β grain boundaries and occasionally in the grain interiors. When the ageing temperature is low, large number of plate shaped α form in the interior of the β grains and the Widmanstätten α precipitates are observed along certain β

grain boundaries (Fig. 3.4(b_1)). However, TEM examinations revealed that besides the formation of larger amount of dislocations, the remaining β phase still contains striations as seen in Fig. 3.4(a_2) and Fig. 3.4(b_2) as the case of the solution treated β phase. This indicates that the striations are not related to the oversaturation of the α stabilizing elements. Moreover, the formed α phase does not show any morphology of parallel lamellas.

3.3.2 Chemical composition distribution characteristics

Some authors have hypothesized that the striation maybe related to the spinodal decomposition of the β phase [81]. In this case, the striations should be associated with composition oscillation of the alloying elements in the β phase. To verify it, STEM-HAADF-EDS measurements were performed on the solution treated specimen. The line profiles of the distribution of Ti, Al, V, Cr, Mo and Fe across the striations do not display any repartition of these elements from one striation to another. Fig. 3.5 shows one example of the measurements. This result excludes the chemical origin of the striations. The striated structure of the β phase has no relation with spinodal decomposition.

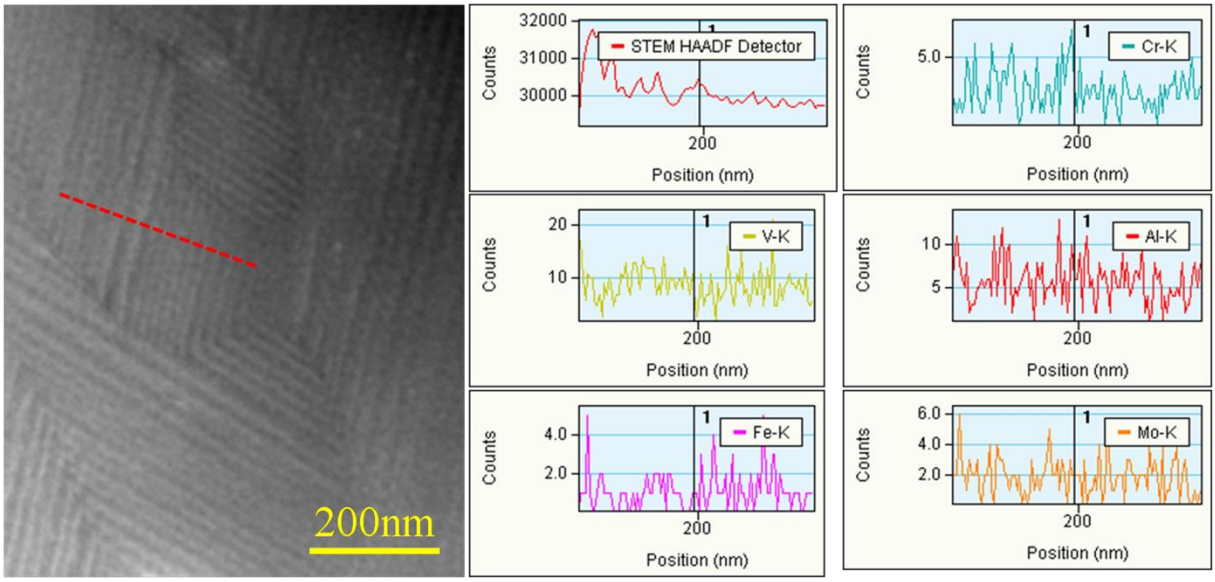

Fig. 3.5 STEM HAADF image of the striated structure in solution treated specimen and the EDX line profiles of Cr, V, Al, Fe and Mo measured along the line indicated in the STEM HAADF image.

3.3.3 Identification of substructures in β phase

In order to further explore the possible origins of the striations, several β zone axis TEM SAED patterns, namely $<100>_\beta$, $<011>_\beta$, $<111>_\beta$, $<113>_\beta$, $<133>_\beta$ and $<012>_\beta$, were acquired and analyzed. The typical $[011]_\beta$, $[113]_\beta$, and $[012]_\beta$ patterns frequently used in the literature are given in Fig. 3.6. It is seen that in each pattern, there are three sets of diffraction spots. Among these sets, one is of high intensity spots from the BCC β and the other two of low intensities located at 1/2 β diffraction positions, and at 1/3 and 2/3 β diffraction positions, respectively. The low intensity spots at the 1/2 β diffraction positions are close to the diffraction positions of α phase but not exactly the same (hereafter we denote this diffraction quasi-α diffraction and the corresponding structure quasi-α), whereas the spots at 1/3 and 2/3 β diffraction positions are very close to those of ω phase (hereafter we denote this diffraction quasi-ω diffraction and the corresponding structure quasi-ω). The two sets of diffraction possess one common feature: the presence of fine streaks continuous between the diffraction spots of the β phase and passing through the origin (transmitted beam) of the diffraction pattern. This is the characteristic of scattering effect arising from crystal size [134]. These fine streaks indicate that the domains producing the corresponding 1/2, 1/3 and 2/3 β diffraction are very small. As the sizes of the quasi domains are too small, no visible dark field contrast can be obtained using the diffracted beams. The same situation was also encountered in another study [135].

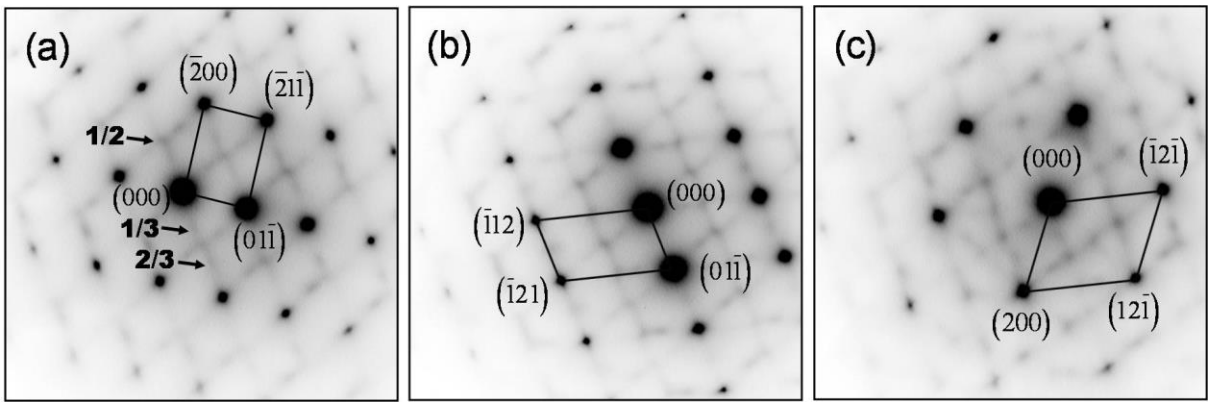

Fig. 3.6 TEM Selected Area Electron Diffraction (SAED) patterns of the striated structure. (a) $[011]_\beta$, (b) $[113]_\beta$, and (c) $[012]_\beta$ zone axis pattern.

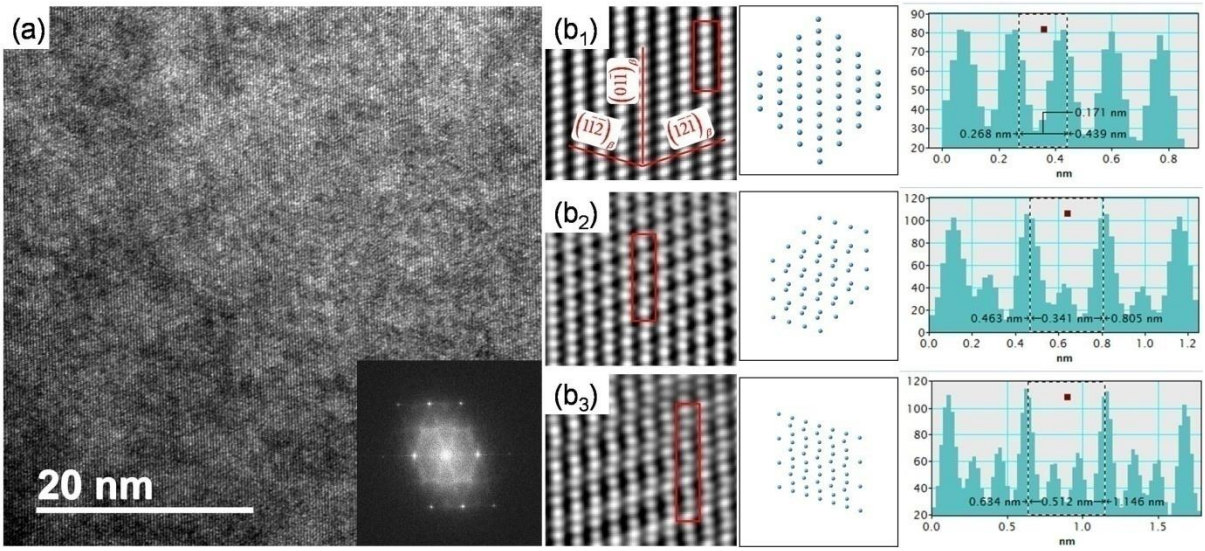

Fig. 3.7 (a) HRTEM micrograph of the striated structure viewed in the $<311>_\beta$ direction. Inset shows a Fast Fourier Transform (FFT) image from the corresponding HRTEM image. (b) Characteristic zones corresponding to the perfect β (b_1), the quasi-α (b_2) and the quasi-ω (b_3) produced by the inverse FFT using the Bragg reflections. The projected atom columns from the modeled structure (perfect β, quasi-α and quasi-ω), and the intensity profiles of the outlined (in red) atom columns.

Fig. 3.7(a) shows a high resolution TEM (HRTEM) micrograph acquired in the area with one of the $<311>_\beta$ directions parallel to the incident beam direction. The insert is the corresponding diffraction pattern generated by the Fast Fourier Transformation (FFT) from the HRTEM image. The pattern well reproduces the characteristics of the corresponding SAED pattern ($<311>_\beta$ pattern) (Fig. 3.6(b)). The image generated by the inverse FFT using the Bragg reflections in the FFT diffraction pattern clearly shows the morphology and the atomic correspondences of the structures giving the β diffraction, the quasi-α diffraction (1/2 β diffraction positions) and the quasi-ω diffraction (1/3 and 2/3 β diffraction positions). The inverse FFT images together with the intensity profiles of the atom columns constituting the $(01\bar{1})_\beta$ plane as marked in the images shown in Fig. 3.7(b). It is seen from the inverse FFT image and the intensity profile in Fig. 3.7(b_1) that for the ideal β phase, the atoms constituting the $(1\bar{1}\bar{2})_\beta$ planes (or $(1\bar{2}\bar{1})_\beta$ planes), with an inter-planar spacing of 1.35Å and $(01\bar{1})_\beta$ planes with an inter-planar spacing of 2.33Å are well in the positions to allow constructive interference of the diffracted electron waves (in phase position). The {112} layers of the BCC structure is clearly visualized. These can be used as references to differentiate the structures

giving the quasi-α diffraction and the quasi-ω diffraction. As seen from Fig. 3.7(b_2), for the quasi-α, every first and third $(1\bar{2}\bar{1})_\beta$ planes in the $(1\bar{2}\bar{1})_\beta$ stacks are well in the BCC positions with an inter-planer spacing of $2d_{(1\bar{2}\bar{1})_\beta}$, whereas the atoms on every second $(1\bar{2}\bar{1})_\beta$ planes are obviously displaced as seen in the outlined zone. The intensity profile also displays decreased intensity of these displaced atoms, indicating that these atoms are out of positions allowing constructive interference of the diffracted waves (out of phase position). Such atomic displacements transform the ideal BCC (β) structure to a two-layered modulated structure and make the additional diffraction spots appear at 1/2 $\{112\}_\beta$ diffraction positions. For the quasi-ω, the displacements happen in two consecutive $(1\bar{2}\bar{1})_\beta$ layers in opposite directions, and the atoms in every first and fourth $(1\bar{2}\bar{1})_\beta$ layers stay in the exact positions of the β BCC structure, as seen in the outlined zone in Fig. 3.7(b_3). The intensity profile also infers that the displaced atoms are no longer in phase positions. Such a structural change forms a three-layered modulation. Due to the structure modulation in the two consecutive $(1\bar{2}\bar{1})_\beta$ planes, additional diffraction spots at the 1/3 and 2/3 β diffraction positions appear. Clearly the two quasi structures are different from the respective hexagonal structure of the ideal α or of the ideal ω.

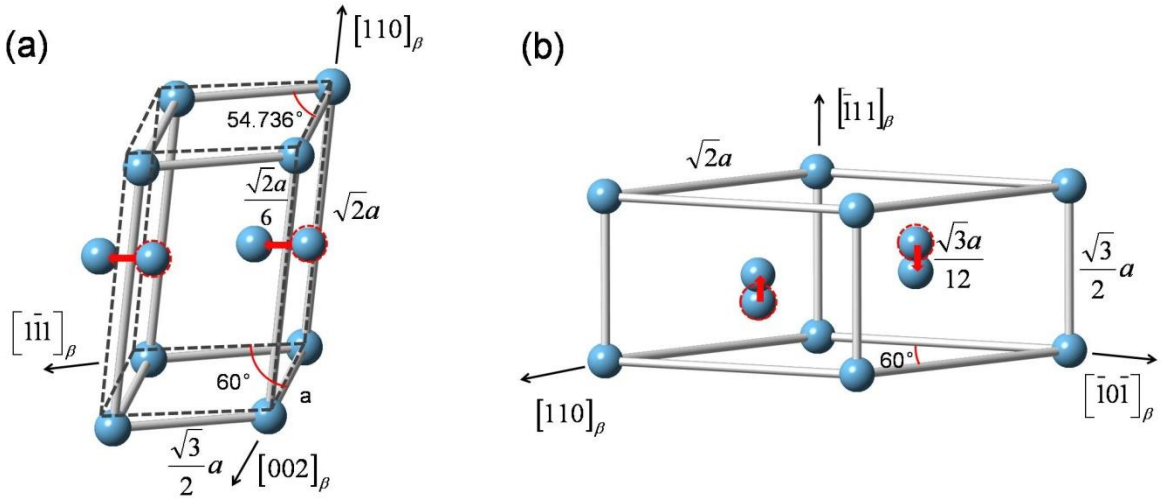

Fig. 3.8 Structural model of (a) quasi-α and (b) quasi-ω with respect to the ideal cubic β structure. For comparison, the ideal α is outlined in dashed lines.

The atomic correspondences revealed by the HRTEM analyses demonstrate that the two-layered modulated structure (quasi-α) and the three-layered modulated structure (quasi-ω)

possess structural resemblance to both the cubic structure of the β phase (for the un-displaced atoms) and the hexagonal structure of the α phase or the ω phase (for the displaced atoms). Based on such characteristics, we modeled the two modulated structures, following the Burgers OR (BOR) between α and β ($\{0001\}_\alpha \parallel \{110\}_\beta$; $\langle 11\bar{2}0\rangle_\alpha \parallel \langle 1\bar{1}0\rangle_\beta$) [136] and the published OR between ω and β ($\{0001\}_\alpha \parallel \{111\}_\omega$; $\langle 11\bar{2}0\rangle_\omega \parallel \langle 1\bar{1}0\rangle_\beta$) [78], as shown in Fig. 3.8. The unit cell of the quasi-α (Fig. 3.8(a)) is encased in one pair of $\{110\}_\beta$ (as basal plane), one pair of $\{112\}_\beta$ planes and one pair of {101} planes (as prismatic planes). The only difference from the cubic structure of the β phase is that the atoms on the $\{110\}_\beta$ between the basal planes are displaced in the $\langle 1\bar{1}0\rangle_\beta$ direction with an amount of $\frac{a}{6}\langle 1\bar{1}0\rangle_\beta$ as indicated in Fig. 3.8(a). For comparison, the ideal α structure is plotted with the dashed lines in the figure. Using this structure model, the diffraction patterns of all acquired zone axes are simulated. With six possible variants (there are 6 distinct $\{110\}_\beta$ planes), all the observed diffraction spots corresponding to the quasi-α are reproduced and properly indexed. As examples, the experimental and simulated <011> and <012> β zone axis diffraction patterns are shown in Fig. 3.9(a_1)(a_2) and Fig. 3.9(b_1)(b_2), where spots from different variants of the quasi-α are in different colors. The $[311]_\beta$ (the $[\bar{1}11]$ for the quasi-α) projection of the atom columns of the quasi-α is given in Fig. 7(b_2). The good match of the modeled structure in both the direct space (Fig. 3.7(b_2)) and the reciprocal space (Fig. 3.9(a_2)(b_2)) validates the structure model of the quasi-α and confirms the existence of the $\frac{a}{6}\langle 1\bar{1}0\rangle_\beta$ atomic displacements on the six distinct $\{110\}_\beta$ planes.

The unit cell of the quasi-ω shown in Fig. 3.8(b) is encased in one pair of $\{\bar{1}11\}_\beta$ (as basal planes), and two pairs of $\{112\}_\beta$ planes (as prismatic planes). The difference from the structure of the ideal β phase is that the atoms on the two $\{211\}_\beta$ (or $\{\bar{1}1\bar{2}\}_\beta$) planes between the prismatic planes are displaced in opposite $[\bar{1}11]_\beta$ directions with a distance between 0 and $\frac{a}{12}[\bar{1}11]_\beta$, as indicated in Fig. 3.8(b). It should be noted that if the displacement is the exact $\frac{a}{12}[\bar{1}11]_\beta$, the 1/3 or 2/3 reflections will disappear in some zone axis patterns and this has not

been found in the present work. As the case of quasi-α, all the diffraction in the 6 zone axis patterns corresponding to quasi-ω are reproduced and properly indexed using 4 variants, as there are 4 distinct $\{111\}_\beta$ planes. Fig. 3.9(a_3) and Fig. 3.9(b_3) show the simulated $<011>_\beta$ and $<012>_\beta$ zone axis patterns. The $[311]_\beta$ (the $[0\bar{1}1]$ for the quasi-ω) projection of the atom columns of the quasi-ω is given in Fig. 3.7(b_3). The good match of the modeled structure in both the direct (Fig. 3.7(b_3)) and the reciprocal space (Fig. 3.9(a_3) and Fig. 3.9(b_3)) validates the structure model of the quasi-ω and confirms the existence of the approximate $\frac{a}{12}[\bar{1}11]_\beta$ displacements on the twelve distinct $\{112\}_\beta$ planes. These two substructures in the β phase may serve as the nuclei for the transformation to the α or the ω phase.

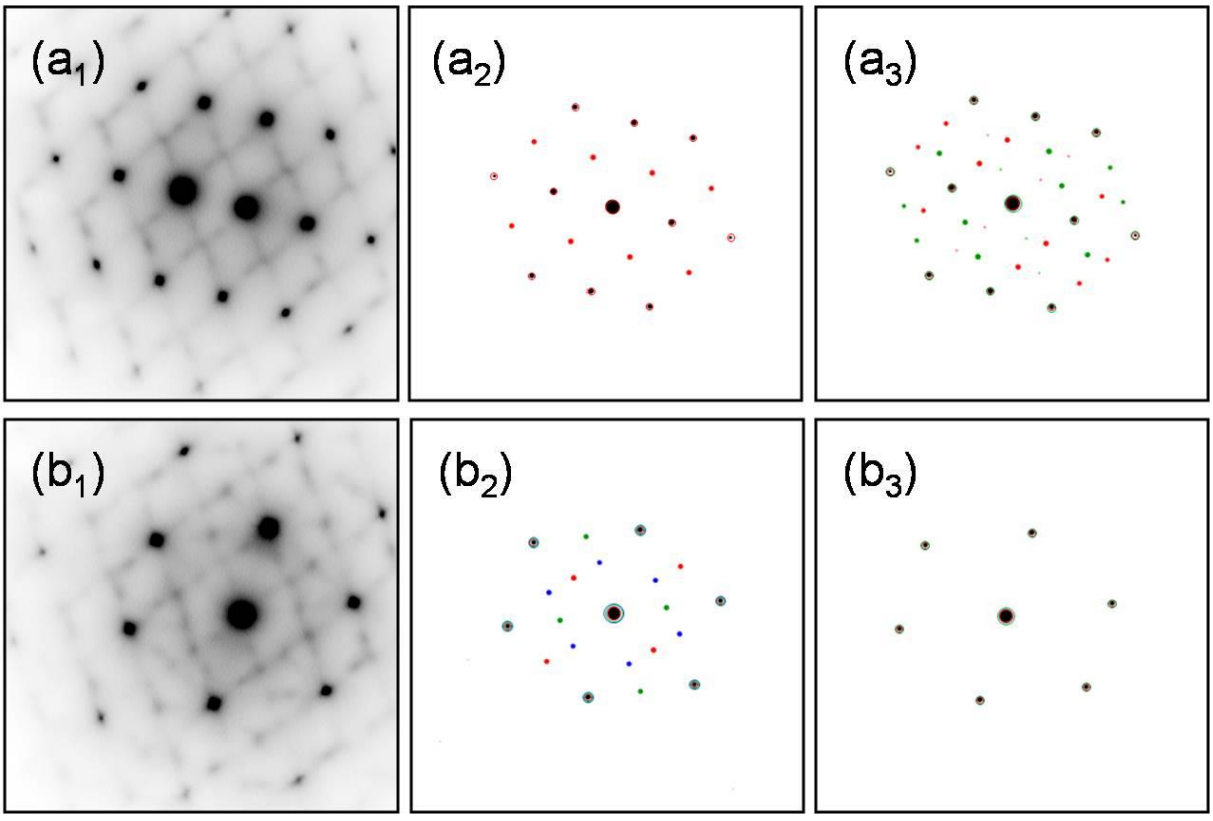

Fig. 3.9 Experimental and Simulated diffraction patterns: (a_1) and (b_1) experimental $[011]_\beta$ and [012] zone axis diffraction patterns taken from Fig. 3.6(a)(c), (a_2) and (b_2) simulated diffraction patterns of quasi-α from 6 different variants. (a_3) and (b_3) simulated diffraction patterns of quasi-ω from 4 different variants. For quasi-α and quasi-ω, the reflections from different variants are present with different colors.

The HRTEM examinations revealed that the quasi-α and the quasi-ω are in equiaxed shape. Each domain contains about several tens of atoms. They are distributed homogeneously within

the β matrix. Clearly they do not organize in the form of the striations as seen at lower magnification TEM micrographs (Fig. 3.2(c)). The striations should have some other origins.

3.3.4 Relation between the substructures and the striations

Through systematic examination of the SAED patterns acquired in the present work, we found two characteristics associated with the diffraction spots of the β phase. First some β diffraction spots are obviously elongated in certain reciprocal directions, forming the so-called relrods [134, 137]. The elongation is increased with the increasing order of the diffraction. This indicates that the elongation is rather from the scattering effect by crystal defects than by crystal size. Second the relrods exhibit characteristic extinction. This further confirms that the formation of the relrods is indeed from crystal defects. In the present alloy, the β diffraction spots are elongated in two families of reciprocal directions: <110> and <112> (hereafter <110> relrods and <112> relrods), as shown in Fig. 3.10. In the figures, the <110> relrods are displayed in red and the <112> relrods in green, and the geometrical relation between the two zone axes in the reciprocal space with the presence of the two kinds of relrods is also displayed. It is seen from Fig. 3.10 that the $[01\bar{1}]$ relrods (illustrated with the dashed red line) are absent in the $[011]_\beta$ zone axis pattern (Fig. 3.10(a)) but present in the $[100]_\beta$ zone axis pattern (Fig. 3.10(b)). It is well established that the atomic distortion on certain planes will result in the extension of the diffracted intensity in the direction normal to these planes [134, 137]. In the present case, the planes normal to the $[01\bar{1}]$ relrods are the $(01\bar{1})_\beta$ planes, as the structure is cubic. As analyzed above, the formation of quasi-α involves atomic displacements on $\{110\}_\beta$ planes and in $\langle 1\bar{1}0\rangle_\beta$ directions. The appearance of the $[01\bar{1}]$ relrods could be related to the formation of the quasi-α. If we denote the displacement vector $\boldsymbol{u}$, the absence of the $[01\bar{1}]$ relrods in the $[011]_\beta$ zone axis pattern corresponds to the situation $\boldsymbol{g}\cdot\boldsymbol{u}=0$, where $\boldsymbol{g}$ is the reciprocal vector of the diffraction spot. However in the $[100]_\beta$ zone axis pattern, this situation is not fulfilled, as summarized in Table 3.3. This indicates that the formation of the <110> relrods is indeed originated from the atomic displacements on the $\{110\}_\beta$ planes in the $\langle 1\bar{1}0\rangle_\beta$ to form the quasi α. Similarly, the formation of the <112> relrods is originated from the atomic

displacements to form the quasi ω.

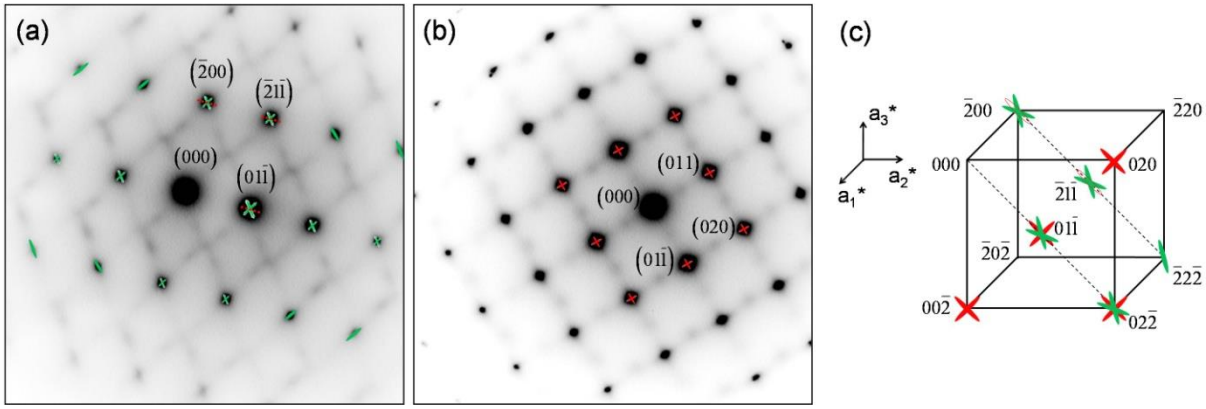

Fig. 3.10 Diffraction patterns of (a) $[011]_\beta$ and (b) $[100]_\beta$ zone axes. The <110> relrods are marked in red and the <112> relrods are marked in green. (c) Geometrical relation between the $[100]_\beta$ and the $[011]_\beta$ zone axis patterns in the reciprocal space.

Table 3.3 $\boldsymbol{g}\cdot\boldsymbol{u}$ for the $[011]_\beta$ and $[100]_\beta$ zone axis diffraction.

Zone axis	$[011]_\beta$			$[100]_\beta$		
g	$(\bar{2}00)$	$(\bar{2}1\bar{1})$	$(01\bar{1})$	(011)	$(01\bar{1})$	(020)
$\boldsymbol{u}$=[011] on the distorted plane $(01\bar{1})$	0	0	0	≠0	≠0	≠0

For a defected crystal, when the atoms are displaced from their lattice positions by a vector $\boldsymbol{u}$, a phase factor $\alpha=2\pi\,\boldsymbol{g}\cdot\boldsymbol{u}$ is introduced to the diffracted beam $\boldsymbol{g}$. Thus in the bright field image formed by excluding the diffracted wave $\boldsymbol{g}$ with an objective aperture, we obtain some dark regions arising from the enhanced diffraction by the strain field of the crystal defect [138]. The above extinction of the $[01\bar{1}]$ relrods in the [011] zone axis pattern was thus checked with the microstructure. The specimen was tilted to several positions. No specific contrast or striations appeared in the direction perpendicular to $\boldsymbol{g}_{(01\bar{1})}$, demonstrating $\boldsymbol{g}\cdot\boldsymbol{u}=0$ invisible character. This character indicates that the contrast of the striations is related to crystal defects. The oscillation of the contrast in microstructure suggests that the crystal defects possess planar feature, like stacking faults. Thus, the periodic contrast present on the exit site of the specimen is simply a representation of periodic extinction of the related distorted planes through the thickness of the specimen. With the known geometrical relations of the normal of the distorted planes, the

normal of the specimen surface, and the direction of the incident beam, the extinction distance of the distorted planes $\xi_g=\pi\Omega\cos\theta_{hkl}/(\lambda f(\theta_{hkl}))$ [138] can be calculated. In the equation, Ω is the volume of the unit cell, θ_{hkl} the Bragg angle, λ the electron wavelength and $f(\theta_{hkl})$ the atomic scattering amplitude [138]. Then the inter-striation spacing can be derived.

Table 3.4 Visibility of the distorted $\{110\}_\beta$ and $\{112\}_\beta$ planes under $(01\bar{1})_\beta$ reflection.

	$\{110\}_\beta$						$\{112\}_\beta$			
Distorted plane	$\pm(0\bar{1}1)$	$\pm(011)$	$\pm(101)$	$\pm(\bar{1}01)$	$\pm(110)$	$\pm(\bar{1}10)$	$\pm(112)$ $\pm(\bar{1}21)$ $\pm(2\bar{1}1)$ *	$\pm(\bar{1}12)$ $\pm(121)$ $\pm(21\bar{1})$ *	$\pm(1\bar{1}2)$ $\pm(12\bar{1})$ $\pm(211)$	$\pm(11\bar{2})$ $\pm(1\bar{2}1)$ $\pm(\bar{2}11)$
u	$\pm[011]$	$\pm[0\bar{1}1]$	$\pm[\bar{1}01]$	$\pm[101]$	$\pm[1\bar{1}0]$	$\pm[110]$	$\pm[11\bar{1}]$	$\pm[1\bar{1}1]$	$\pm[\bar{1}11]$	$\pm[111]$
$\boldsymbol{g}=(01\bar{1})$	inv	v	v	v	v	v	v	V	inv	inv

* The invisibility of these planes is due to their perpendicular positions to the specimen surface.

To simplify the analysis, we used a zone where the specimen surface is very close to the $(011)_\beta$ plane of the β phase (7.76° away from (011)). The microstructure is displayed in Fig. 3.2(d) and Fig. 3.2(e). The $(01\bar{1})_\beta$ is used as the operative reflecting plane. The spacing of the striations at the $(01\bar{1})_\beta$ extinction contour (where the two beam condition and the s_g=0 condition are approximately satisfied) is measured. It is about 30 nm. Under the two conditions, the formula of the extinction distance ξ_g has a particular simple form as given above. The visibility of the defected $\{110\}_\beta$ and $\{112\}_\beta$ planes under the $(01\bar{1})_\beta$ reflection is verified and the results are given in Table 3.4. The orientations of these planes with respect to the specimen surface are represented with the stereographic projection on the $(011)_\beta$ plane (the approximate specimen surface) and displayed in Fig. 3.11, where the visible planes are plotted in solid symbols. It is seen that two pairs of $\{110\}_\beta$ planes ($(1\bar{1}0)_\beta$ & $(\bar{1}0\bar{1})_\beta$ and $(\bar{1}01)_\beta$ & $(110)_\beta$) and two pairs of $\{112\}_\beta$ planes ($(1\bar{2}\bar{1})_\beta$ &$(\bar{1}\bar{1}\bar{2})_\beta$ and $(\bar{1}12)_\beta$ & $(121)_\beta$) are visible. The poles of the $(1\bar{1}0)_\beta$ & $(\bar{1}0\bar{1})_\beta$ and $(1\bar{2}\bar{1})_\beta$ & $(\bar{1}\bar{1}\bar{2})_\beta$ are located on the same diameter in the stereographic projection, as seen in Fig. 3.11, and thus these planes share approximately the

same orientation of the intersection with the specimen surface, as the surface is very close to the $(011)_\beta$ plane.

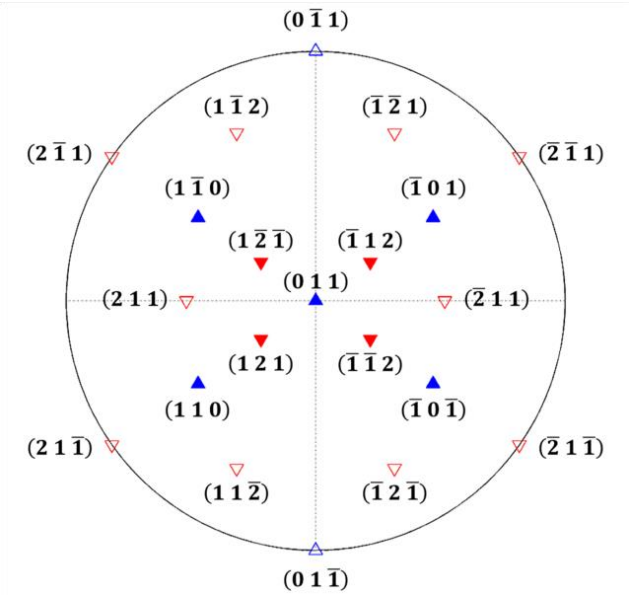

Fig. 3.11 Stereographic projections of the $\{110\}_\beta$ planes (in blue) and $\{112\}_\beta$ planes (in red) on the $(011)_\beta$ plane. The visible planes using the $(01\bar{1})_\beta$ reflection are expressed in solid symbols.

The situation is similar for the $(\bar{1}01)_\beta$ & $(110)_\beta$ and $(\bar{1}12)_\beta$ & $(121)_\beta$. The geometrical relations of the $(1\bar{1}0)_\beta$ and the $(1\bar{2}\bar{1})_\beta$ plane with respect to the incident beam are illustrated in Fig. 3.12. The spacing of the extinction fringes of the two planes on the exit site of the specimen is calculated. It is 17.5nm for the $(1\bar{1}0)_\beta$ plane and 34.2nm for the $(1\bar{2}\bar{1})_\beta$ plane. As the two sets of fringes are both projected on the TEM screen, the eventually observed fringes should be a mixture of the two and each can be treated as a set of Moiré fringes, as illustrated in Fig. 3.12. Thus the spacing and the orientation of the mixed fringes can be calculated according to the equations given in [138]. The calculated spacing of the mixed fringes is 35.5nm and the angle between the mixed fringes and the $(1\bar{1}0)_\beta$ fringes is 5.5°. The results are indicated in Fig. 3.12. The spacing is very close to the observed inter-striation spacing and the orientation of the calculated fringes is also very close to that of the observations. It confirms that the striations are indeed originated from the atomic displacements on the $\{110\}_\beta$ and $\{112\}_\beta$ planes to form the quasi structures. The fact that only one oriented striations are clearly observed in each striation zone indicates that the atomic displacements on the other

potential visible planes are not prevalent and the striations in these directions are less visible. They act as background noise to disturb the contrast homogeneity of the prevalent striations.

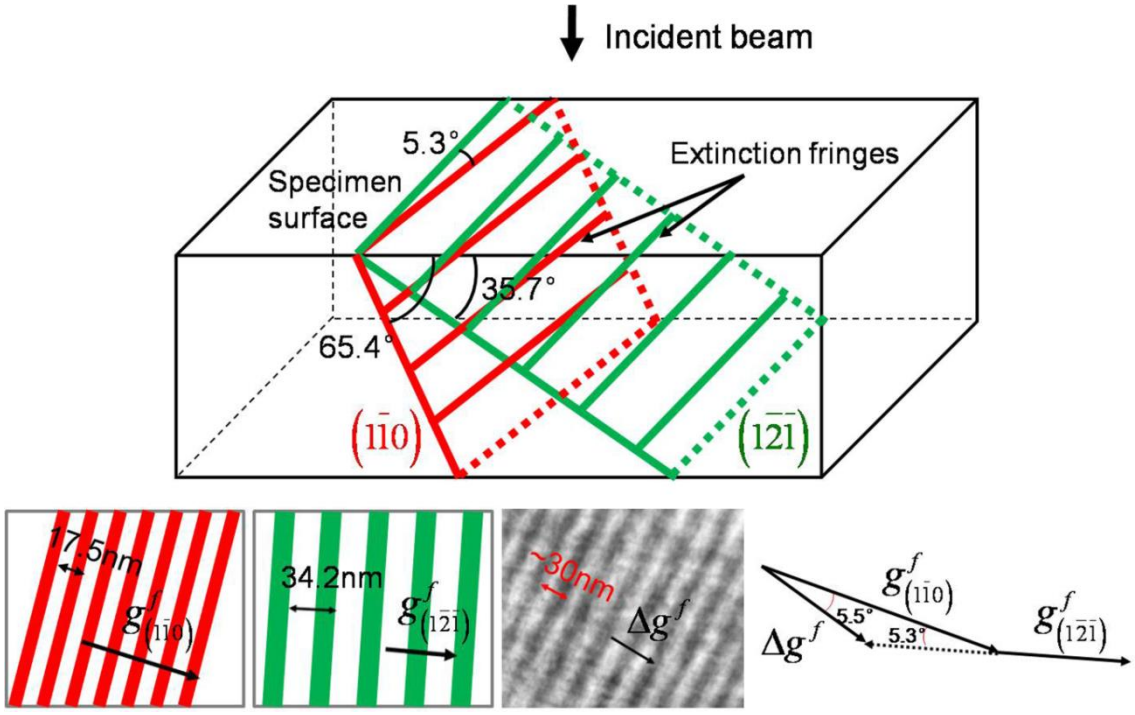

Fig. 3.12 Geometrical positions of the visible $(1\bar{1}0)_\beta$ and $(1\bar{2}\bar{1})_\beta$ planes in the foil with respect to the incident electron beam and the calculated inter-striation spacing and orientation of the two visible planes. In the figure, $\mathbf{g}^f$ is the reciprocal vector of a given set of fringes, i.e. it is perpendicular to the fringe direction and its modulus is the inverse of the inter-fringe spacing.

3.3.5 Relation between the two quasi structures and the phase transformation of β

To find out the relation between the $\{011\}_\beta$ and $\{112\}_\beta$ planar defects (that give rise to the striations in the TEM bright and dark field images and the additional spots in TEM SAED patterns) and the phase transformations of the β phase, the microstructures of the 800°C aged and the 350°C aged specimens were further examined. The two ageing temperatures are the characteristic α and ω formation temperatures for metastable β titanium alloys. In the 800°C aged specimen, α is formed and present as platelets in the microstructure, as shown in Fig. 3.13(a), whereas in the 350°C aged specimen, ω phase is formed and present as nano scaled particles, as shown in Fig. 3.13(c), the two being typical for the metastable β titanium alloys. Further crystallographic analyses showed that the α and the β phases possess the BOR with

$\{0001\}_\alpha \parallel \{110\}_\beta$; $\langle 11\bar{2}0\rangle_\alpha \parallel \langle 1\bar{1}0\rangle_\beta$ (Fig. 3.13(b)), whereas the β and the ω possess the Blackburn OR with $(0001)_\omega \parallel (\bar{1}11)_\beta$; $[\bar{1}2\bar{1}0]_\omega \parallel [110]_\beta$ (Fig. 3.13(d)). The two ORs are also typical for the two transformations in metastable β titanium alloys.

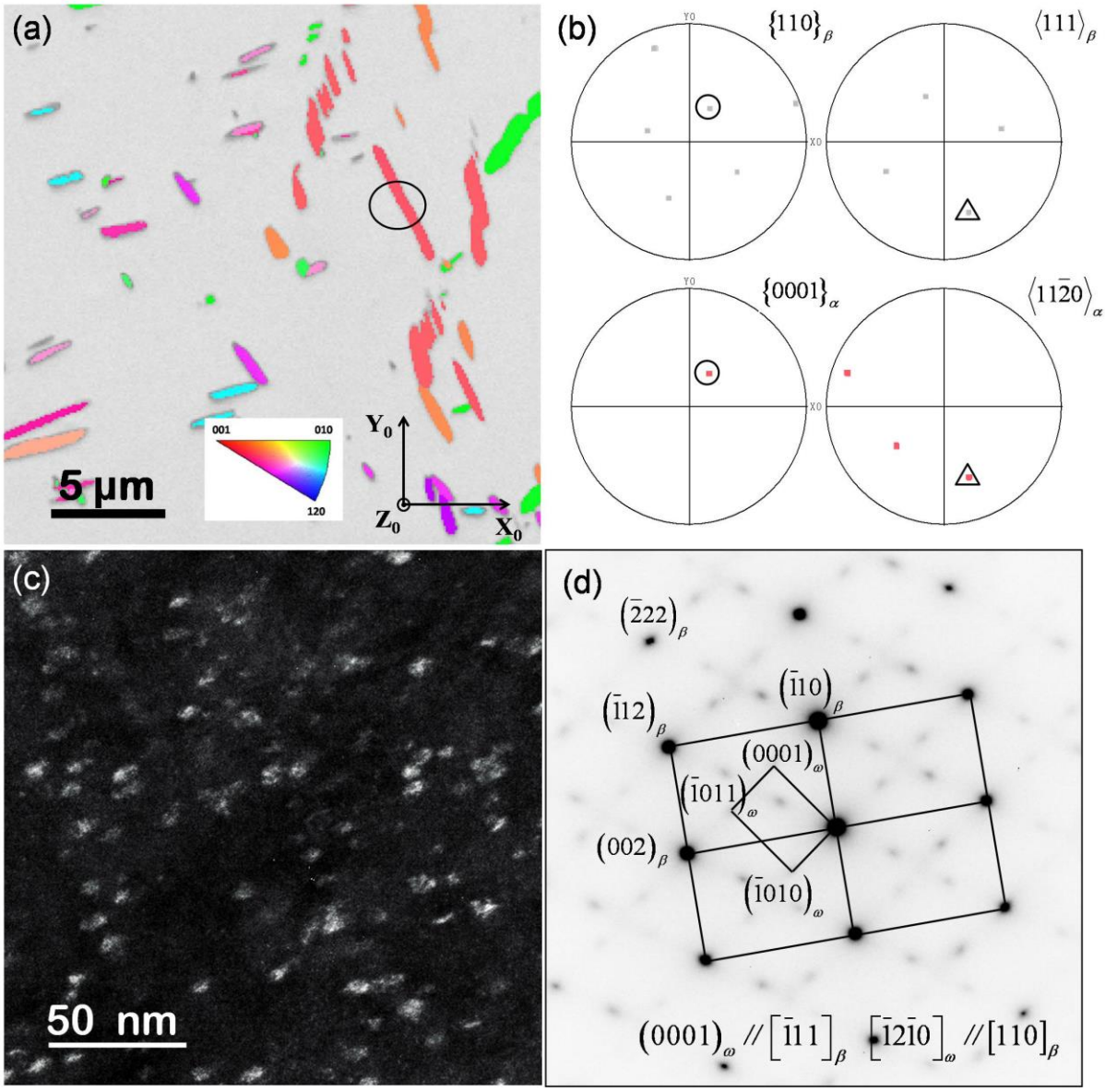

Fig. 3.13 (a) SEM/EBSD micrograph of Ti-5553 aged at 800°C for 30 min followed by water quenching and (b) the corresponding $\{110\}_\beta$, & $\langle 111\rangle_\beta$; $\{0001\}_\alpha$ & $\langle 11\bar{2}0\rangle_\alpha$ pole figures of the α and the β enclosed in the black circle in (a). The related planes and direction defining the BOR in the pole figures are outlined with the black circles and the black triangles, respectively. (c) TEM dark field micrograph of Ti-5553 aged at 350°C for 120 min and (d) the corresponding $[110]_\beta/[\bar{1}2\bar{1}0]_\omega$ zone axis SAED pattern. The dark field image was produced from the $(\bar{1}010)_\omega$ reflection of the ω phase.

With the two identified ORs, the atomic correspondences between the parent β and the product α and ω can be readily established, as shown in Fig. 3.14, where the two quasi structures are given between the parent and the product structures for each transformation. The characteristics of each defect structure demonstrate that they are exactly the structure between the initial and the transformed structures of the corresponding transformation. Detailed one to one atomic correspondence analysis showed that for the β to α transformation, the structure change from the parent cubic (BCC) to the hexagonal structure (HCP) of α is realized first by displacing each second $\{110\}_\beta$ planes (outlined in red in Fig. 3.14(a)) in $\langle 1\bar{1}0\rangle_\beta$ direction with an amount of $\frac{a}{6}\langle 1\bar{1}0\rangle_\beta$ and then a coordinated movements of all atoms to reach the atomic positions in the hexagonal structure of α. In such a sequence, the structure produced by the $\frac{a}{6}\langle 1\bar{1}0\rangle_\beta/\{110\}_\beta$ displacement can be regarded as the precursor for the β to α transformation. Similarly, the detailed one to one atomic correspondence analysis demonstrated that for the β to ω transformation, the structure transition is realized first by the displacement of the second and the third $\{211\}_\beta$ planes (outlined in respective red and black in Fig. 3.14(b)) in the opposite $\langle\bar{1}11\rangle_\beta$ directions with an amount of about $\frac{a}{12}\langle\bar{1}11\rangle_\beta$ and then by a coordinated movement of all atoms to reach the atomic positions in the hexagonal structure of ω. Similar to the case of the β to α transformation, the structure produced by the $\pm\frac{a}{12}\langle\bar{1}11\rangle_\beta/\{211\}_\beta$ displacements is the precursor for the β to ω transformation. As α and ω are the thermodynamically stable and metastable phases at temperatures lower than T_β, the formation of the two quasi structures is toward the formation of these phases, hence the existence of the two structures is energetically favorable.

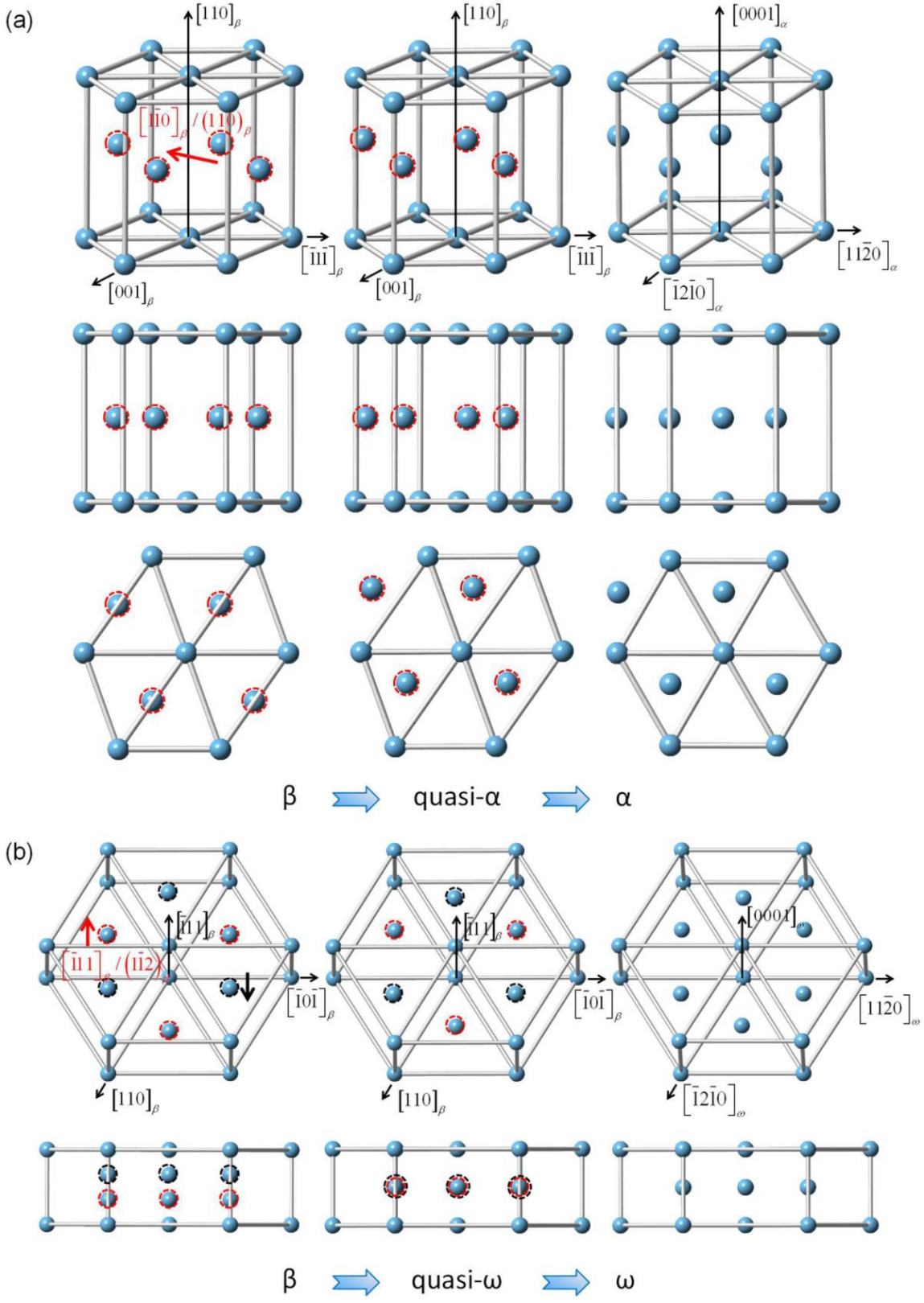

Fig. 3.14 Atomic correspondences between the parent β and the products (a) α with quasi-α as an intermediate structure and the corresponding cells viewed in the $[\bar{1}12]_\beta$ and the $[\bar{1}\bar{1}0]_\beta$ directions, and (b) ω with quasi-ω as an intermediate structure and the corresponding cells viewed in the $[\bar{1}\bar{2}1]_\beta$ direction.

3.4 Summary

In the present work, the striations and the diffraction characteristics of the β phase of a metastable titanium alloy were thoroughly investigated. The results clearly demonstrate that the structure of the β phase in the metastable titanium alloy is not "purely" body centered cubic. Large amount of planar defects are formed with a structure between that of the parent β phase and that of the α or the ω phase, demonstrating pre-phase transformation tendency. These structures are formed by atomic displacements on $\{110\}_\beta$ plane in $\langle 1\bar{1}0\rangle_\beta$ direction for the quasi-α and atomic displacements on $\{112\}_\beta$ plane in $\langle 11\bar{1}\rangle_\beta$ direction for the quasi-ω. Due to these atomic displacements, the $\{110\}_\beta$ and $\{112\}_\beta$ planes become distorted, giving rise to the additional diffraction spots at the 1/2, the 1/3 and 2/3 diffraction positions of the β phase, the streaking of the β diffraction spots and the formation of extinction fringes in the TEM bright and dark field images. Different from the diffraction contrast induced by perfect stacking fault, the contrast of the striations is diffuse and not homogeneous, because the distorted regions on the corresponding planes are very small at atomic scale. In the microscopic scale, the striations are distributed homogenously. This infers that the pre-phase transformation in β phase occurs very homogeneously and globally. The results of the present work provide new information on the structural nature of the β phase in metastable β titanium alloys and elucidate the origins of the commonly observed striations.

Chapter 4 Microstructure and crystallography of α phase during high temperature thermo-mechanical treatments

4.1 Introduction

During hot compression below the β transus temperature (T_β), several physical mechanisms may occur simultaneously as the plastic deformation, the β→α phase transformation and softening such as dynamic recovery (DRV) or recrystallization (DRX) of the β phase [12, 19, 91, 139]. These mechanisms may influence the α phase nucleation [52], the orientation relationship [96, 140, 141, 142], as well as the kinetics of phase transformation [52, 143, 144]. However, these dynamic characteristics during hot compression of metastable β titanium alloy have not been fully assessed and exploited.

In this chapter, the microstructural evolution during the high temperature (800℃) coupled thermo-mechanical treatments of Ti-5553 alloy with a single β initial microstructure was studied in detail. The α precipitation mechanism, orientation relationship between α/β, substructures formed during deformation as well as the effect of deformation on phase transformation behavior were examined and discussed in this work. The results of the present work are expected to provide valuable reference for process optimization and the microstructural evolution control.

4.2 Experimental

Compression was applied isothermally at 800°C using a Gleeble-3500 thermo-mechanical simulator (Fig. 2.4 (a) in ***Chapter 2***). The hot compression was performed at two different strain rates to two different strains. The detailed deformation parameters are given in Table 4.1. Prior to each compression, the specimens were heated to the isothermal temperatures at a rate of 25°C/s and then held for 10s at 800°C before the commencement of the deformation to ensure a

homogeneous temperature field. After compression, all specimens were immediately cooled in water in order to retain the deformed microstructures. As references, the same numbers of specimens with the same initial microstructure were heat treated at 800°C, respectively, under the same thermal conditions as those of the hot compressions.

Table 4.1 Detailed hot compression parameters.

Temperature (°C)	Strain rate (s^{-1})	Strain	Corresponding isothermal holding time (min)	Cooling
800	0.0005	0.7	23	Water quenching
	0.0005	1.2	40	
	0.001	1.2	11.5	

4.3 Results

4.3.1 Initial microstructure

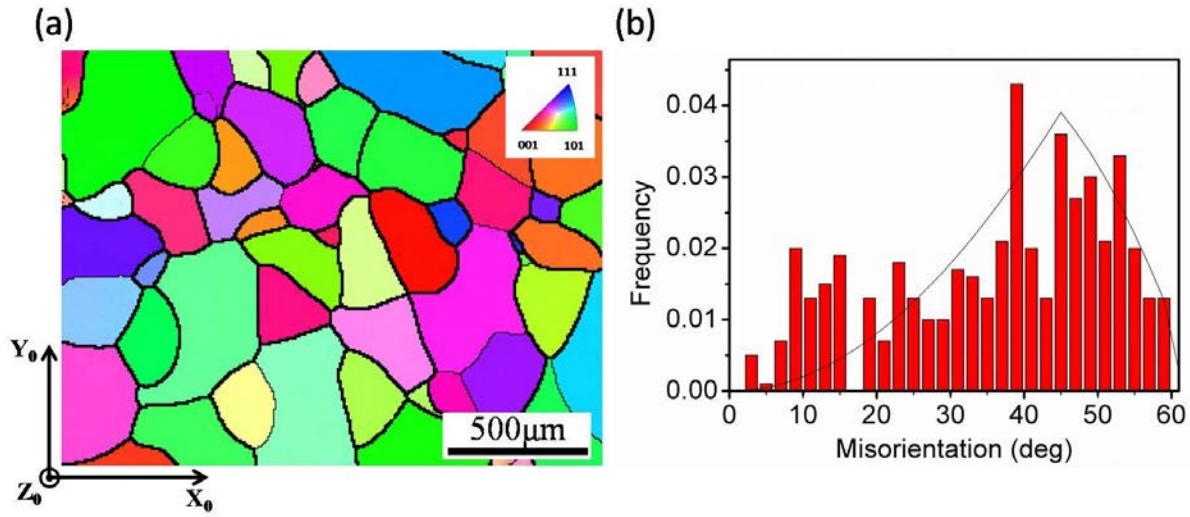

Fig. 4.1 (a) EBSD map of the single β phased microstructure of Ti-5553 after solution treatment. The grains are colored according to the projection of the direction Y_0 in the Inverse Pole Figure (IPF/Y_0) as shown in the legend. The bold black lines outline the high angle grain boundaries (>10°, HAGBs) and the fine black lines represent the low angle grain boundaries (2-10°, LAGBs). (b) Histogram of correlated disorientation angle distribution of the as-solution treated β phase (minimum angle is 2°, bin width is 2°). For comparison, the theoretical disorientation angle distribution of an isotropic polycrystal is given in line profile (MacKenzie distribution).

As mentioned in ***Chapter 3***, the initial microstructures for the subsequent heat treatments and hot compression were obtained by solution treatment at 900°C for 30 min followed by water quenching. The microstructure displayed in Fig. 4.1(a) is composed of single β equiaxed grains with an average size of ~300μm. The corresponding correlated disorientation angle distribution histogram (Fig. 4.1(b)) is close to that of randomly oriented polycrystals (the line profile), suggesting that the alloy is not textured. The non smooth feature of the histogram is due to a statistical effect.

4.3.2 Microstructural evolution characteristics

4.3.2.1 Morphology and transformation rate

Each column of Fig. 4.2 represents the optical micrographs of the microstructures obtained for the same holding time at 800°C either through heat treatments (Fig.4.2(a_1-c_2)) or hot compressions (Fig.4.2(a_3-c_4)). Each microstructure is represented at two different magnifications. It is seen that for the heat treated samples, the α phase forms mainly along β grain boundaries (GB) and also inside the β grains. The grain boundary α (α_{GB}) are more or less continuous along the grain boundaries, whereas the intragranular α (α_I) precipitates have a short plate shape. With increasing aging time (from 20 min to 40 min), the amount of both kinds of α precipitates increases. The α_{GB} precipitates become more continuous, and the α_I increase both in size and number (Fig. 4.2(a_2-c_2)). Moreover, with the prolongation of the aging time, some parallel α lamellae start to precipitate from grain boundary towards grain interior, forming the so-called Widmanstätten α, α_{WGB} (Fig. 4.2(b_2)). All these characters are typical of the β to α transformation in Ti-5553 alloy and of some other Ti alloys. Additionally, one can find that in all the heat treated samples, precipitate free zones (PFZs) are present on either side of β grain boundaries with a thickness of about 40μm (Fig. 4.2(a_1-c_2)), suggesting that the formation of α precipitates is diffusional. The corresponding chemical analyses are given in ***Section 4.3.2.2***.

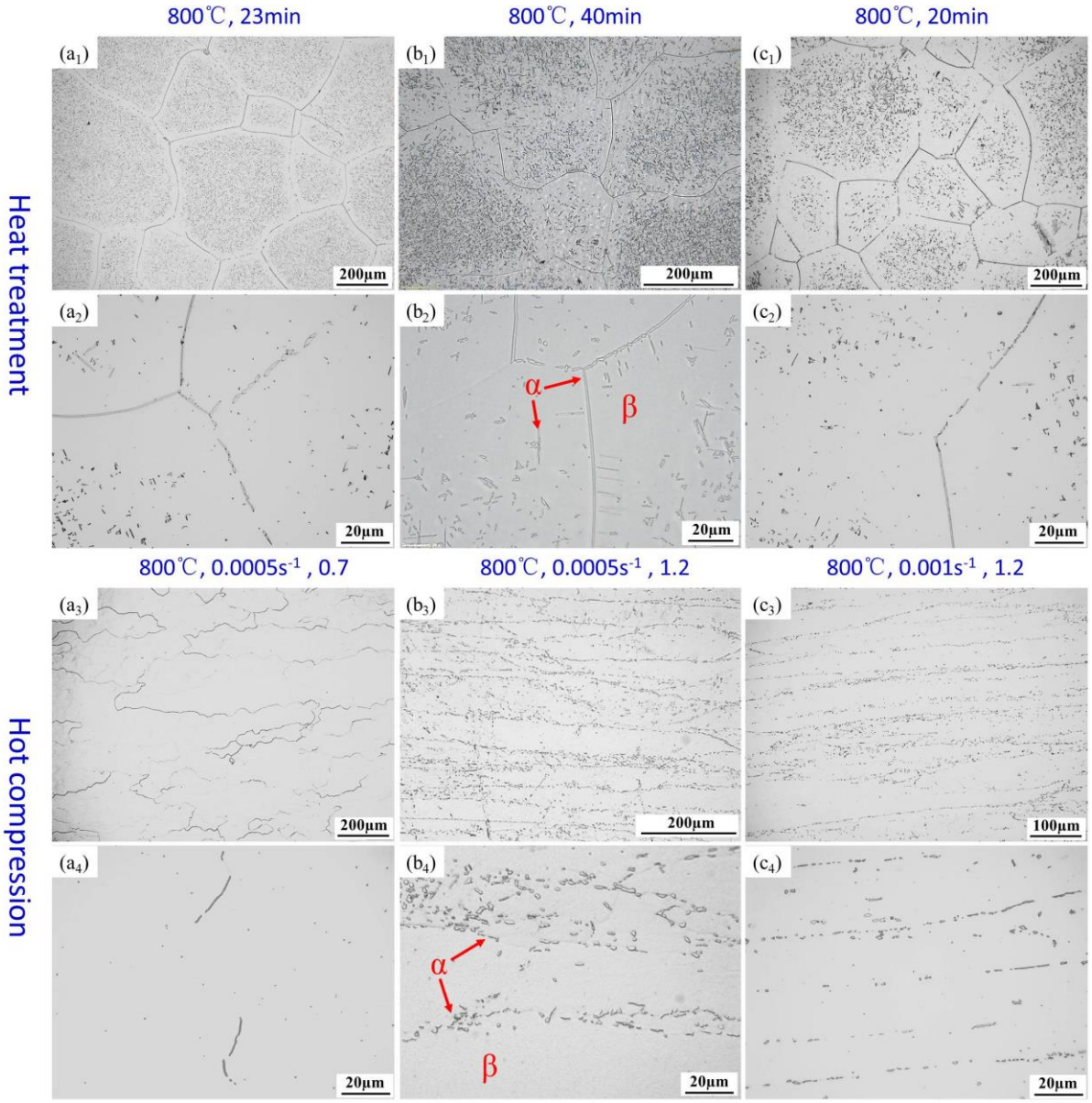

Fig. 4.2 Optical micrographs

Processing mode	No.	(a)	(b)	(c)
Heat treatment	1 2	800°C, 23min	800°C, 40min	800°C, 20min
Hot compression	3 4	Strain of 0.7 at 800°C, $0.0005s^{-1}$	Strain of 1.2 at 800°C, $0.0005s^{-1}$	Strain of 1.2 at 800°C, $0.001s^{-1}$

When different compression parameters were applied, the resultant microstructures change drastically. The chosen reference treatment was performed with a strain of 1.2 and a

strain rate of $0.0005s^{-1}$ (Fig. 4.2(b_3)(b_4)). Comparison at iso-strain and iso-strain rate can be made with the treatment presented in Fig. 4.2(a_3)(a_4) and Fig. 4.2(c_3)(c_4) respectively.

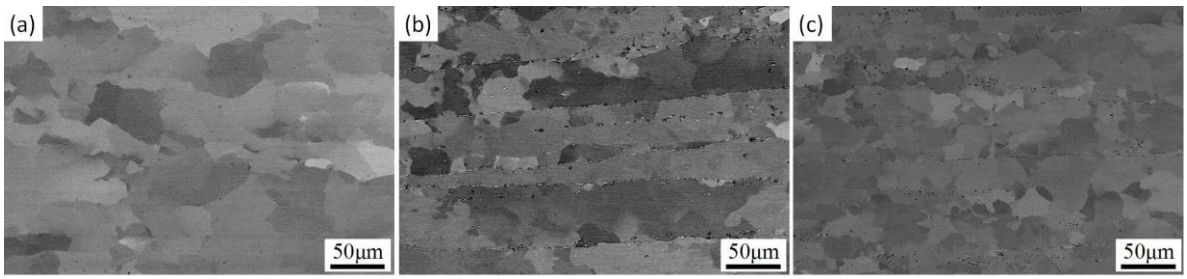

Fig. 4.3 SEM back scattered electron (BSE) micrographs of Ti-5553 samples hot compressed at 800°C to a strain of (a) 0.7 under a strain rate of $0.0005s^{-1}$, (b) 1.2 under a strain rate of $0.0005s^{-1}$ and (c) 1.2 under a strain rate of $0.001s^{-1}$.

For the first case, the deformation rate is constant ($0.0005s^{-1}$) but the deformation strain changes from 0.7 to 1.2. A comparison between Fig. 4.2(a_3)(a_4) with Fig. 4.2(b_3)(b_4) shows that the β grain boundaries are no longer straight. Simultaneously, the β grains are no longer equiaxed but became elongated in the direction perpendicular to the compression axis (vertical direction in the figures). The aspect ratio of the grains increases with increasing strain, as shown by the SEM backscattered electron (BSE) micrographs in Fig. 4.3. In this figure, the contrast is mostly due to the difference in crystallographic orientation and thus can be utilized to identify grains and subgrains. These indicated that DRV and DRX happened with the deformation by comparing the Fig 4.1-3 [12, 91, 145]. It is seen that at small deformation strain (0.7), the elongation of the β grains is accompanied by grain fragmentation, forming subgrains (Fig. 4.3(a)) which is typical of DRV. With the strain increasing to 1.2, banded structures with their longer axis perpendicular to the compression axis formed. Within each band, sub domains with different sizes and shape can be clearly seen (Fig. 4.3(b)). The widths of the bands are around 40μm which is of the same order of magnitude as the PFZs on either side of the β grain boundaries in the heat treated specimens. Together with the morphology change of the β grains, the β→α phase transformation occurred. First, unlike in the undeformed specimens, a large majority of the precipitates are located along β boundaries (LAGBs and HAGBs) but seldom in β grain interiors. Then, the morphology differs from those in the corresponding heat treated specimens. Some α_{GB} are still partial continuous in deformed

specimen with small strain (Fig. 4.2 (a_3)(a_4)), but equiaxed or rod shaped α, 1~2μm in length, formed in the large strain specimen (Fig. 4.2 (b_3)(b_4)). Such a microstructure is often referred as "necklace" microstructure [146]. With increasing of strain, the isothermal holding time also increases. As consequence, the α precipitates are more numerous but remains discontinuous.

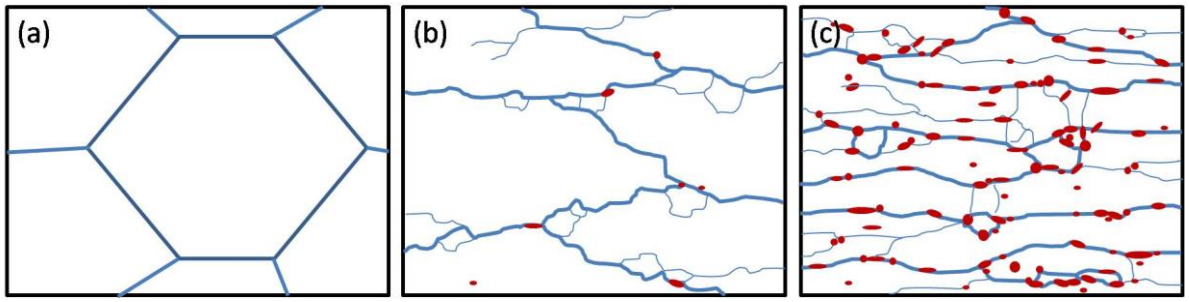

Fig. 4.4 Illustration of the microstructural evolution of Ti-5553 alloy during the hot compression at 800℃. (a) Initial microstructure composed of single β equiaxed grains, (b) β grain fragmentation through deformation and DRV/DRX and commencement of α precipitation at β boundaries, and (c) formation of band shaped β grains with particle shaped α (in red) along β boundaries.

For the second case, the deformation strain (1.2) is constant but the strain rate changes from $0.0005s^{-1}$ to $0.001s^{-1}$, the microstructural features of the two phases remain not much changed. The β grains are elongated in the direction perpendicular to the compression axis, forming the band structure, as seen in Fig. 4.3(c), and the α phase is in equiaxed or short bar shape distributed along β band boundaries, as shown in Fig. 4.2(c_3)(c_4). At higher strain rate, the α particles (~1μm) are smaller and the amount is lower. This is related to the shorter isothermal holding time and thus a shorter available time for the formation and the growth of the α phase. For the β matrix, as seen in Fig. 4.3(c), grains are largely refined as the case under slow deformation rate (Fig. 4.3(b)), indicating that DRV/DRX occurred with the deformation. However, the band characteristic (Fig. 4.3(c)) is less pronounced compared with that obtained at lower strain rate (Fig. 4.3(b)). This is because the amount of α phase is less, hence its decoration effect on microstructure and its pinning effect on β grain boundaries are reduced. It should also be noted that DRV/DRX happened before the β to α phase transformation, as seen from Fig. 4.2(a_3) and Fig. 4.3(a) where the phase transformation just started but DRV/DRX is well advanced. This indicates the energy barrier to DRV/DRX is smaller than that to phase transformation. For convenience, the microstructural evolution induced by deformation,

DRV/DRX and phase transformation of the present alloy during hot deformation at 800°C is summarized in Fig. 4.4.

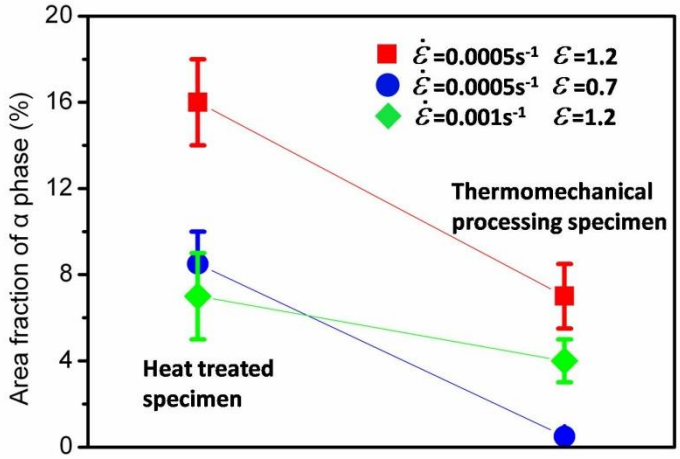

Fig. 4.5 Area fractions of α phase in the hot compressed and the corresponding heat treated specimens.

The influence of the deformation on the phase transformation process is further studied. The amount of α precipitates are quantified in the hot compressed samples and in their heat treated counterparts. The results are shown in Fig. 4.5. It is seen that, in general, the amount of α precipitates in the deformed samples is less than that obtained under heat treatment, indicating that the deformation retards the β→α phase transformation. The area fractions of the α phase in the specimens heat treated at 800°C for 23 min and that hot compressed under the same thermal conditions but with a strain of 0.7 under the strain rate of 0.0005s^{-1} are ~8.5% and ~0.5%, respectively. When the strain was increased to 1.2, the corresponding area fractions of the heat treated and the hot compressed specimens are ~16% and ~7%, as indicated by the blue and red lines in Fig. 4.5. For these two lines the slopes are almost the same, indicating that the retardation degree of the deformation under the same strain rate is similar. However, when the deformation rate increases to 0.001s^{-1}, the areas fraction of the α phase in the hot compressed specimen and that in the corresponding heat treated specimen are ~4% and ~7%, respectively, as shown by the green line in Fig. 4.5. Comparing the absolute value of the slope of the green line with those of the blue and the red line, one can found that the slope of the green line is obviously smaller. This indicates that retardation impact of deformation on phase transformation with higher strain rate is lower. Coincidently, the reduced retardation

effect of the deformation on phase transformation under higher strain rate corresponds to the reduced degree of DRV/DRX of the β phase, as revealed above. It seems that the β to α phase transformation is in competition with the DRV/DRX of the β phase under deformation. When DRV/DRX occur intensively, the phase transformation is retarded.

4.3.2.2 Chemical composition distribution characteristics

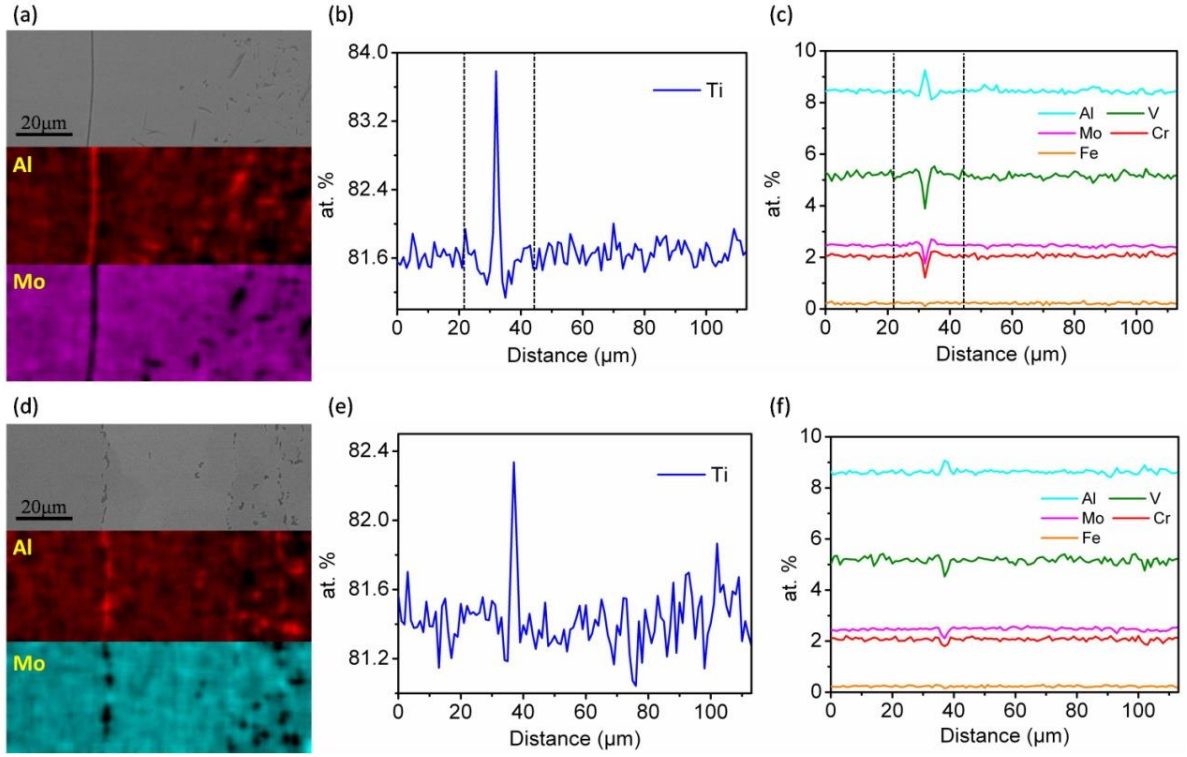

Fig. 4.6 SEM/EDX Al and Mo composition maps, as well as the corresponding SE images of the specimens (a) heated treated at 800°C for 40 min and (d) hot compressed at 800°C to a strain of 1.2 at a strain rate of $0.0005s^{-1}$ and the corresponding line profile of Ti, and the alloying elements Al, Mo, V, Cr and Fe in (b) and (c) the heat treated, and (e) and (f) the hot compressed specimens integrated along the direction parallel to the boundary (vertical in (a) and (d).

Fig. 4.6 shows the distribution and evolution of the alloying elements (Ti, Al, Mo, V, Cr and Fe) by SEM/EDX analyses. Obviously, in the α phase the representative α and β stabilizing elements, Al and Mo, are enriched and depleted, respectively (Fig. 4.6(a) and (d)) in both heat treated and hot compressed specimens, confirming that the phase transformation is diffusional and deformation did not change it. For the heat treated specimen, Ti and Al are depleted in the zones 10μm in width adjacent to the β boundaries, as indicated with the dotted

lines in Fig. 4.6(b) and (c). In contrast, the β stabilizing elements (Mo, V, Cr and Fe) are enriched in these areas. These distribution features lead to the formation of PFZs on both sites of β grain boundaries. For the hot compressed specimen, quantitative analysis of the α precipitates shown in Table 4.2 demonstrates that the enrichment of the α stabilizing element and the depletion of the β phase stabilizing elements in the α phase is more pronounced. This may be attributed to the existence of large amount of crystal defects produced by deformation. The abundant defects, such as dislocations and subgrain boundaries, could provide favorable diffusion paths and enhance the repartition of the alloying elements required by phase transformation.

Table 4.2 Chemical composition of α phase in heat treatment and hot compressed specimens (at. %).

Alloy elements	Nominal composition	Heat treated		Hot compressed
		α_{GB}	α_{I}	α_{GB}
Titanium	80.94	82.75	83.46	86.92
Chromium	2.52	1.42	1.33	0.13
Molybdenum	2.46	2.13	1.70	0.30
Iron	0.36	0.11	0.01	0
Vanadium	4.46	3.89	3.73	1.65
Aluminium	9.26	9.70	9.78	11.00

4.3.2.3 Orientation relationship between α and β and their crystallographic features

Crystallographic analyses show that for the heat treated specimens, the αphase and the β phase respect the Burgers orientation relationship (BOR). As shown in Fig. 4.7(a) and (b), both the α_I and α_{GB} demonstrate good agreement with the BOR. The deviations are smaller than 4°. The peak at 13° comes from the α_{GB}, the respect the BOR with one grain but have more deviation with the other one. The relation with the other grain is not completely random. Indeed, in special geometric cases, a α_{GB} can respect the BOR with both β grains. In cases where the geometrical conditions are approximately met, there is a tendency to minimize the BOR with respect the second β grain also [47]. This explains why the misorientation angle is small with

respect to the random distribution plot with the continuous line.

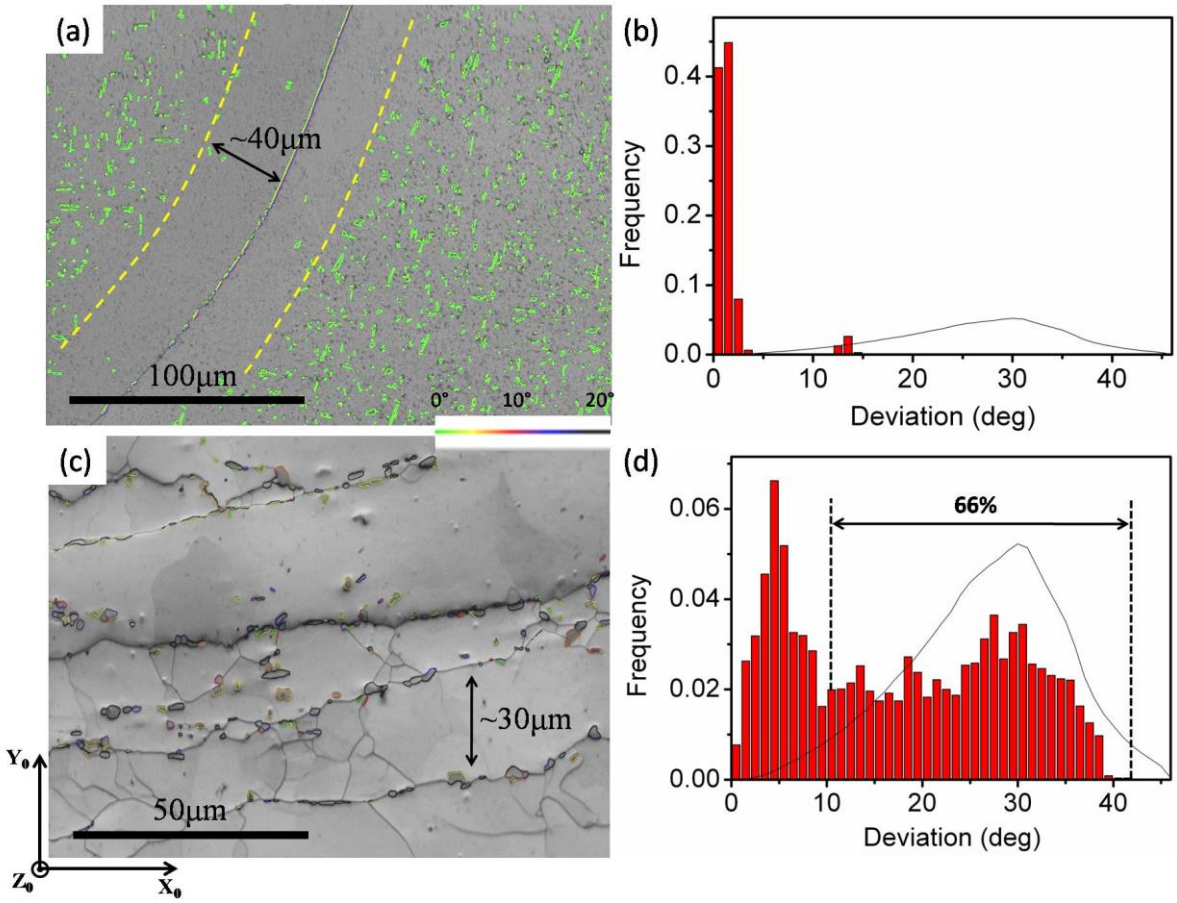

Fig. 4.7 EBSD Band contrast micrograph of Ti-5553 (a) heat treated at 800°C for 40 min and (c) hot compressed at 800°C to a strain of 1.2 under a strain rate of $0.0005s^{-1}$, and (b) and (d) the corresponding statistical histograms of angular deviation from the BOR between α and β in the two specimens. The colored contour lines around α indicate the angular deviations with respect to the exact BOR. The deviations higher than 20° are shown in black. For comparison, the deviation to the BOR of a randomly oriented precipitatesis given in line profile. The yellow lines in (a) delimitate the PFZs on both sides of the boundary β. The widths of the PFZs in (a) and the band spacing in (b) are indicated.

When hot compression was performed, the situation changed. As shown in Fig. 4.7(c) and (d), most of the α particles are deviated from the BOR. About 66% of the α phase have a deviation larger than 10° (regarded as a large deviation form BOR) and the maximum deviation reaches 42° (Fig. 4.7(d)). From the EBSD band contrast images of the microstructures obtained by the heat treatment and the hot compression in Fig. 4.7(a) and (c), the width of the PFZs is in comparable dimension as the width of bands in the latter.

Examinations also show that thedeviation from the BOR is strain and strain rate dependent. As shown in Table 4.3, with the increase of the deformation strain under a constant strain rate both the maximum deviation angle and the amount of α having a deviation higher than 10° are increased. When the strain rate is increased to a fixed deformation strain, the amount of α with more than 10° deviation decreases, from 66% to 51%. Usually for plastic deformation at high temperature, there are two mechanisms of the deformed alloy to accommodate the macroscopic strain. One is dislocation slip and the other is grain boundary sliding. The latter contribution increases with the decrease of deformation rate and hence more boundary α losses their OR with the adjacent β grains. As the α phase is known to respect the BOR when it precipitates, it indicates that the OR is gradually destroyed during the subsequent deformation due to grain boundary sliding and dislocation ship in the area around the α particles leading to rotation of the crystalline lattices. This has been further confirmed by the subsequent examinations where the deviations of the α_I and the α_{GB} are analyzed separately. The results shown in Fig.4.8 clearly demonstrate that the deviation mainly happens to α_{GB} phase (Fig. 4.8(a)) and the amount of α with large deviation (>10°) decreases with the increase of the deformation strain rate (Fig. 4.8(b)). Moreover, there are other two reasons that explain the difference between α_I and the α_{GB}. The one is precipitation occur first at grain boundaries, the first precipitate have more time to undergo the subsequent deformation; the other one is there is already one side of the GB which is not in BOR with the precipitate as it forms.

Table 4.3 Deviation from BOR under different deformation parameters.

Deviation from BOR	Variations of deformation parameters			
	Strain rate of $0.0005s^{-1}$		Strain rate of 1.2	
	0.7	1.2	$0.001s^{-1}$	$0.0005s^{-1}$
Fraction >10 (%)	26	66	51	66

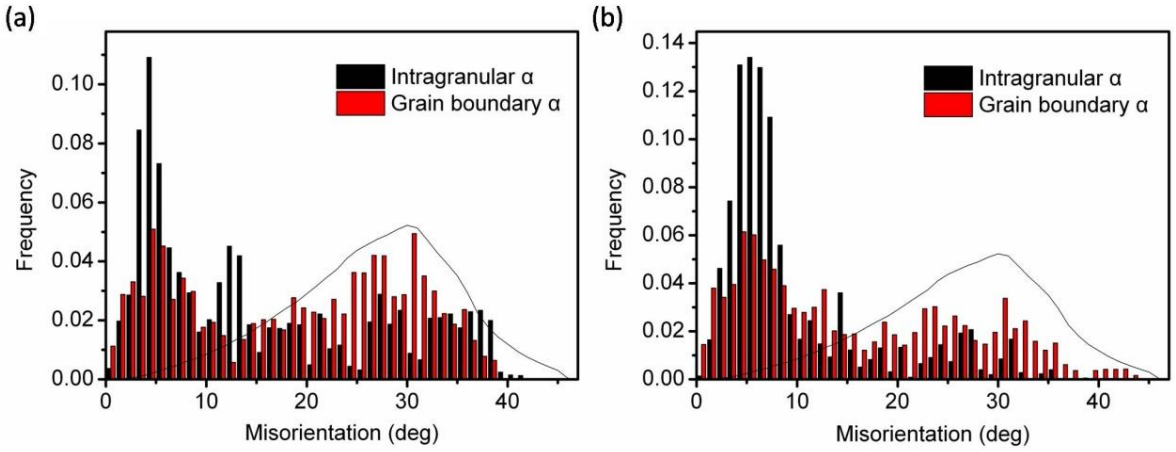

Fig. 4.8 Statistical histogram of the angular deviation of α_I and the α_{GB} from the exact BOR in the Ti-5553 compressed at 800°C to a strain of 1.2 under strain rates of (a) $0.0005s^{-1}$ and (b) $0.001s^{-1}$, respectively.

Accompanying the loss of the BOR in the progress of the deformation, the morphology and the crystallographic orientation of the α_{GB} changes from the continuous form with single orientation (Fig. 4.9(a)) to particles each having a different crystallographic orientation Fig. 4.9(b). For example those in the white dotted box in Fig. 4.9(b), these α grains are in different colors in the magnifying IPF map and have own different $\{0001\}_\alpha$ plane shown in the $\{0001\}_\alpha$ pole figure (Fig. 4.9(c)). The adjacent particles along the β grain boundary are neither in BOR nor twin related. Thus, hot deformation not only changed the nucleation site of α phase, but also destroyed the OR. As aforementioned in ***Section 4.3.2.1***, due to the increased atomic mobility at high temperature, softening processes, such as DRV and DRX would occur during high temperature deformation. Fig. 4.9(d) is the phase-grain boundary map of of the hot compressed microstructure at 800°C to a strain of 1.2 under a strain rate of $0.0005s^{-1}$, abundant LAGBs/subgrain boundaries formed by the dislocations rearrangement during the hot compression accompanied by a small quantity of DRV [87].That agrees with that it is generally accepted that the predominating softening mechanism of the β phase is DRV in metastable β titanium alloys [11]. Moreover, the DRX could be identified as typical continuous dynamic recrystallization (CDRX), which involves a transformation of low angle boundaries into high angle boundaries of the subgrains [89, 90, 91]. Due to this instability during continuous deformation, the nucleated α cannot grow smoothly to form continuous precipitates.

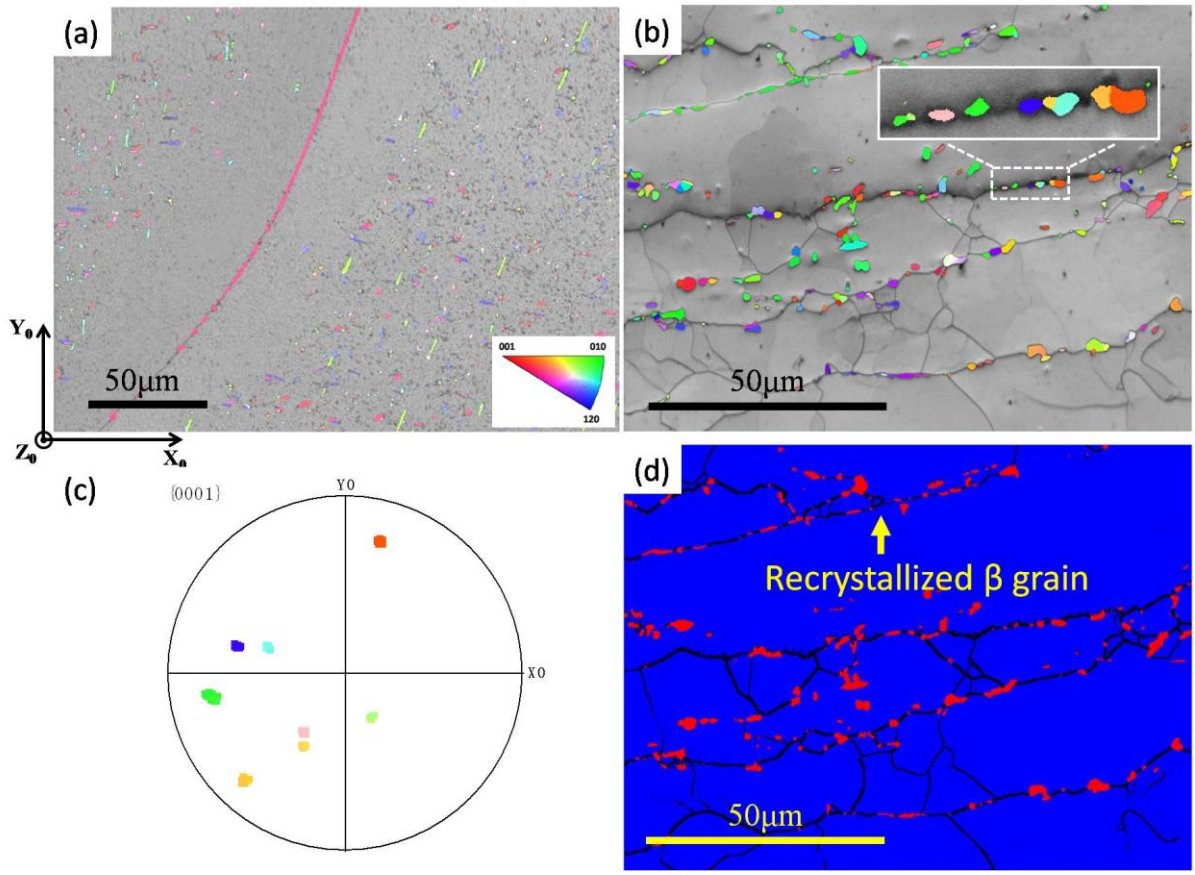

Fig. 4.9 EBSD micrographs of Ti-5553 (a) heat treated at 800°C for 40 min, (b) hot compressed at 800°C to a strain of 1.2 under a strain rate of $0.0005s^{-1}$, and (c) the $\{0001\}_{\alpha}$ pole figure of the α phase marked with whitedotted box in Fig. 4.9(b). In the figures, the β phase is represented by the EBSD band contrast and the α phase is by the Y_0 axis inverse pole figure (IPF) micrograph. (d) The phase-grain boundary EBSD map of the hot compressed microstructure at 800°C to a strain of 1.2 under a strain rate of $0.0005s^{-1}$. The bold black lines outline high angle boundaries (>10°) and the fine black lines low angle boundaries (2-10°).

4.3.3 Substructures of hot compressed β matrix

TEM examinations revealed that the β matrix possesses deformed and DRV/DRX substructures. As shown in Fig. 4.10(a), many β grains are composed of bands characterized by large amount of parallel dislocation arrays, demonstrating the mixed feature of deformation and polygonalization. The large quantities of dislocations were induced by deformation; whereas their regular arrangement should results from polygonalization. In some other areas, DRV/DRX is in progress. Equiaxed grains of several micrometers in size are formed, as shown in Fig. 4.10(b), indicating the occurrence of DRV/DRX. Thus dynamic hardening and dynamic softening occurred simultaneously. Moreover, the abundant dislocations produced by the deformation offer efficient diffusion paths allowing quick segregation of the alloying

elements to the boundary areas, as indirectly confirmed by the results in Table 4.2.

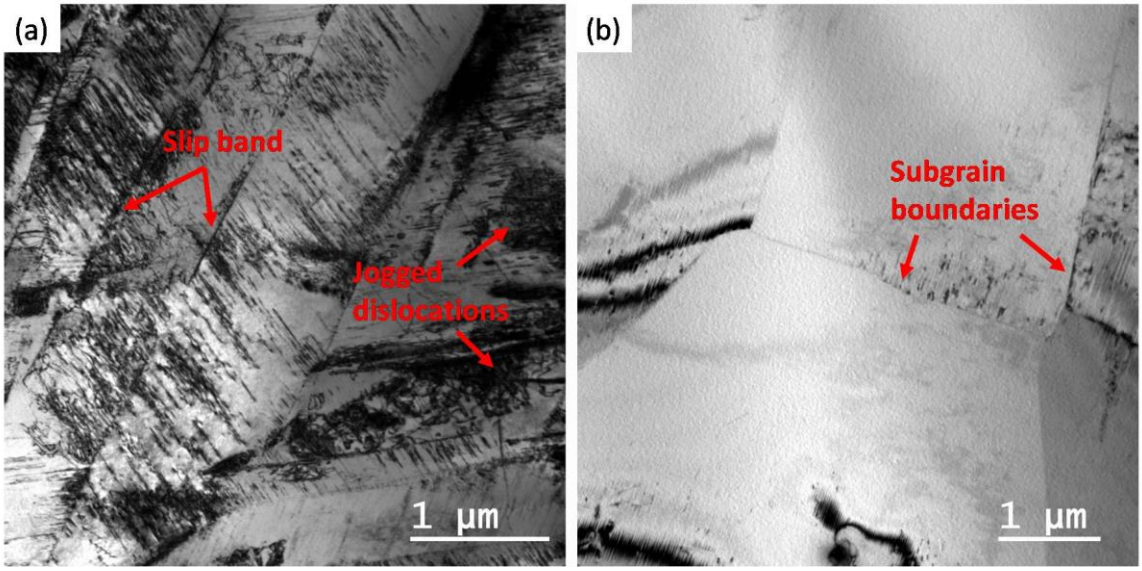

Fig. 4.10 TEM bright field micrographs of Ti-5553 hot compressed at 800°C to a strain of 0.7 under the strain rate of $0.0005s^{-1}$.

4.4 Discussions

The above results show that during the hot compression of the present Ti-5553, the β phase was subject to three processes: deformation, softening and transformation to α phase. The phase transformation happened when softening was well in progress and thus interwove continuously with the deformation of the β matrix and the softening.

4.4.1 Influence of deformation on nucleation site and morphologyof α precipitates

Two microscopic phenomena occurred and exerted important influences on the nucleation site and the morphology of the α phase. One is the significant grain refinement and elongation of the β phase and the other is the serration of β grain boundaries, as seen in Fig. 4.3 and 4.6(c). Due to the former effect, the initial coarse βgrains are filled with large amount of low and high angle boundaries. The spacing between the boundary segments with close orientations are around 40μm (Fig. 4.7(c)) that is roughly the thickness of the PFZ. These boundaries offer favorable nucleation sites for α. As the transformation is diffusive, the formation of α along the boundaries attracts the α stabilizing element, Al, and repels the β stabilizing elements to the

grain interiors. Owing to the continuous deformation, large amount of crystal defects, especially dislocations are produced, offering efficient diffusion channels. In this sense, the repartition of alloying elements are more efficient with much shorter intragranular diffusion distance due to the fragmentation, hence α phase forms mainly at low and high angle β boundaries and very rarely in grain interiors, as illustrated in Fig. 4.4(c).

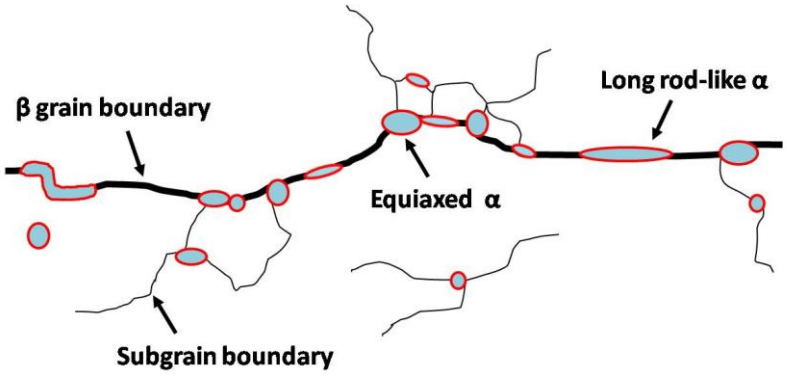

Fig. 4.11 Illustration of α precipitation on serrated β grain boundaries-"necklace" microstructure.

As the β boundaries are serrated with large amount of boundary ledges and steps, on one hand they offer favorable individual nucleation sites, but on the other hand they prevent the already formed α particles from growing smoothly to reach their neighboring particles and to form continuous α along the boundary. Certainly the growth of the α nuclei also depends on the coherency degree of the interphase boundaries [96]. With the intensified local crystal distortion induced by deformation, α/β interphase boundaries lost the coherency if they were coherent at the beginning of the phase transformation. Thus α nuclei are inclined to grow into spheres instead of plates to decrease the total interfacial area, hence interfacial energy. In this way, the α precipitates formed along the β boundaries are discontinuous and in particle shape. For the continuous α that precipitates at the early state of deformation and along undisturbed β boundaries (Fig. 4.2(a_4)), fragmentation and spheroidization should happen during the subsequent deformation. This could be realized primarily through the classical boundary splitting mechanism [85] and then followed by spheroidization by means of termination migration [63, 93, 94]. Due to the specific influences of deformation on α nucleation sites and α morphology, the characterized "necklace" microstructure is obtained, as illustrated in Fig. 4.11.

4.4.2 Influence of deformation on orientation relationship between α and β

The characteristic deformation amount, deformation rate and spatial distribution dependent deviation of α from BOR with β suggests that at the beginning of the formation of α, the BOR is maintained as the case of in the heat treated specimens, however, with the deformation, the BOR is gradually lost. The deformation was mainly accommodated by the β phase due to the relatively smaller size and less volume fraction of α phase. As the deformation temperature was relatively high and the deformation rate was relatively low, dislocations created by deformation had time to migrate, giving rise to the occurrence of dynamic recovery that reorganize the dislocations leading to the rotation of the crystalline lattices. Moreover, as the mechanical properties of β and α are different, the lattice rotation at the β/β boundary parts and the β/α parts are not the same and thus uncoordinated [141]. This may cause the loss of the BOR between the β and the boundary α particles.

4.4.3 Deformation induced phase transformation retardation

Thermodynamically, Gibbs free energy change ΔG of a transformation under deformation can be expressed as $\Delta G = V\Delta G_V + A\Delta G_r + V\Delta G_S + \Delta G_d$, where ΔG_V, ΔG_r and ΔG_S are the volumic free energy change, interfacial energy and elastic strain energy, respectively, andΔG_d is the stored energy provided by deformation.ΔG_V and ΔG_d represent the driving force for the transformation, whereas ΔG_r and ΔG_S the energy barriers to the transformation. Under the present deformation (at 800°C), although the driving force for phase transformation is increased by the addition of the stored energy provided by deformation, dynamic stress induce phase transformation (DSIPT) did not happen but on the contrary it was retarded. This is due to the occurrence of DRV/DRX induced by hot deformation. Actually, the two transformation processes, DRV/DRX and β→α transformation, occurred competitively during the hot compression. Although the two processes are diffusive in nature, the efforts required to achieve the two are not the same. For softening, it is a restoration process, reducing the quantity of defects in crystals. It involves neither repartition of alloying elements nor collective crystal structure change, as the case of β to α phase transformation. The energy barrier for DRV/DRX is smaller. Therefore, it requires less effort (lower driving force) to

overcome the energy barriers. The stored energy provided by the deformation is firstly consumed by softening before it reaches the level that is sufficient to drive the phase transformation. In this way, the phase transformation is retarded. This coincides with results in the Ref. [12, 147]. It should be noted that the two transformations have inverse temperature dependence. For DRV/DRX, it occurs above the theoretical temperature and the driving force increases with the increase of the actual temperature, whereas for β to α phase transformation, the effective transformation temperature is lower than the equilibrium temperatureand the driving force increases with the decrease of the temperature. Thus there should exist a transit temperature (T_{trans}) above which DRV/DRX is prevalent and phase transformation inhibited but below which DRV/DRX is suppressed and phase transformation promoted, as illustrated by Fig. 4.12. In the latter case, the DSIPT occurs that has been observed in some hot deformation process of Ti alloys [52].

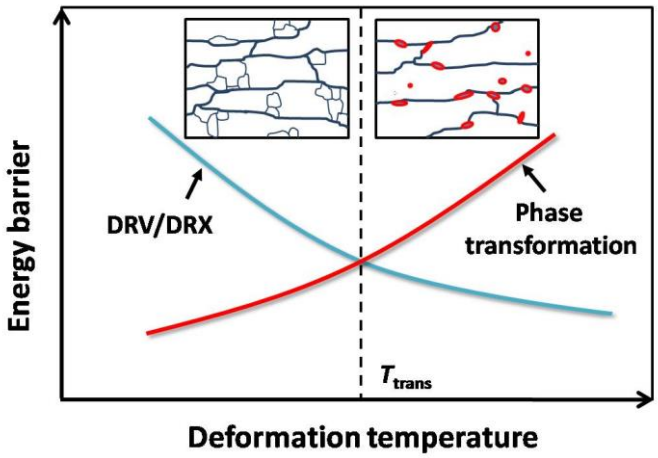

Fig. 4.12 Illustration of the completion between DRV/DRX and phase transformation.

Clearly other deformation parameters, such as strain and strain rate, may have also influence on the T_{trans}, depending on their kinetic effect on the softening process. Large strain and high strain rate would inhibit the softening process, thus reduces the retarding effect of phase transformation.

4.5 Summary

The β to α phase transformation of Ti-5553 during hot compression at 800°C, in terms of

nucleation site, morphology, orientation relationship and transformation kinetics, was studied. Several conclusions can be drawn from the studies.

During the deformation at higher temperature in the α+β region, equiaxed or short rod shaped α precipitates (1~2μm) mainly form on the high angle grain boundaries and low angle grain boundaries but seldom in β grain interiors, forming a "necklace" microstructure. This is due to the formation of large amount of low angle and high angle boundaries produced by DRV/DRX that provides abundant nucleation sites. The defects induced by the hot compression also provide favorable diffusion paths for the repartition of the alloying elements and accelerate the repartition of the elements to the boundaries. As the deformation and the subsequent DRV/DRX happen in a continuous manner, boundary migration take place continuously. Due to this instability, the nucleated α cannot grow smoothly to form continuous precipitates.

The deformation and the subsequent DRV/DRX which happen in a continuous manner, destroys the BOR gradually between the α and β phases. The deviation of α_{GB} is larger than that of α_I. This is due to the continuous deformation and recrystallization that induces β grain migration and rotation. The coherency of the α/β interfaces is reduced due to the different and uncoordinated lattice rotation at the β/β boundary parts and the β/α parts. The deviation from the BOR increases both with the increased strain and decreased strain rate.

The phase transformation is obviously retarded during the hot compression due to the competitive effect of softening process. The stored energy is first consumed by DRV/DRX before it reaches sufficient level to drive phase transformation. In this way the phase transformation is retarded. Due to the inverse temperature dependence of the two transformations, there could exist a transit temperature (T_{trans}), above which the driving force for phase transformation is smaller than that for DRV/DRX, whereas below which the DRV/DRX is retarded.

Chapter 5 Microstructural evolution and α variant selection during low temperature thermo-mechanical treatments

5.1 Introduction

The variant selection (VS) of α phase during precipitation is determined by the interplay between the externally applied stress and the internal stress generated by the precipitation. Moreover, abundant defects would be induced during deformation. Thus, the VS mechanism and the crystallographic features during thermo-mechanical treatment might be much more complicated and severely restricted by the nature of the defects [44, 50, 51]. Limited work exists in the literature about β→α variant selection during thermo-mechanical treatment. In addition, various strain localization bands would be formed during the deformation. The deformation mechanism and α phase nucleation behavior in slip bands should be investigated in detail.

In this chapter, an in-depth study was conducted on variant selection mechanism of α precipitates and deformation mechanism of Ti-5553 alloy during low temperature (600℃) hot compression.

5.2 Experimental

Compression was applied isothermally at 600°C using a Gleeble-3500 thermo-mechanical simulator (Fig. 2.4 (a) in ***Chapter 2***). The hot compression was performed at two different strain rates to two different strains. The detailed deformation parameters are given in Table 5.1. Prior to each compression, the specimens were heated to the isothermal temperatures at a rate of 25°C/s and then held for 10s before the deformation to ensure a homogeneous temperature. After compression, all specimens were immediately cooled in water in order to retain the deformed microstructures.

As references, the same numbers of specimens with the same initial microstructure were heat treated at 600°C, respectively, under the same thermal conditions as those of the hot compressions.

Table 5.1 Detailed hot compression parameters.

Temperature (°C)	Strain rate (s^{-1})	Strain	Corresponding isothermal holding time (min)	Cooling
600	0.001	0.7	11.5	Water quenching
	0.01	0.7	1.2	
	0.001	1.2	20	

5.3 Results

5.3.1 Micostructural features

5.3.1.1 Microbands

Fig. 5.1 shows SEM SE micrographs of the specimens isothermally compressed at 600°C. Deformations were performed either at the same strain (0.7) but under two different strain rates ($0.01s^{-1}$ and $0.001s^{-1}$) (Fig. 5.1(a) and (b)) or at two different strains (0.7 and 1.2) but under the same strain rate ($0.001s^{-1}$) (Fig. 5.1(b) and (c)). The two groups of deformation represent three isothermal holding times: 1.2min, 11.5min and 20min, respectively. Very different from the deformed microstructures obtained at 800°C in ***Chapter 4***, the microstructures, as shown in Fig. 5.1, contain large amount of regularly spaced bands (highly contrasted) about 500nm in width. In certain grains, the bands appear with several orientations, forming a kind of reticular structure (Fig. 5.1(a_2)). The morphology of the bands is deformation dependent. At higher strain rate, the bands are sharper and straighter (Fig. 5.1(a_1) and (a_2)) but with the decreasing strain rate, the bands become diffused and deviated (Fig. 5.1(c) and (d)). With increasing strain, the spacing of the bands turns out to be smaller and the number of bands increases (Fig. 5.1(d)). Moreover, these traces widen gradually with increasing strain and decreasing strain rate (Fig. 5.1(c)(d)). Steps are formed at the intersections of the bands with the initial β grain boundaries,

as shown in Fig. 5.2, evidencing that the deformation is localized in the band areas. Thus the bands can be considered as strain localization areas that accommodate the macroscopic deformation. The relation of these bands with the potential deformation modes of BCC metals, will be studied later in ***Section 5.3.3***.

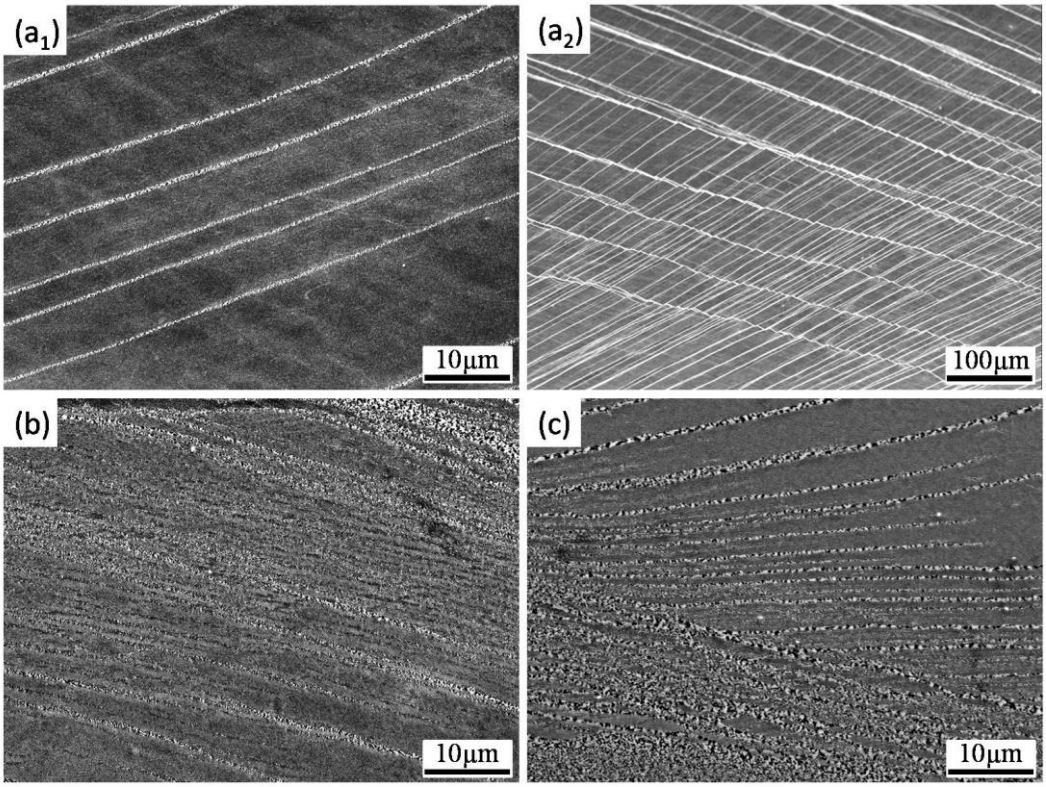

Fig. 5.1 SEM SE micrographs of Ti-5553 hot compressed at 600°C to (a) 0.7 under $0.01s^{-1}$, (b) 0.7 under $0.001s^{-1}$ and (c) 1.2 under $0.001s^{-1}$.

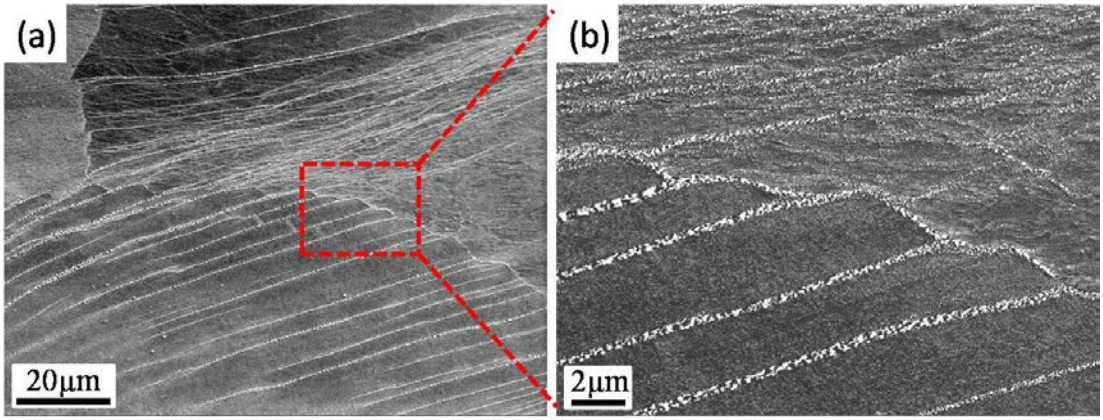

Fig. 5.2 SEM SE micrographs of the specimen hot compressed at 600°C to 0.7 at $0.01s^{-1}$. (a) Steps formed at the intersections of the bands with the initial β boundary and (b) a zoomed micrograph of the area outlined by the dashed box in (a).

Examination at higher magnifications revealed that the band areas in all the deformed specimens are composed of equiaxed constituents (around 50~200nm in diameter), whereas the areas between the bands consist of lamellar constituents (about 20nm in width), as shown in Fig. 5.3. The lamellae are organized in colonies, as seen in Fig. 5.3(a_3), (b_3) and (c_3). The two kinds of microstructural constituents coarsen, from about 50nm to 200nm for the equiaxed constituents and from about 15nm to 20nm for the lamellas, with increasing deformation time, represented by decreasing strain rate at constant strain or by increasing strain at constant strain rate. In addition, with the decrease of the strain rate (Fig. 5.3(b_3)) or the increase of the deformation (Fig. 5.3(c_3)), the lamellae become less straight or even fragmented, indicating that the formed lamellae are subject to deformation.

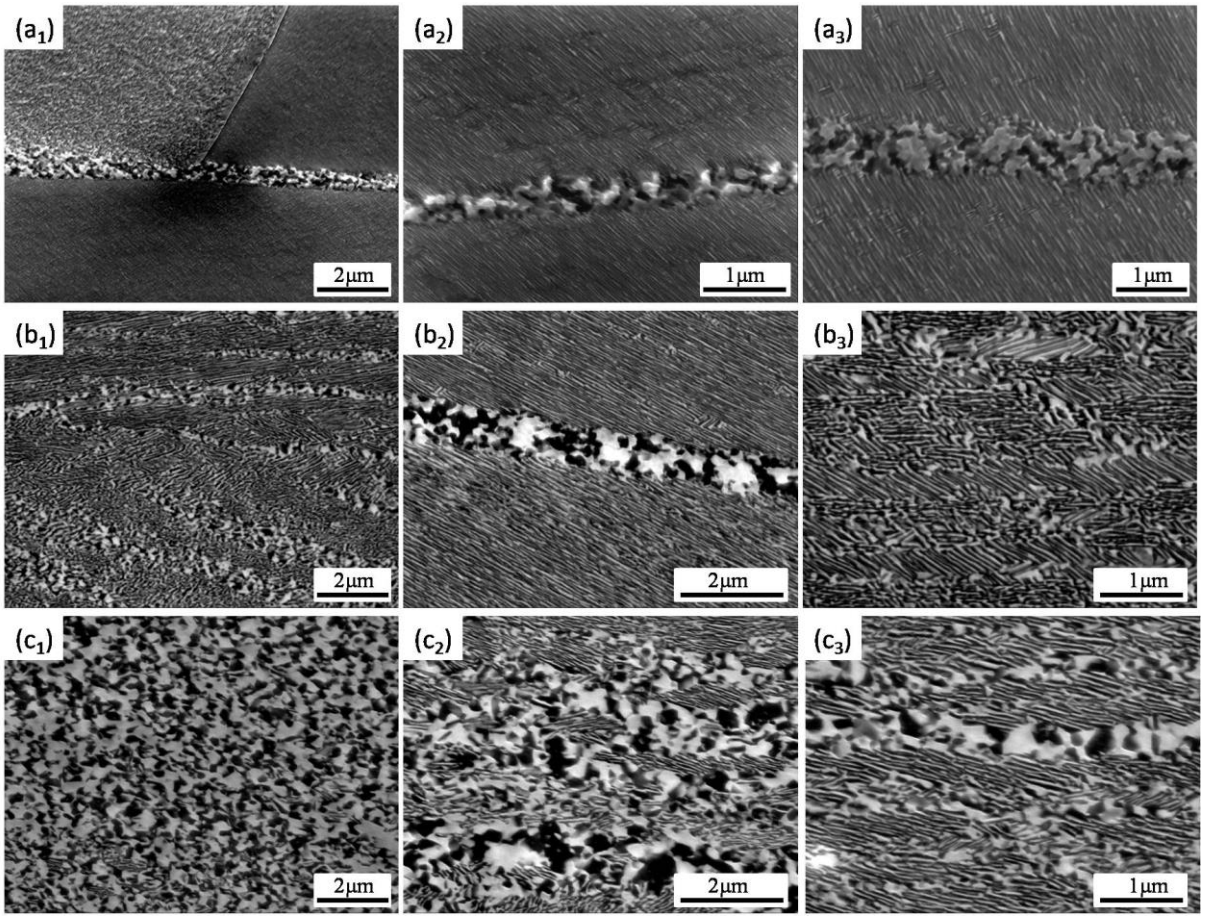

Fig. 5.3 SEM SE micrographs of hot compressed Ti-5553 alloy at 600°C to (a) 0.7 at $0.01s^{-1}$, (b) 0.7 at $0.001s^{-1}$ and (c) 1.2 at $0.001s^{-1}$.

5.3.1.2 Phase constituent

Further TEM imaging and SAED analyses showed that the equiaxed constituents consist of mixed α and β grains, as shown in Fig. 5.4(a). The SAED pattern shows that the α and the β reflections tend to form arcs, suggesting the randomization of the crystallographic orientations of the two phases. For the lamellar constituents, they are composed of alternatively distributed α and β plates, maintaining Burgers OR, as shown in Fig. 5.4(b). The SAED pattern displays single crystal feature for the two phases, indicating that the lamellae of the same colony possesses the same crystallographic orientation.

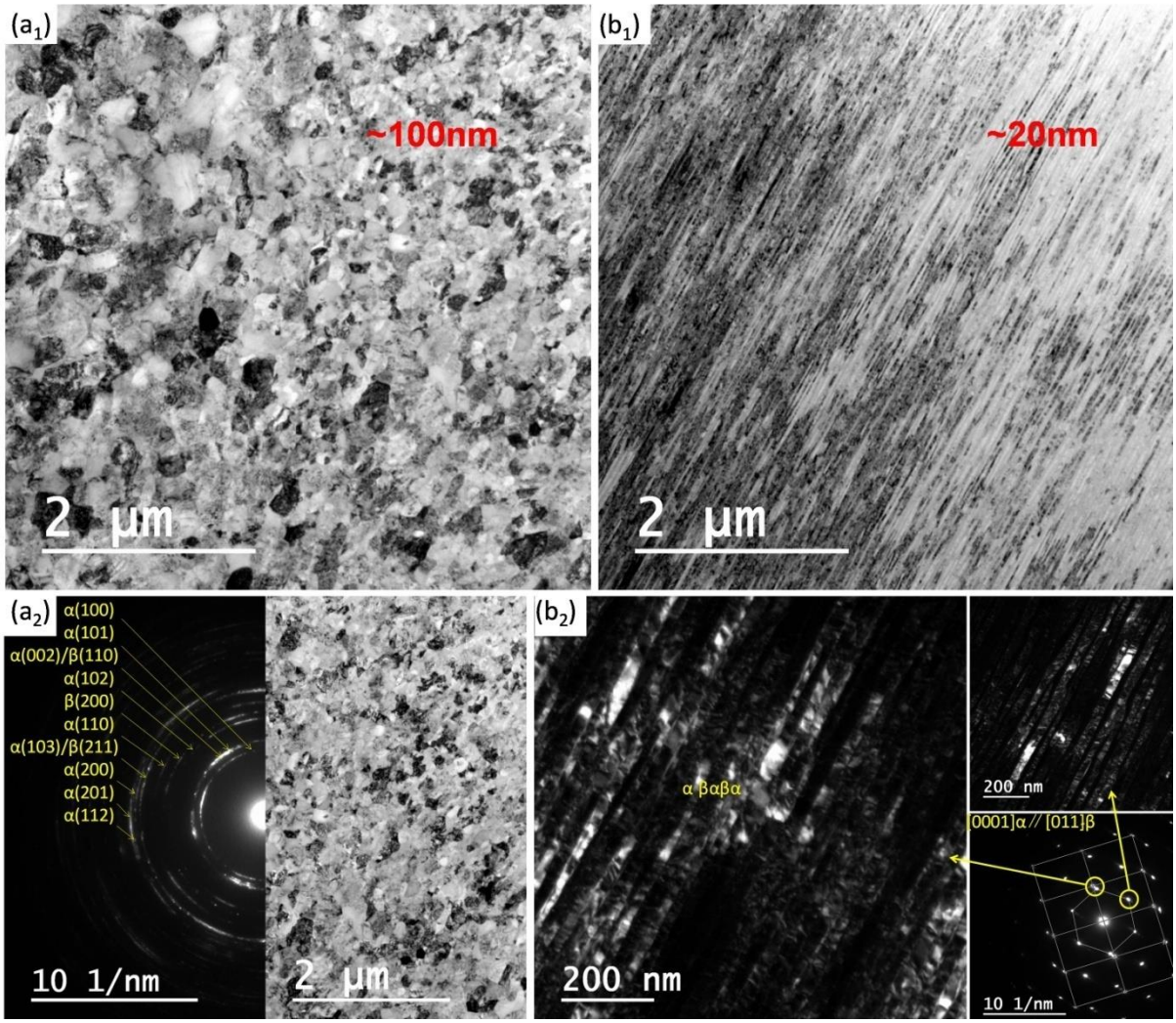

Fig. 5.4 TEM micrographs and SAED patterns of hot compressed Ti-5553 at 600°C to 0.7 at $0.001s^{-1}$: (a) bright field images and the SAED pattern of fine equiaxed microstructure and (b) bright field and dark field images and the SAED patterns of the lamellar microstructure.

For comparison, the SEM micrographs of three specimens aged at 600°C with an isothermal holding time corresponding to the hot deformation times (1.2min, 11.5min and 20min, respectively) are shown in Fig. 5.5. It shows that when held for 1.2min, α phase only forms continuously along β grain boundaries (Fig. 5.5(a)). When the specimens were held for 11.5min and 20min, respectively, large amount of plate-like α phase forms in the interiors of β grains (intragranular α, α_I) and in the vicinities of β grain boundaries (Widmanstätten α, α_{WGB}) (Fig. 5.5(b) and (c)). The three α constituents are typical for Ti-5553 when aged at 600°C. Such microstructures are very different from the aforementioned deformed microstructures.

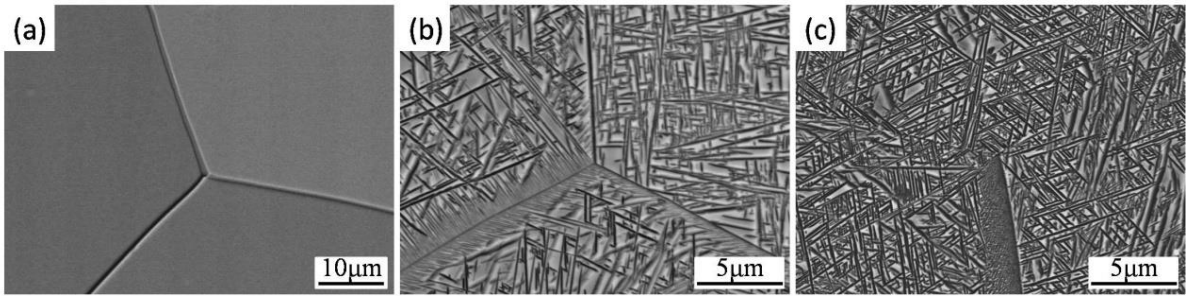

Fig. 5.5 SEM BSE micrographs of the Ti-5553 aged at 600°C for (a) 1.2min, (b) 11.5min and (c) 20min.

5.3.1.3 β→α phase transformation amount

The amount of α precipitates are quantified in the hot compressed specimens and their heat treated counterparts and displayed in Fig. 5.6. It is seen from the figure that the amount of α phase is significantly different between the deformed specimen to 0.7 at $0.01s^{-1}$ and the aged specimen (1.2min), about 41% and about 1.5% respectively. This indicates that the deformation promotes the phase transformation, the so-called Dynamic Stress-induced Phase Transformation (DSIPT). However, with the increase of the holding time for both the deformed and the aged specimens, the difference is greatly reduced from about 45% (0.7 at $0.001s^{-1}$) versus about 52% (11.5min) to about 54% (1.2 at $0.001s^{-1}$) versus about 53% (20min). This means that with the progress of the transformation, the equilibrium amount of transformation is reached in both deformation and ageing conditions. In this context, the deformation only changes the transformation kinetics but not the phase equilibrium.

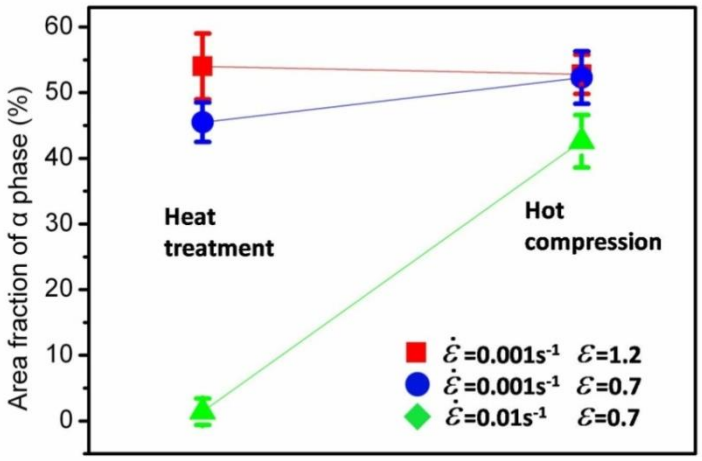

Fig. 5.6 Area fractions of α phase in the heat treated and the hot compressed specimens.

It should be noted that these results do evidence the existence of DSIPT at temperature lower than 800°C, which was predicted in ***Chapter 4***. This proves that there indeed exists a transition from deformation retarded transformation to deformation promoted transformation from high temperature to low temperature.

5.3.2 Crystallographic features of α under deformation

5.3.2.1 Orientation relationship with β

The orientation relationship (OR) between the α and the β phases in the two characteristic zones in the deformed specimens was further studied by TEM electron diffraction under both convergent beam and parallel beam. Fig. 5.7 is a TEM bright field image of the equiaxed α and β grains in the band areas. The orientations of the grains of the two phases were determined from the Kikuchi patterns produced under the convergent electron beam with the home made orientation determination software package Euclid Phantasies (EP) [115, 116] and represented with a triplet of Euler angles in Bunge notation [117]. The table in Fig. 5.7 shows the Euler angles of the α and the β grains indicated in the TEM bright field micrograph on the left of the figure. The three β grains and the four α grains were adjacent. The pole figures of the three β grains and the four α grains are displayed in the Fig. 5.8. No ORs including the Burgers OR (BOR) could be found between the adjacent β and α. These results demonstrate that no representative ORs exist between the two phases in the band areas. Moreover, the orientations

of the two phases are random. By opposition, the two phases in the areas between the bands are composed of lamellaes, as indicated by the TEM spot pattern in Fig. 5.4(b_2), respect the BOR.

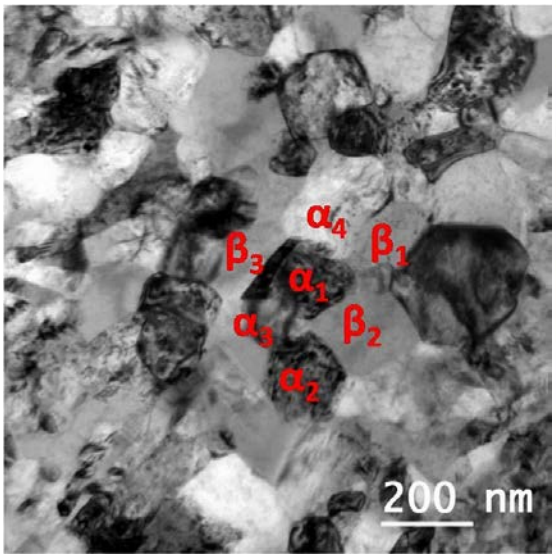

Phase	Euler angle (φ1, Φ, φ2)
α_1	300.16,59.52,259.39
α_2	352.89,39.57,160.61
α_3	186.73,58.88,334.69
α_4	299.46,61.70,246.45
β_1	106.91,8.37,54.86
β_2	215.44,42.52,5.15
β_3	211.81,43.19,310.58

Fig. 5.7 Left: TEM bright field micrograph of the equiaxed α and β grains in the band areas in Ti-5553 deformed at 600°C to 0.7 at $0.001s^{-1}$, and right: Euler angles of the selected α and β grains in the micrograph on the left.

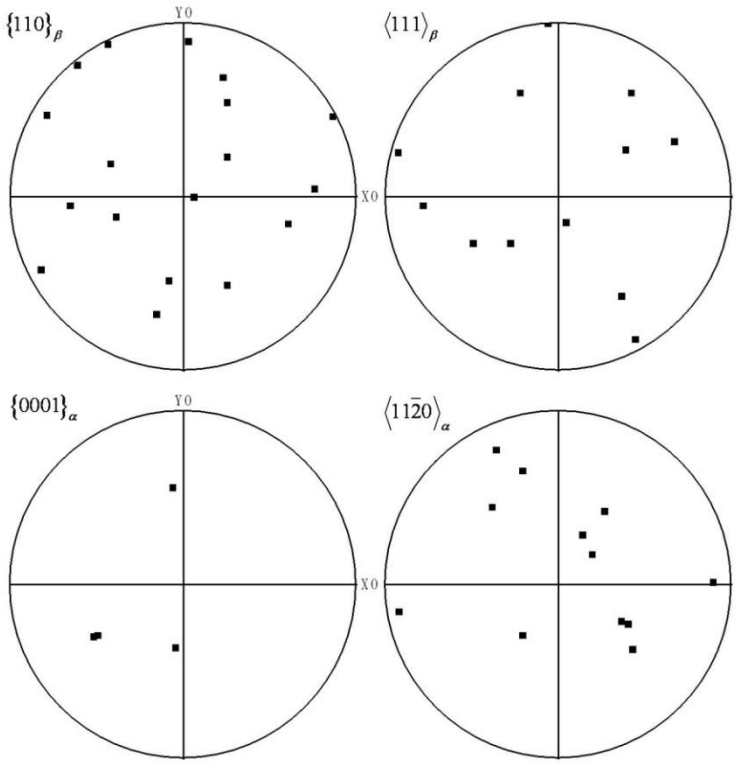

Fig. 5.8 $\{110\}_\beta/\langle 111\rangle_\beta$ and $\{0001\}_\alpha/\langle 11\bar{2}0\rangle_\alpha$ plane/direction pole figures of the three β grains and the four α grains selected in Fig. 5.7.

In the aged specimens, BOR is strictly followed by the two phases for all the three aforementioned α constituents (α_{GB}, α_{WGB} and α_I). This indicates that the deformation only affects the OR in the strain localization areas but not in the areas between the bands. This further evidences that the deformation in the band areas is very intensive but much lower in areas between the bands.

5.3.2.2 Variant selection of α phase

The number of variants in the aged specimens and in the areas between the bands in the deformed specimens was investigated by SEM/EBSD. As displayed in the SEM/EBSD IPF micrograph and the corresponding $\{110\}_\beta/\{0001\}_\alpha$ and $\langle 111\rangle_\beta/\langle 11\bar{2}0\rangle_\alpha$ pole figures in Fig. 5.9, all the 12 distinct α variants can be found in one original β grain. This is consistent with the results reported in the literature, as summarized in Table 1.3 in ***Chapter 1***. However, for the α phase in the areas between the bands in the deformed specimens, the number of variants is restricted. As shown in Fig. 5.10, three distinct colonies with different habit planes (denoted α_1 (vertical), α_2 (horizontal) and α_3 (diagonal)) can be found in one initial β grain (Fig. 5.10(a)). The three differently α colonies correspond only to two crystallographic orientations (Fig. 5.10(b)). α_1 and α_2 possess very close orientations but different habit planes. The misorientations between the three variants were calculated. The corresponding disorientations are given in Table 5.2. It is seen that the disorientations of α_1/α_3 and α_2/α_3 are $[11\bar{2}0]/88.58°$ and $[\bar{1}\bar{1}20]/87.78°$ respectively. They belong to the typical $\langle 11\bar{2}0\rangle/90°$ α variants (Table 1.4 in ***Chapter 1***). However, that of α_1/α_2 is $[2\bar{1}\bar{1}6]/5.18°$, which is not the specific orientation and may be attributed to the rotation of the α colonies during the compression. Moreover, the volume fractions of the three variants are not equal. α_1 and α_2 have a much higher volume fraction than α_3.

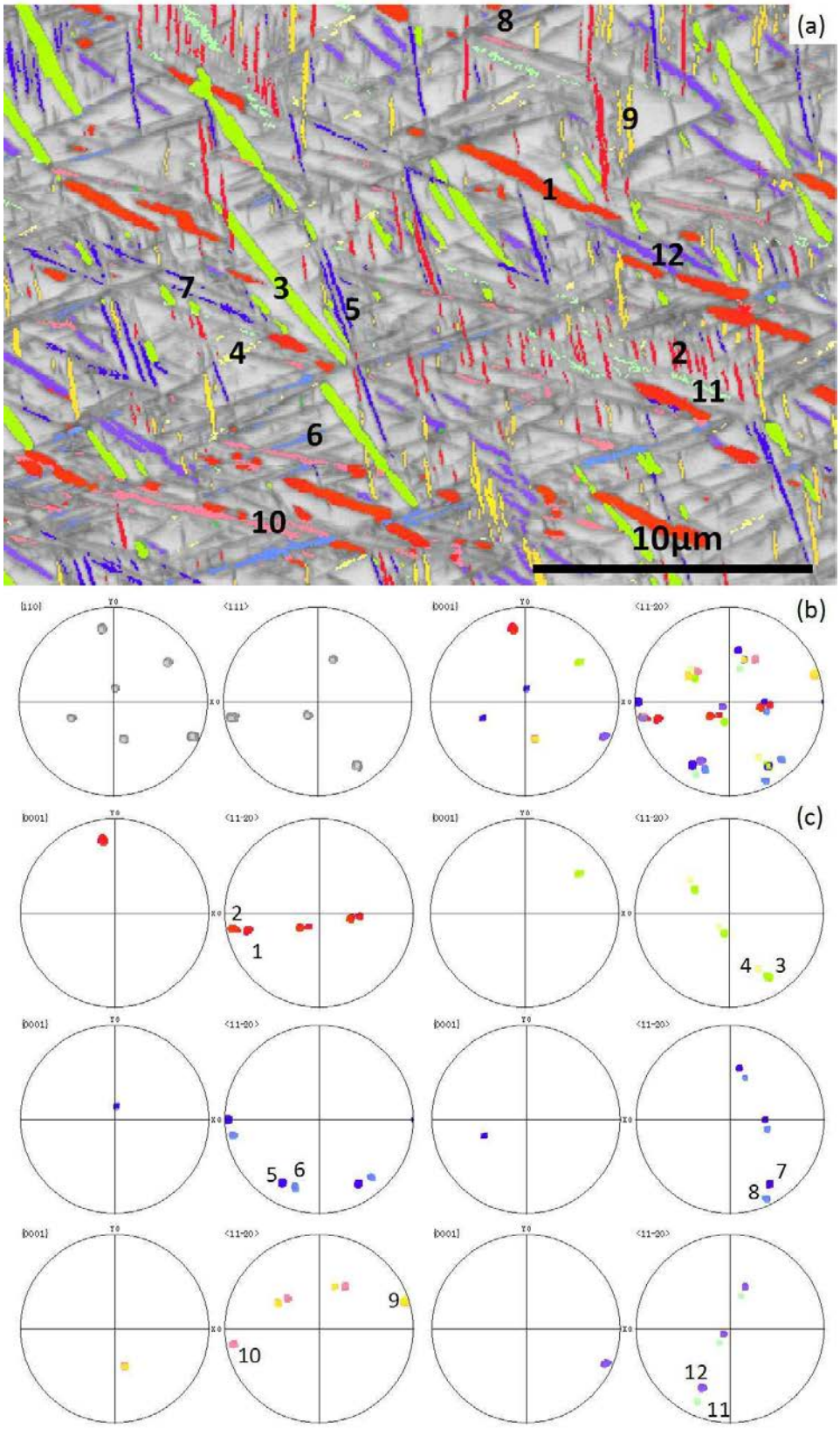

Fig. 5.9 (a) SEM/EBSD IPF micrograph of the Ti-5553 alloy aged at 600°C for 11.5min, and the corresponding $\{110\}_\beta/\{0001\}_\alpha$ and $\langle 111\rangle_\beta/\langle 11\bar{2}0\rangle_\alpha$ pole figures of (b) the β and the 12 α and (c) the 12 individual variants.

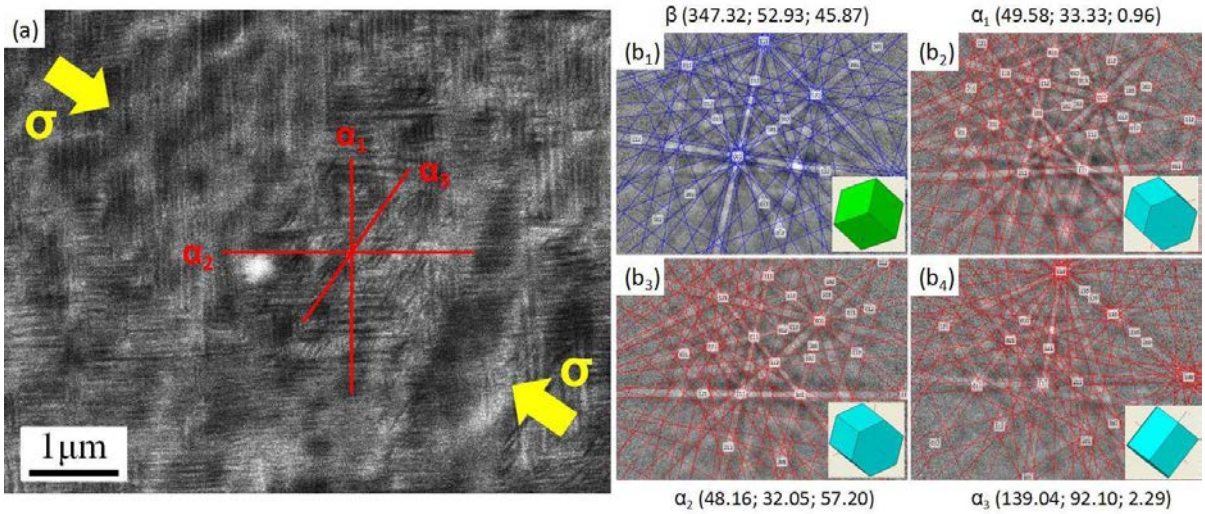

Fig. 5.10 (a) SEM/BSE micrograph of deformed Ti-5553 at 600°C to 0.7 at 0.001s^{-1}, and (b) the Kikuchi patterns of the β matrix and the α variants indicated in (a) and their indexations as well as the representative Euler angles and the illustration of the unit cell. In (a), the compression direction is indicated with the yellow arrows.

Table 5.2 Disorientation between the three kinds of α variants indicated in Fig. 5.10(a).

α variants	Axis/angle pairs
α_1/α_2	$[2\bar{1}\bar{1}6]$/5.18°
α_1/α_3	$[11\bar{2}0]$/88.58°
α_2/α_3	$[\bar{1}\bar{1}20]$/87.78°

Fig. 5.11 displays the pole figures of the plane and the direction of the β and the three α in Fig. 5.10 defined by the BOR. It can be seen from Fig. 5.11 that the $\{0001\}_\alpha$ poles of the three α coincide to the $(101)_\beta$ and $(\bar{1}01)_\beta$ poles of the β that are marked with the red circles, the blue rectangles and the green triangles, respectively. The $[2\bar{1}\bar{1}0]_\alpha$ poles of the three α coincide with the three $[\bar{1}\bar{1}1]_\beta$, $[\bar{1}11]_\beta$ and $[111]_\beta$ poles. Thus the BOR for the three α can be described as: α_1: $(101)_\beta \,||\, (0001)_\alpha$; $[\bar{1}\bar{1}1]_\beta \,||\, [2\bar{1}\bar{1}0]_\alpha$, α_2: $(101)_\beta \,||\, (0001)_\alpha$; $[\bar{1}11]_\beta \,||\, [2\bar{1}\bar{1}0]_\alpha$ and α_3: $(\bar{1}01)_\beta \,||\, (0001)_\alpha$; $[111]_\beta \,||\, [2\bar{1}\bar{1}0]_\alpha$ that correspond to No. 8, No. 7 and No. 4 relations in Table 1.3 (***Chapter 1***).

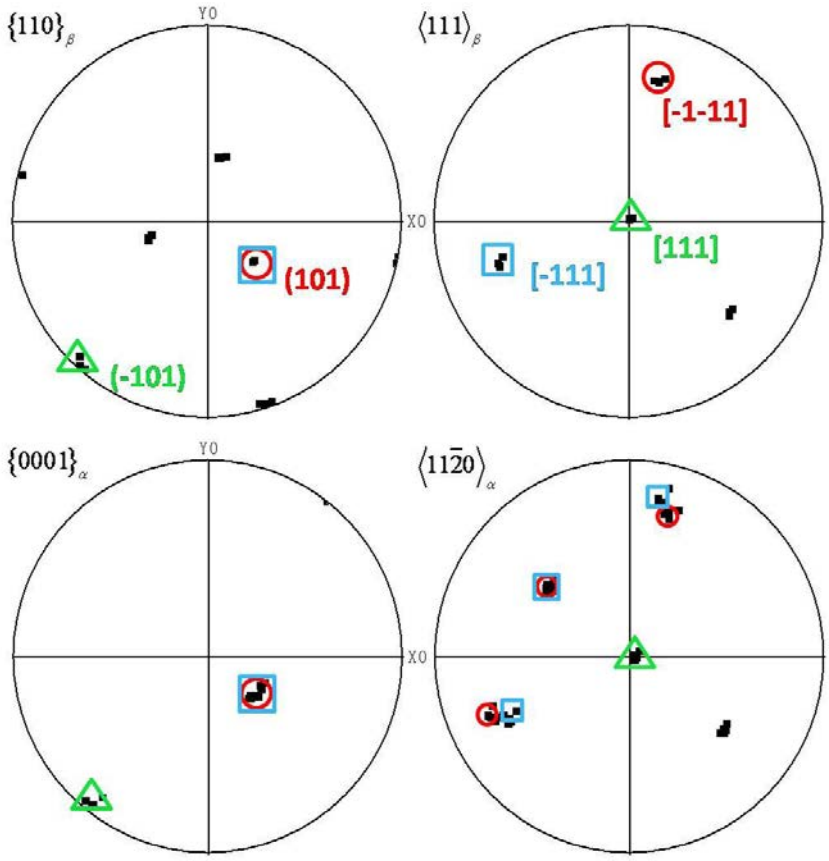

Fig. 5.11 $\{110\}_\beta/\langle 111\rangle_\beta$ and $\{0001\}_\alpha/\langle 11\bar{2}0\rangle_\alpha$ plane/direction pole figures of the three α variants and the β phase in Fig. 5.10. The red circles, blue rectangles and green triangles represent α_1, α_2 and α_3, respectively.

5.3.2.3 Habit plane between α and β

The habit planes between the α and β phase in lamellar microstructure of the deformed specimens were identified by verifying the published $\{11\ 11\ 13\}_\beta$ plane [43, 44, 148] and $\{334\}_\beta$ plane [149] using the trace analysis method. The results represented with the corresponding pole figures and with the indication of the interface traces are shown in Fig. 5.12. It can be seen from the pole figures Fig. 5.12(b)(c), the $\{334\}_\beta$ planes are closer to the traces of these three α variants than the $\{11\ 11\ 13\}_\beta$. Thus, the $\{334\}_\beta$ could be confirmed as the habit plane for the lamellar α in the present deformed specimen. The detail crystallographic orientations are shown in Table 5.3.

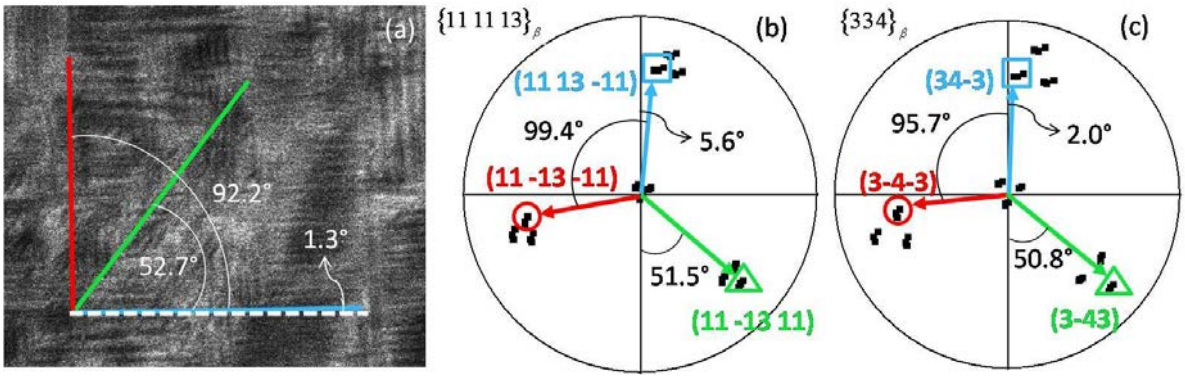

Fig. 5.12 (a) SEM/BSE micrograph of deformed Ti-5553 at 600°C to 0.7 at 0.001s^{-1}, (b) $\{11\ 11\ 13\}_\beta$ pole figures of the β phase and (c) $\{334\}_\beta$ pole figures of the β phase. The corresponding traces of α/β interfaces and the microstructures are indicated. The colors of red, blue and green in (b)(c) represent α_1, α_2 and α_3, respectively. Their inclination angles with respect to the horizontal axis are indicated with the white dashed line.

Table 5.3 Crystallographic parameters of the three α variants with three different stretching directions.

Variants	Plane (BOR)	Direction (BOR)	Habit plane
α_1	$(101)_\beta \,\|\|\, (0001)_\alpha$	$[\bar{1}\bar{1}1]_\beta \,\|\|\, [2\bar{1}\bar{1}0]_\alpha$	$(3,\bar{4},\bar{3})_\beta$
α_2	$(101)_\beta \,\|\|\, (0001)_\alpha$	$[\bar{1}11]_\beta \,\|\|\, [2\bar{1}\bar{1}0]_\alpha$	$(3,4,\bar{3})_\beta$
α_3	$(\bar{1}01)_\beta \,\|\|\, (0001)_\alpha$	$[111]_\beta \,\|\|\, [2\bar{1}\bar{1}0]_\alpha$	$(3,\bar{4},3)_\beta$

5.3.3 Slips of β phase in the band areas

The slips systems contributing to the formation of the bands were further identified by firstly calculating the Schmid Factors (SFs) of all possible slip systems of a BCC crystal and their slip traces on the macroscopic sample surface, using the orientation of the β phase, and then comparing them with the trace orientation of the observed bands. The possible slip systems sharing the same macroscopic trace on the surface of the sample are further discriminated using their SFs. The slips with higher SFs are considered as the ones with higher potential.

The determination was done with the specimen deformed at higher strain rate (0.01s^{-1}) and with a lower strain (0.7). The examined area is close to the upper surface of the cylindrical

specimen (close to the anvil), where the strain is further reduced and the deformation bands are straight and sharp. As β phase is not much deformed, especially in the areas between the bands, the orientation of the initial β grains should not be too far from that before deformation. As the transformation progressed very rapidly, the β grains are largely transformed to α. In the areas between the bands, the β lamellas are very fine (<20nm in width). It is impossible to obtain proper SEM/EBSD Kikuchi patterns to resolve the orientation of β phase, hence the orientation of the β phase was calculated indirectly from the measured orientations of the α variants under the determined BOR.

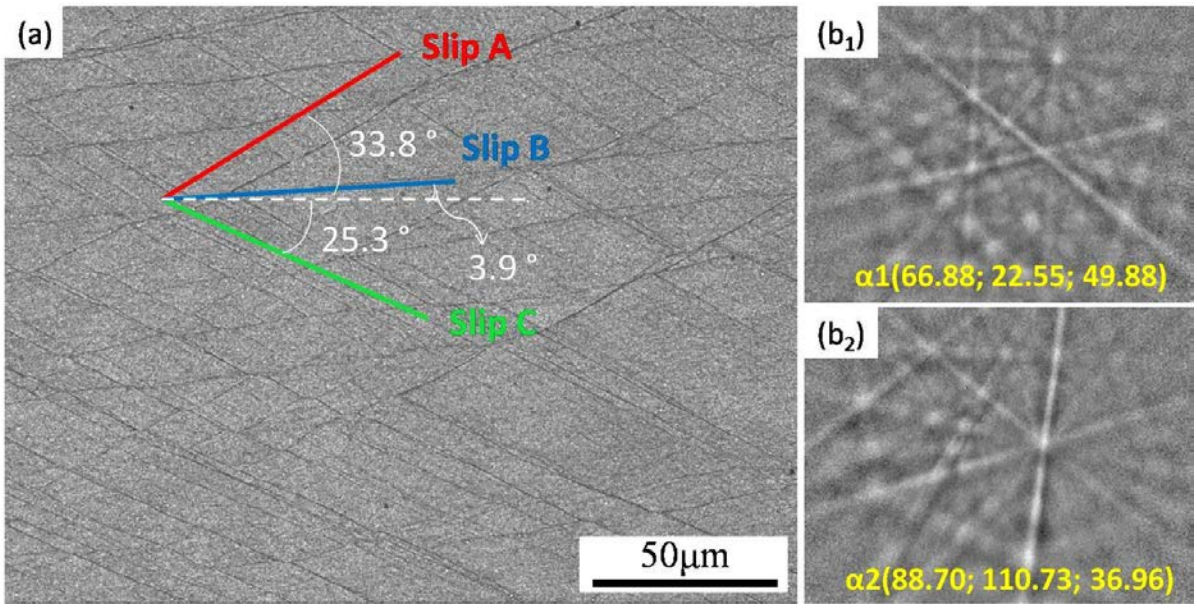

Fig. 5.13 (a) SEM/BSE micrograph of Ti-5553 deformed at 600°C to 0.7 at $0.01s^{-1}$ (b) Kikuchi line patterns of two distinct variants and their Euler angles. Three distinctly oriented bands are outlined in red (band A), blue (band B) and green (band C) and their inclination angles with respect to the horizontal axis are indicated with the white dashed line.

Fig. 5.13 displays an SEM/BSE micrograph of the deformed microstructure and the examples of the two distinct α variants. Obviously, three sets of bands (band A, band B, and band C colored indicated in red, blue and green) can be observed in Fig. 5.13(a). For an unambiguous determination of the orientation of the parent phase, up to four distinct orientations of the product phase could be needed [150]. However, this depends on the misorientation between the variants. In the present case it was possible to measure manually 23 α orientations in the same parent β grains. These 23 orientations correspond to the two variants

that are $\langle 11\bar{2}0\rangle_\alpha$/90° misoriented. Theoretically, these variant have two common potential parents that are 10.5° misoriented. However, due to deformation orientation corresponding to the same variant may be 5° appart. Using a clustering approach, we have selected for each variant the potential parent which overall was the closest to the majority of that the overall, meaning that it was possible to have a rough estimate of the parent orientation (within an uncertainity of about 8°).

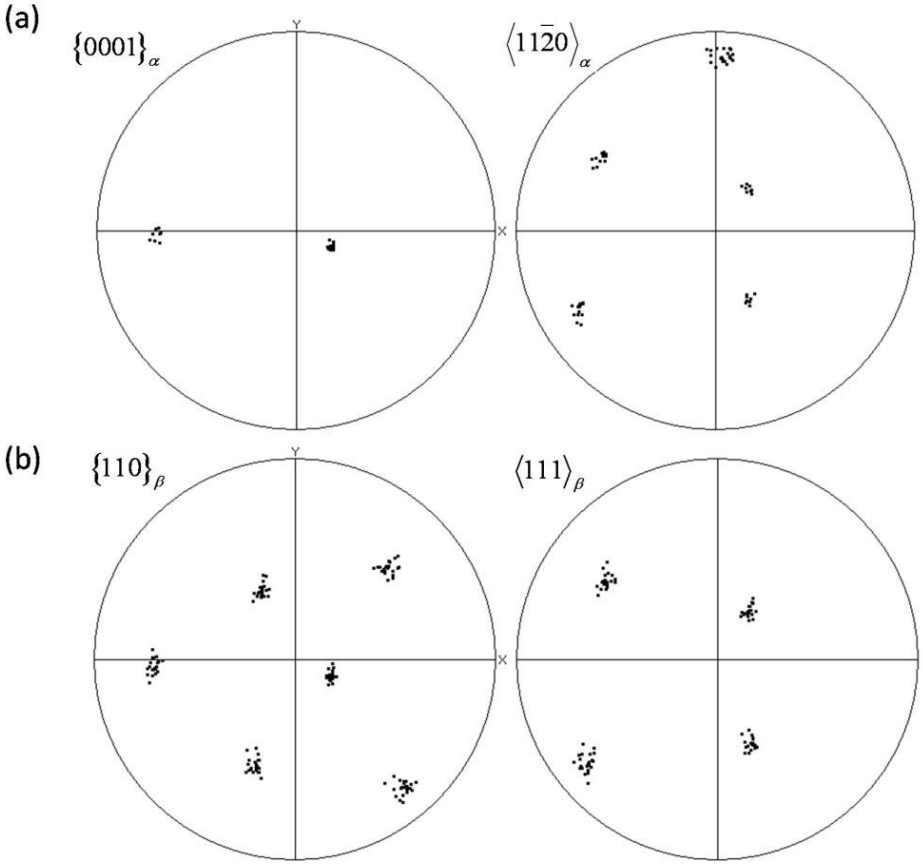

Fig. 5.14 (a) $\{0001\}_\alpha$ and $\langle 11\bar{2}0\rangle_\alpha$ poly figures of the 23 α randomly selected in the area shown in Fig. 13(a) and (b) $\{110\}_\beta$/$\langle 1\bar{1}0\rangle_\beta$ Pole figures of the β orientations calculated from the 23 experimental α orientations under BOR.

Their $\{0001\}_\alpha$ and $\langle 11\bar{2}0\rangle_\alpha$ pole figures are displayed in Fig. 5.14(a). The calculated β orientations represented with their $\{110\}_\beta$ and $\langle 1\bar{1}0\rangle_\beta$ poly figures are given in Fig. 5.14(b). It is seen that the calculated β orientations form a kind of orientation "cloud" with some spread but not very far, as the case of the 23 α variants in Fig. 5.14(a). From this orientation "cloud", the average orientation is calculated and taken as the initial orientation of the β grain. The Euler

angles of the average β orientation with respect to the sample coordinate system are (179.39°, 80.72°, 335.06°).

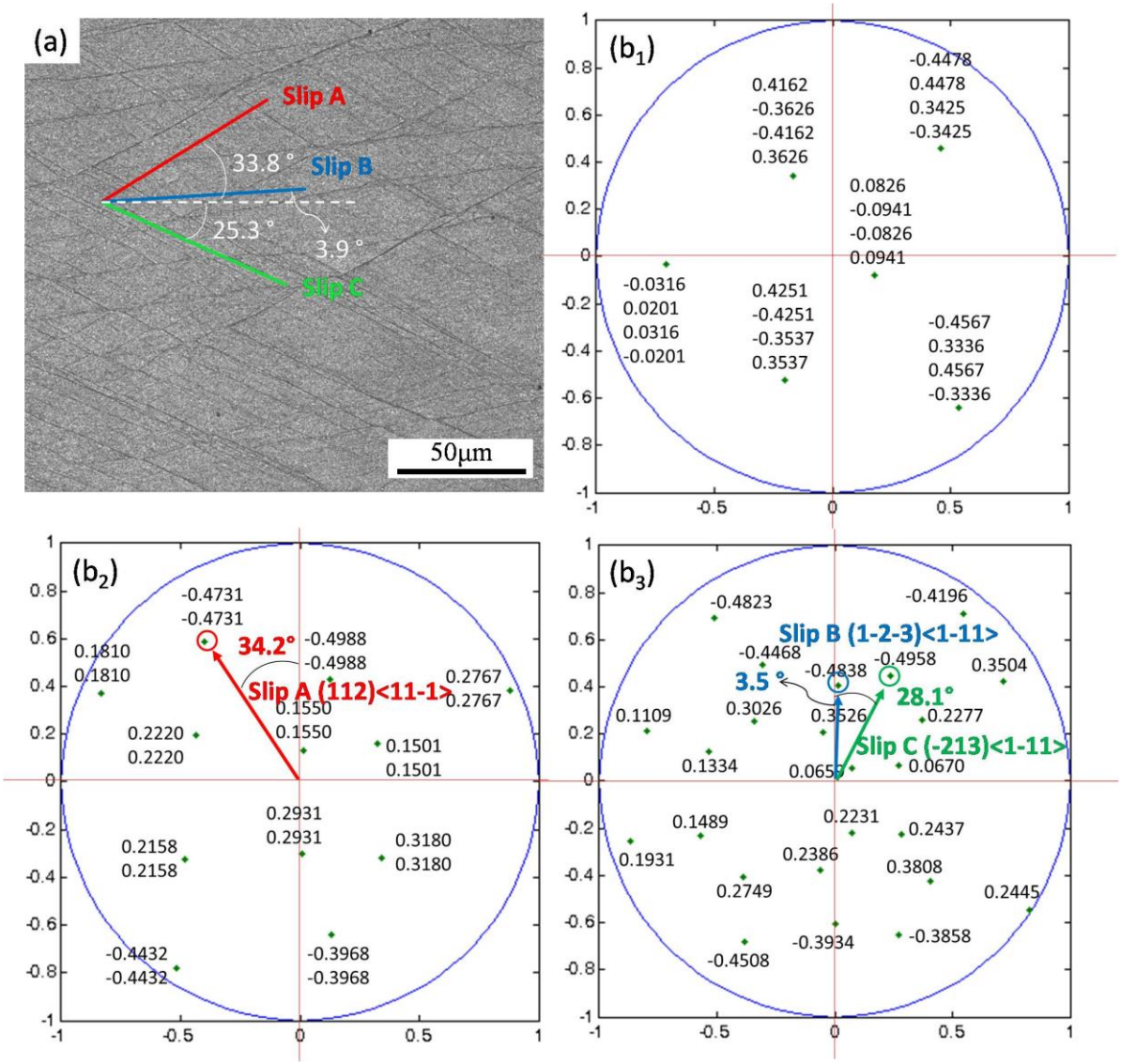

Fig. 5.15 (a) SEM/BSE micrograph of Ti-5553 deformed at 600°Cto 0.7 at 0.01s^{-1} (b) {110}, {112} and {123} pole figures of the β in (a). The SF values under the compression are indicated for each slip system. The slips systems correspond to the three distinctly oriented bands are circled in red, blue and green.

Using the determined orientation of the β phase, the possible slip systems were further analyzed. For BCC metals, the most energetically favorable slip direction is ⟨111⟩. The ⟨111⟩ slips can be realized on six {110} planes, twelve {112} planes and twenty four {123} planes. Based on such an assumption, the orientations of the three families of planes with respect to the sample coordination system are calculated and displayed as the respective plane pole figures in

Fig. 5.15, where the SFs of the corresponding slip systems are also indicated. By comparing the slip plane traces and taking into account of the value of the SFs, the three distinctly oriented bands A, B and C could be estimated as slip bands of $(112)[11\bar{1}]$, $(1\bar{2}\bar{3})[1\bar{1}1]$ and $(\bar{2}13)[1\bar{1}1]$ respectively.

5.4 Discussions

5.4.1 α phase nucleation behavior and microstructural evolution

As mentioned in ***Section 5.3.1.1***, all of the slip bands are occupied by fine equiaxed α precipitates and β grains, while irregular α particles, crooked α/β lamellae and regular clusters of α/β lamellae are distributed in the gaps betwwen slip bands. Because the initiation of the slip bands produced by dense dislocations is accompanied by the nucleation of α phase during the hot deformation, the slip bands would be the preferential nucleation sites. Abundant dislocations would be piled up in the band areas. Thus, many α nuclei could nuclear in the slip bands and grow up to a fine equiaxed microstructure [51], as Fig. 5.16(a) shows. Both the size of α particles and the width of slip bands would increase gradually with the increased strain.

On the other hand, the α platelets with certain stretching directions are favorable for nucleation and growth due to variant selection under the applied force. According to the SEM and TEM observations on the deformed lamellar microstructure, the detailed process of the evolution of α/β lamellae under the hot compression can be shown in Fig. 5.16(b) and described below.

When lower compression strain is applied, severe kinking of α/β lamellae occurred in the α/β lamellar colonies under the complicated shear stress state (upper of Fig. 5.16(b)). It should also be noted that the kinking of α/β lamellae should be related to the original orientation of the lamellae relative to the loading direction [98]. Bieler et al. [97] observed that globularization is difficult in colonies having their ***c***-axes parallel to the compression direction so that the prism and basal slip systems cannot be activated. And then, globularization (fragmentation) of the α/β lamellae may occur under the effect of dense dislocation configurations with the increased

strain. Actually, the kinking of α/β lamellae is the preparatory stage of fragmentation.

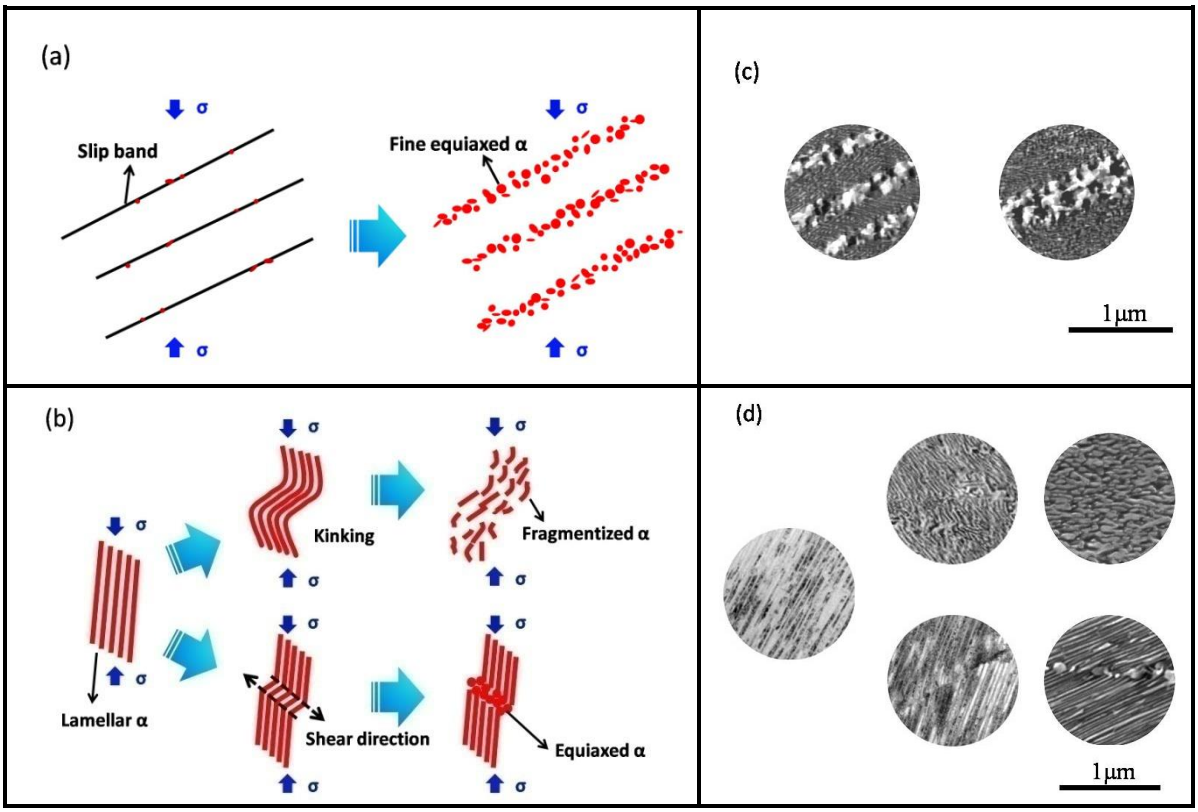

Fig. 5.16 Schematic diagram of α phase precipitation and evolution. (a) the nucleation and growth of α phase in the slip bands; (b) the evolution of α_I lamellar formed during the hot compression; (c) and (d) corresponding micrographs of (a)and (b), respectively.

When higher compression strain is applied, slip bands might form directly and across α/β lamellae gradually (bottom of Fig. 5.16(b)). Thus, the α plates are easier to be fragmented under the high shear strain. Actually, the initiation of the slip bands might be accompanied by the fragmentation of α/β lamellar in slip bands by intense dislocation activites. Ref. [151, 152] described that the refinement of grains in deformation bands as a recrystallization behavior. However, the α/β lamellar structures are really thin with ~20nm in width in the present work. Thus, the fragmentation and globularization is speculated to play an important role in the grain refinement process within the slip bands and GBs. Moreover, the increased deviation from BOR of α/β due to the deformation would accelerate the kinetics of α lamellae fragmentation [96, 153]. The fragmentized α/β lamellae might be further broken and rotated in order to release the stresses, which led to the formation of randomly orientated nanocrystallites (Fig. 5.4). With the continuous increase of the strain, the adjacent α precipitates and β blocks would

be swept into the localized strain region. In other words, the slip band thickens at the expense of the surrounding α precipitates and β blocks. Another important point is that the diffusion rate of alloy elements is faster at GBs and slip bands, which would contribute to the nucleation and growth of α phase. That is why the size of α precipitates on slip bands and GBs is larger than the width of α_I plates (Fig. 5.3).

The above observations and characterizations clearly indicate that the microstructural evolution (slip bands, kinking, fragmentation or globularization) strongly depends on deformation parameters and the original orientation of the lamellae relative to the loading direction. And the same rules illustrated in Fig. 5.16 might be also adaptable to other β or α+β titanium alloys as well.

5.4.2 Deformation mechanism of metastable β titanium alloys

The actual deformation behavior of titanium alloys strongly depends on the degree of stability of the β phase [104]. The β phase stability increases, and the deformation mode changes from twinning/stress-induced martensite formation to slip, as Fig. 1.10 in ***Chapter 1*** shows. The β phase has a approximately critical $[Mo]_{eq}$ of 8.8 wt. % in the present Ti-5553 alloy, which can be attributed to the fact that the addition of enough β-stabilizing elements inhibits the formation of stress-induced martensite and twin [104]. Furthermore, the dislocation slip systems are controlled by thermally-activated process. That is why no martensite and twin be observed in the higher (800℃ , in ***Chapter 4***) and lower (600℃ , in ***Chapter 5)*** temperature deformation processes. Thus, dislocation slip is leading deformation mechanism for the Ti-5553 alloy. The slip was also observed in other Ti-alloys by S. Hanada et al. [112] as a predominant deformation mechanism.

Compared with the results of high temperature deformation at 800℃ in ***Chapter 4***, there is no significant change in the deformation mechanism of Ti-5553 alloy. Well-defined thin slip lines in high temperature deformation are replaced by slip bands at low temperature deformation. The β grains in the alloys are sheared relative to each other by the generation, movement, and rearrangement of dislocation in most titanium alloys upon hot deformation.

Thus, each β grain might possess its own set of dislocations on the preferred slip planes that are distinctly oriented from those of the adjacent grains (Fig. 5.2). That is consistent with the fact that the multiple- or cross-slips of BCC metal could appear easily due to the high stacking fault energy. However, no cracks initiated along the bands or at the intersection sites between the slip bands and the grain boundaries, which implies excellent workability of Ti-5553 alloy [85].

5.4.3 α variant selection mechanism under the applied force

It is clear that the local strain state of an untransformed β matrix is a key factor in controlling variant selection during precipitation and the final transformation texture. However, the challenges to study variant selection during β→α phase transformation under the influence of stress are twofold: first, one needs to determine strain distribution in an elastically anisotropic and inhomogeneous medium under a given applied stress or strain condition; second, one needs to describe interactions of local stress with coherent and semi-coherent α precipitates, i.e. to describe interactions of local stress with evolving two-phase microstructures.

Table 5.4 displays the deformation gradient tensors of α variants expressed in the macroscopic sample coordinate system. The components $e_{ij}(i = j)$ stand for the normal strain that represent the dilatation along i directions normal to the plane perpendicular to j. The components $e_{ij}(i \neq j)$ are shear strains that indicate the shears in i direction and in the plane normal to j. In the present case, for the deformation gradient tensors of the uniaxial compression deformation, the components e_{2j} would be the crucial analysis objects because the direction i=2 corresponds to the compression axis. Thus, e_{11}>1, e_{22}<1 and e_{33}>1; and e_{21}, e_{23} could not be very large. Thus, only two deformation gradient tensors of α variants could be find satisfactory in Table 5.4, i.e., NO. 4 and No. 10. These two α variants could provide a better accommodation to the compression long the Y direction. This leads to the significant variant selection of α phase during the hot compression test.

Table 5.4 Deformation gradient tensors of all possible α variants expressed the macroscopic sample coordinate system.

Variant No.	Deformation matrix
1	$\begin{pmatrix} 0.960471 & 0.026291 & 0.038309 \\ -0.11719 & 1.08555 & 0.071638 \\ 0.076275 & -0.03727 & 0.97207 \end{pmatrix}$
2	$\begin{pmatrix} 0.969876 & -0.12806 & 0.072013 \\ 0.01542 & 1.075777 & -0.02644 \\ 0.034047 & 0.082476 & 0.972437 \end{pmatrix}$
3	$\begin{pmatrix} 0.97546 & -0.01663 & 0.004277 \\ -0.01953 & 1.01284 & 0.001423 \\ 0.176865 & 0.065414 & 1.029791 \end{pmatrix}$
4	$\begin{pmatrix} \mathbf{1.016488} & \mathbf{-0.02188} & \mathbf{0.001718} \\ \mathbf{-0.01063} & \mathbf{0.957177} & \mathbf{0.001228} \\ \mathbf{-0.02911} & \mathbf{-0.17992} & \mathbf{1.044425} \end{pmatrix}$
5	$\begin{pmatrix} 0.991467 & -0.01366 & 0.180518 \\ -0.01075 & 1.014989 & 0.067074 \\ 0.007929 & 0.003083 & 1.011634 \end{pmatrix}$
6	$\begin{pmatrix} 0.973722 & 0.038568 & 0.004022 \\ 0.03023 & 0.995028 & -0.0016 \\ -0.13774 & 0.115549 & 1.049341 \end{pmatrix}$
7	$\begin{pmatrix} 1.016776 & -0.00815 & -0.03129 \\ -0.01939 & 0.974137 & -0.18643 \\ -0.00046 & -0.00528 & 1.027178 \end{pmatrix}$
8	$\begin{pmatrix} 0.990742 & 0.001957 & -0.01458 \\ 0.156682 & 1.042204 & 0.06332 \\ -0.08337 & -0.00891 & 0.985145 \end{pmatrix}$
9	$\begin{pmatrix} 1.006462 & 0.160073 & -0.07754 \\ 0.005348 & 1.027393 & -0.00074 \\ -0.00875 & 0.071488 & 0.984236 \end{pmatrix}$
10	$\begin{pmatrix} \mathbf{1.096899} & \mathbf{-0.09896} & \mathbf{-0.06348} \\ \mathbf{0.052862} & \mathbf{0.940008} & \mathbf{-0.05189} \\ \mathbf{0.040308} & \mathbf{-0.06013} & \mathbf{0.981184} \end{pmatrix}$
11	$\begin{pmatrix} 1.090584 & 0.0386 & 0.030215 \\ -0.11322 & 0.945045 & -0.05746 \\ -0.07358 & -0.04922 & 0.982461 \end{pmatrix}$
12	$\begin{pmatrix} 0.983414 & 0.021841 & -0.14418 \\ 0.03018 & 1.002215 & 0.119879 \\ -0.00242 & 0.002725 & 1.032461 \end{pmatrix}$

5.4.4 Dynamic stress-induced phase transformation

From the results of ***Section 4.3.2.1*** in ***Chapter 4*** and ***Section 5.3.1.3*** in ***Chapter 5***, the effects of deformation on the transformation amount of α phase are completely different between high and low temperature deformation processes. The phase transformation is obviously retarded during the high temperature deformation due to the competitive effect of recovery and recrystallization. Whereas, DSIPT happened during the low temperature deformation for two reasons. The first one is the more nucleation sites and accelerating growth of α precipitates due to the deformation. The second one might be the retarded softening behavior during the deformation. By comparison, the latter might play a more important role in DSIPT because the amounts of α phase inside and outside of the slip bands are almost the same.

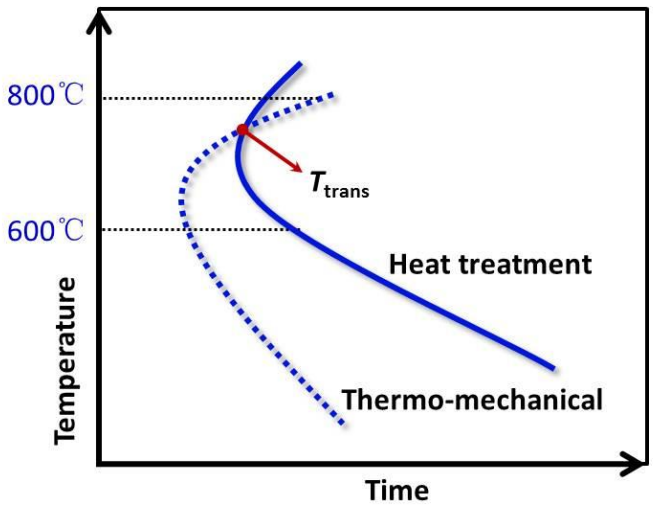

Fig. 5.17 TTT schematic diagram under the heat treatment and thermo-mechanical conditions.

The schematic diagram of the competitive relationship between phase transformation and softening is shown in Fig. 4.11. The energy barrier for phase transformation under the low temperature is much smaller than DRV/DRX. Therefore, it requires less effort (lower driving force) to overcome the energy barriers. The stored energy provided by the deformation is firstly consumed by phase transformation. In this way, the phase transformation is accelerated. This coincides with the results in the Ref. [52]. Fundamentally, the kinetics of β→α phase transformation is changed by the application of deformation. As the TTT schematic diagram Fig. 5.17 shows, above the T_{trans} (800℃), DRV/DRX is prevalent and phase transformation

inhibited. Whereas, below the T_{trans} (600℃), DRV/DRX is suppressed and phase transformation enhanced. The two transformation processes, DRV/DRX and β→α transformation, occurred competitively during the hot compression.

The dynamic α precipitation during hot deformation is supposed to strongly relate to the deformation parameters and manners. This competition mechanism is not only applicable for the deformation temperature but also strain and strain rate, which is not only found in the present work but is also often observed in other hot deformed Ti alloys.

5.5 Summary

The microstructure evolution and variant selection mechanism of α phase during the thermo-mechanical treatment at low temperature were studied in the Ti-5553 metastable β titanium alloy with single β phase initial microstructure. Meanwhile, the deformation mechanisms were also analyzed in detail. Several conclusions can be drawn from the studies.

Dislocation slip is leading deformation mechanism for the Ti-5553 alloy. Single or multiple-slip bands with two or three different propagating directions would form during the hot deformation process. The slip bands would be straighter and clearer in the higher strain rate deformation process. Moreover, the bands widen gradually with the increased strain and decreased strain rate. Considering the Schmidt factor and the slip trace directions in micrographs it was possible to identify slip systems.

Big differences could be found between the microstructures of hot compression and heat treatment specimens. A large amount of α phase with several different morphologies, such as lamellar α, equiaxed α and irregular α, precipitate during the hot deformation. The microstructure evolution (slip bands, kinking, fragmentation or globularization) strongly depends on deformation parameters and the original orientation of the lamellae relative to the loading direction. In the core region of the slip bands, equiaxed α/β grains, 50~200nm in grain size, are present without BOR. However, between the band regions, lamellar α and β phases, ~20 nm in width and with strict BOR, are distributed alternately.

Dynamic stress-induced phase transformation (DSIPT) of β→α process happened during the hot deformation should be due to the more induced deformation defects as the α phase nucleation sites and accelerated growth of α precipitates and retarded recovery or recrystallization. The amount of α precipitates in the deformed samples is more than that obtained under heat treatment conditions. These results are almost opposite to that of deformation at 800°C in ***Chapter 4***. Actually, it is a competitive mechanism between DRV/DRX and α phase nucleation, which depended on the deformation parameters and modes. This competition mechanism is not only applicable for the deformation temperature but also for strain and strain rate, which is not only found in the present work but also is often observed in other hot deformed Ti alloys.

It is different from the heat treated specimen, only two or three α variants would nucleate in local β matrix under the hot deformation condition, rather than 12 α variants form randomly during the heat treatment process. This variant selection mechanism is dominated by the stress field, i.e., stress-induced variant selection. The stress-induced variant selection mechanism could explain both deformation accommodation and energy perspectives. The habit plane of all the α variants were determined as $\{334\}_{\beta}$.

Chapter 6 Conclusions and Future work

6.1 Conclusions

In the present PhD work, firstly, the striations microstructure and the diffraction characteristics of the β phase of metastable titanium alloy were thoroughly investigated. Secondly, the α phase precipitation, orientation relationship between α and β as well as dynamic stress-induced phase transformation during thermo-mechanical treatments were investigated. Thirdly, the α variant selection mechanism under the simultaneous stress field and thermal field was figure out. Lastly, the deformation mechanism of metastable β titanium alloy was discussed. From the results of the present work, following main conclusions can be drawn:

(1) The structure of the β phase in the metastable titanium alloy is not "pure" body centered cubic. Large amount of planar defects are formed with a structure between that of the parent β phase and that of the α or the ω phase, demonstrating pre phase transformation tendency These intermediate structures are formed by atomic displacements on $\{110\}_\beta$ plane in $\langle 1\bar{1}0\rangle_\beta$ direction for the quasi-α and atomic displacements on $\{112\}_\beta$ plane in $\langle 11\bar{1}\rangle_\beta$ direction for the quasi-ω. Due to these atomic displacements, the $\{110\}_\beta$ and $\{112\}_\beta$ planes become distorted, giving rise to the additional diffraction spots at the 1/2, the 1/3 and 2/3 diffraction positions of the β phase, the streaking of the β diffraction spots and the formation of extinction fringes in the TEM bright and dark field images. These results provide new insights into the structural nature of β phase in titanium alloys and its effect in electron diffraction and in microstructure.

(2) During the deformation at higher temperature in the α+β region, equiaxed or short rod shaped α precipitates (1~2μm) mainly form on the high angle grain boundaries and low angle grain boundaries but seldom in β grain interiors, forming a "necklace" microstructure. This is due to the formation of large amount of low angle and high angle boundaries

produced by dynamic recovery/recrystallization that provides abundant nucleation sites. The deformation and the subsequent recovery/recrystallization which happen in a continuous manner, destroys the BOR gradually between the α and β phases. The coherency of the α/β interfaces is reduced due to the different and uncoordinated lattice rotation at the β/β boundary parts and the β/α parts. The deviation from the BOR increases both with the increasing strain and decreasing strain rate.

(3) During the deformation at lower temperature in the α+β region, the α precipitates exhibit different morphologies, such as lamellar, equiaxed and irregular shapes. The microstructure evolution (micro bands, kinking, fragmentation or globularization) strongly depends on deformation parameters and the original orientation of the lamellae relative to the loading direction. Within the slip bands, equiaxed α and β grains do not respect BOR and 50~200nm in grain size are present. However, between the band, lamellar α and β phases, ~20 nm in width and maintain the strict BOR, are distributed alternately.

(4) A strong variant selection is observed during the deformation at lower temperature of the α+β region. When the BOR is respected, only two or three distinct α variants of the lamellar α form rather than the 12 α variants observed without deformation. This variant selection mechanism is dominated by the stress field. Only the variants that can accommodate the macroscopic deformation are selected.

(5) The phase transformation is retarded during the hot compression at higher temperature region, which was attributed to the competition of dynamic softening mechanism on phase transformation. On the contrary, it is promoted during compression at lower temperature region due to the more inducted deformation defects acting as α phase nucleation sites and due to accelerating growth of α precipitates and retarded softening. There is a competitive mechanism between softening and α phase transformation, which depends on the deformation. Due to the inverse temperature dependence of the two transformations, there could exist a transit temperature (T_{trans}), above which the driving force for phase transformation is smaller than that for softening and vice versa. This competition is not only

applicable for the deformation temperature but also strain and strain rate, which is not only found in the present work but also often observed in other hot deformed Ti alloys.

(6) Dislocation slip is leading deformation mechanism for the metastable β Ti-5553 alloy. Single or multiple-slip bands with two or three different propagating directions formed during the compression process. The slip bands are straighter and clearer at higher strain rate. Moreover, the bands widen gradually with increasing strain and the decreasnig strain rate. Further, it was possible to identify slip systems by trace analysis.

6.2 Future work

The following points may be addressed in the future work:

(1) The origin of the striation microstructure was first elucidated in the work, but its influence on the nucleation of α phase and on the final mechanical properties is not clear. The authors have observed a special distribution relationship between the striation and dislocations. Thus, the striation might produce an impact on the microstructural evolution and the final properties of the metastable β titanium alloy.

(2) All the thermo-mechanical treatments, have been performed with an initial single β microstructure in the present work. This initial microstructure plays an important role on phase development and other initial microstructures shall be studied as well.

(3) The thermo-mechanical path may be changed as well for example the effects of cooling during deformation may allow us to observe how the competition between softening and phase transformation change the microstructure.

(4) The dynamic phase transformation mechanism during hot deformation has not been well explored until now. However for this, in-situ examination is needed. Thermo dilatometer incorporated in synchrotron radiation will be pertinent facility and technique for in-situ investigation of phase transformation of metastable β titanium alloys during the hot deformation. In addition, HRTEM analysis on the interphase of α/β might be necessary to understanding the dynamic nucleation mechanism of α phase.

(5) The variant selection mechanism during deformation might be much more complicated and severely restricted by the nature of the defects such as grain boundaries, stacking faults and dislocations. Thus, the roles of the various defects on variant selection needs further study.

(6) Based on the accommodation strain concept and energy consumption principle, it is necessary to make detailed numerical simulation on local stress concentration and variant selection of α phase.

(7) As the present work shows, multiple-scaled microstructure could be gained after coupled thermo-mechanical treatments. Mechanical testing could be considered to establish the relation between microstructural evolution and mechanical properties of titanium alloys related to hot deformation parameters.

Bibliography

[1] G. Lütjering, J. Williams, Titanium (Engineering Materials and Processes). Berlin Heidelberg: Springer, 2007.
[2] www.webelements.com.
[3] G. Lutjering and J.C. Williams. Titanium. Springer-Verlag, 2003.
[4] E. W. Collings, Materials Properties Handbook. Titanium alloys, ASM International, Materials Park, 1994.
[5] H.W. Rosenberg, The Science, Technology and Application of Titanium, Pergamon Press, Oxford, UK. 851 (1970).
[6] P. J. Bania. Beta titanium alloys and their role in the titanium industry. JOM, 46 (1994) 16–19.
[7] P. J. Bania, Beta Titanium Alloys and Their Role in the Titanium Industry, in Beta Titanium Alloys in the 1990's, D. Eylon, R. R. Boyer, D. A Koss, eds., TMS, Warrendale, 1993.
[8] C. Leyens, M. Peters, Titanium and titanium alloys, Wiley Online Library, 2003.
[9] S. L. Raghunathan, A. M. Stapleton, R. J. Dashwood, M. Jackson, D. Dye, Micromechanics of Ti-10V-2Fe-3Al: In situ synchrotron characterisation and modeling, Acta Mater. 55 (2007) 6861–6872.
[10] R. Boyer, R. D. Briggs, The use of β titanium alloys in the aerospace industry, J. Mater. Eng. Perform. 14 (2005) 681–685.
[11] M. Jackson, R. Dashwood, L. Christodoulou, H.M. Flower, The microstructural evolution of near beta alloy Ti-10V-2Fe-3Al during subtransus forging, Metall. Mater. Trans. A. 36 (2005) 1317–1327.
[12] N. G. Jones, R. J. Dashwood, D. Dye, M. Jackson, Thermomechanical processing of Ti-5Al-5Mo-5V-3Cr, Mater. Sci. Eng. A. 490 (2008) 369–377.
[13] C. Roubaud, T. Grosdidier, M. Phillippe, Y. Combres, Titanium '95: Science and Technology. (Eds.: P. A. Blenkinsop, W. J. Evans, H. M. Flower), 996 (1996).
[14] V. N. Moiseev, Titanium '95: Science and Technology. (Eds.: P. A. Blenkinsop, W. J. Evans, H. M. Flower), 1387 (1996).
[15] S.Veeck, D. Lee, R. Boyer, R. Briggs, The castability of Ti-5553 alloy: Its microstructure and properties. Journal of advanced materials, 37 (2005) 40–45.
[16] N. Clément, A. Lenain, P. J. Jacques, Mechanical property optimization via microstructural control of new metastable beta titanium alloys. JOM, 59 (2007) 50–53.
[17] R. R. Boyer, Attributes, characteristics, and applications of titanium and its alloys. JOM, 62 (2010) 21–24.
[18] G. Tomchik, Overview of Titanium Applications on Advanced Commercial Transports, AeroMat Conference, unpublished research, 15 May 2006.

[19] N. G. Jones, R. J. Dashwood, D. Dye, M. Jackson, The flow behavior and microstructural evolution of Ti-5Al-5Mo-5V-3Cr during subtransus isothermal forging. Metall. Mater. Trans. A. 40 (2009) 1944–1954.

[20] An Update on Properties and Applications for Ti-5Al-5Mo-5V-3Cr, presented at the International Titanium Association, Scottsdale 2005, presented by VSMPO staff.

[21] S. L Nyakana, J. C. Fanning, R. R. Boyer, Quick reference guide for β titanium alloys in the 00s. Journal of materials engineering and performance, 14(6) (2005) 799–811.

[22] R. Panza-Giosa, The Effect of Heat Treatment on the Microstructure Evolution and Mechanical Properties of Ti-5Al-5V-5Mo-3Cr, and Its Potential Application in Landing Gears. McMaster University, 2009.

[23] B. Jiang, Effect of Severe Plastic Deformation on Microstructure in Metastable β-Ti Alloys. University of Tsukuba, 2015.

[24] J. K. Fan, J. S. Li, H. C. Kou, K. Hua, B. Tang, Y. D. Zhang. Microstructure and mechanical property correlation and property optimization of a near β titanium alloy Ti-7333. J. Alloy Compd. 682 (2016) 517–524.

[25] B. Appolaire, L. Héricher, E. Aeby-Gautier, Modelling of phase transformation kinetics in Ti alloys-Isothermal treatments. Acta Mater. 53(10) (2005) 3001–3011.

[26] Z. Sun, S. Guo, H. Yang, Nucleation and growth mechanism of α-lamellae of Ti alloy TA15 cooling from an α+β phase field. Acta Mater. 61(6) (2013) 2057–2064.

[27] J. K. Fan, J. S. Li, H. C. Kou, K. Hua, B. Tang, Y. D. Zhang. Influence of solution treatment on microstructure and mechanical properties of a near β titanium alloy Ti-7333. Mater. Design. 2015, 83: 499–507.

[28] J. K. Fan, J. S. Li, H. C. Kou, K. Hua, B. Tang. The Interrelationship of Fracture Toughness and Microstructure in a New Near β Titanium Alloy Ti-7Mo-3Nb-3Cr-3Al. Mater. Charact. 96 (2014) 93–99.

[29] C. Leyens, M. Peters, Titanium and Titanium Alloys, Fundamentals and Applications, Wiley, 2003.

[30] W. G. Burgers, On the process of transition of the cubic-body-centered modification into the hexagonal-close-packed modification of zirconium, Physica. 1 (1934) 561–586.

[31] S. Roy, S. Suwas, S. Tamirisakandala, et al. Mater. Sci. Eng. A. 540(0) (2012), 152–163.

[32] T. Furuhara, H. Nakamori, T. Maki, Chrystallography of a Phase Precipitated on Dislocations and Deformation Twin Boundaries in a β Titanium Alloy, Material Transactions, JIM, 33 (1992) 585–595.

[33] W. Pitsch, A. Schrader, Die Ausscheidungsform des ε-Karbids im Ferrit und im Martensit beim Anlassen. Archiv fur das Eisenhuttenwesen, 29 (1958) 715–721.

[34] D. I. Potter, The structure, morphology and orientation relationship of V3N in α-vanadium, Journal of the Less Common Metals. 31 (1973) 299–309.

[35] E. A. Brener, V. I. Mel'nikov, Pattern selection in two-dimensional dendritic growth.Adv. Phys. 40 (1991) 53–97.

[36] M. Fleck, C. Hüter, D. Pilipenko, R. Spatschek, E. A. Brener, Pattern formation during diffusion limited transformations in solids. Philos. Mag. 90 (2010) 265–286.

[37] C. Laird, H. Aaronson, The growth of γ plates in an Al-15% Ag alloy. Acta Metall. 17 (1969) 505–519.
[38] C. Zener, Theory of growth of spherical precipitates from solid solution. J. Appl. Phys. 20 (1949) 950–953.
[39] C. Laird, H. Aaronson, The growth of γ plates in an Al-15% Ag alloy. Acta Metall. 17 (1969) 505–519.
[40] H. Aaronson, C. Laird, K. Kinsman, Phase Transformations, ASM, Metals Park, (1970) 313–396.
[41] K. R. Kinsman, E. Eichen, H. I. Aaronson, Thickening kinetics of proeutectoid ferrite plates in Fe-C alloys. Metall. Trans. A. 6 (1975) 303–317.
[42] G. Spanos, R. Masumura, R. Vandermeer, M. Enomoto, The evolution and growth kinetics of precipitate plates growing by the ledge mechanism. Acta Metall. Mater. 42 (1994) 4165–4176.
[43] T. Furuhara, T. Ogawa, T. Maki, Atomic structure of interphase boundary of an a precipitate plate in a β Ti-Cr alloy. Philos. Mag. Lett. 72 (1995) 175–183.
[44] T. Furuhara, S. Takagi, H. Watanabe, T. Maki, Crystallography of grain boundary α precipitates in a β titanium alloy, Metall. Mater. Trans. A. 27 (1996) 1635–1646.
[45] S. M. C. Van Bohemen, A. Kamp, R. H. Petrov, L. A. I. Kestens, J. Sietsma, Nucleation and variant selection of secondary α plates in a β Ti alloy. Acta Mater. 56(20) (2008) 5907–5914.
[46] R. Shi, V. Dixit, H. L. Fraser, Y. Wang, Variant selection of grain boundary α by special prior β grain boundaries in titanium alloys. Acta Mater. 75 (2014) 156–166.
[47] R. Shi, V. Dixit, G. B. Viswanathan, H. L. Fraser, Y. Wang, Experimental assessment of variant selection rules for grain boundary α in titanium alloys. Acta Mater. 102 (2016) 197–211.
[48] G. C. Obasi, S. Birosca, D. L. Prakash, J. Q. da Fonseca, M. Preuss, The influence of rolling temperature on texture evolution and variant selection during α→β→α phase transformation in Ti-6Al-4V. Acta Mater. 60(17) (2012) 6013–6024.
[49] M. Salib, J. Teixeira, L. Germain, E. Lamielle, N. Gey, E. Aeby-Gautier, Influence of transformation temperature on microtexture formation associated with α precipitation at β grain boundaries in a β metastable titanium alloy. Acta Mater. 61(10) (2013) 3758–3768.
[50] R. Shi, Y. Wang, Variant selection during α precipitation in Ti-6Al-4V under the influence of local stress-A simulation study. Acta Mater. 61(16) (2013) 6006–6024.
[51] T. Furuhara, T. Maki, Variant selection in heterogeneous nucleation on defects in diffusional phase transformation and precipitation. Mater. Sci. Eng. A. 312(1) (2001) 145–154.
[52] A. Dehghan-Manshadi, R. J. Dippenaar, Strain-induced phase transformation during thermo-mechanical processing of titanium alloys, Mater. Sci. Eng. A. 552 (2012) 451–456.

[53] M. Klimova, S. Zherebtsov, G. Salishchev, S. L. Semiatin, Influence of deformation on the Burgers orientation relationship between the α and β phases in Ti-5Al-5Mo-5V-1Cr-1Fe. Mater. Sci. Eng. A. 645 (2015) 292–297.

[54] P. D. Frost, W. M. Parris, L. L. Hirsch, J. R. Doig, C. M. Schwartz, Isothermal transformation of titanium-chromium alloys, Trans. ASM. 46 (1954) 231–256.

[55] F. Prima, P. Vermaut, G. Texier, D. Ansel, T. Gloriant, Evidence of α-nanophase heterogeneous nucleation from ω particles in a β-metastable Ti-based alloy by high-resolution electron microscopy, Scripta Mate. 54 (2006) 645–648.

[56] Y. Ohmori, T. Ogo, K. Nakai, S. Kobayashi, Effects of ω-phase precipitation on β→α, α″ transformations in a metastable β titanium alloy, Mater. Sci. Eng. A. 312 (2001) 182–188.

[57] S. Nag, R. Banerjee, R. Srinivasan, J. Y. Hwang, M. Harper, H. L. Fraser, X-Assisted nucleation and growth of a precipitates in the Ti-5Al-5Mo-5V-3Cr-0.5Fe β titanium alloy, Acta Mater. 57 (2009) 2136–2147.

[58] T. S. Kuan, R. R. Ahrens, S. L. Sass, The stress-induced omega phase transformation in Ti-V alloys. Metallurgical Transactions A, 6(9) (1975) 1767–1774.

[59] H. Xing, J. Sun, Mechanical twinning and omega transition by<111>{112} shear in a metastable beta titanium alloy. Appl. Phys. Lett. 93 (2008) 1903–1908.

[60] F. Sun, J. Y. Zhang, M. Marteleur, T. Gloriant, P. Vermaut, D. Laillé, P. Castany, C. Curfs, P. J. Jacques, F. Prima, Investigation of early stage deformation mechanisms in a metastable β titanium alloy showing combined twinning-induced plasticity and transformation-induced plasticity effects. Acta Mater. 61 (2013) 6406–6417.

[61] S. Banerjee, R. Tewari, G. Dey, Z. Metallkd. Omega phase transformation–morphologies and mechanisms: Dedicated to Professor Dr. Knut Urban on the occasion of his 65th birthday. Zeitschrift für Metallkunde, 97 (2006) 963–977.

[62] S. K. Sikka, Y. K. Vohra, R. Chidambaram, Omega phase in materials, Prog. Mater. Sci. 27 (1982) 245–310.

[63] M. Ahmed, T. Li, G. Casillas, J. M. Cairney, D. Wexler, E. V. Pereloma, The evolution of microstructure and mechanical properties of Ti-5Al-5Mo-5V-2Cr-1Fe during ageing, J. Allo Compd. 629 (2015) 260–273.

[64] D. De Fontaine, Simple models for the omega phase transformation, Metall. Trans. A. 19 (1988) 169–175.

[65]] Y. A. Bagariatskii, G. I. Nosova, T. V. Tagunova, Crystallographic Structure and Properties of Omega Phase in Titanium Chrome Alloys, InDokl. Akad. Nauk SSSR. 105 (1955) 1225.

[66] J. M. Silcock, M. H. Davies, H. K. Hardy, The mechanism of phase transformations in solids, In A symposium, Monograph and Report Series No. 18, Inst. of Metals London. 93 (1956).

[67] D. De Fontaine, N.E. Paton, J.C. Williams, The omega phase transformation in titanium alloys as an example of displacement controlled reactions, Acta Metallurgica. 19 (1971) 1153–1162.

[68] H. Y. Kim, Y. Ikehara, J. I. Kim, H. Hosoda, S. Miyazaki, Martensitic transformation, shape memory effect and superelasticity of Ti–Nb binary alloys. Acta Mater. 54 (2006) 2419–2429.

[69] K. A. Bywater, J. W. Christian, Martensitic Transformations in Titanium-Tantalum Alloys. Philosophical Magazine, 25(6) (1972) 1249–1273.

[70] A. V. Dobromyslov, V. A. Elkin, Martensitic transformation and metastable beta-phase in binary titanium alloys with d-metals of 4-6 periods. Journal De Physique Iv, 112 (2003) 723–726.

[71] R. Davis, H. M. Flower, D. R. F. West, Martensitic Transformations in Ti-Mo Alloys. J. Mater. Sci. 14 (1979) 712–722.

[72] T. W. Duerig, R. M. Middleton, G. T. Terlinde, J. C. Williams. Stress Assisted Transformation in Ti-10V-2F3-3Al. The Fourth International Conference on Titanium, Kyoto, Japan. The Metallurgical Society of AIME, (1980) 1503–1512.

[73] E. W. Collings, The Physical Metallurgy of Titanium Alloys, American Society for Metals, 1984.

[74] T. W. Duerig, J. C. Williams, Beta Titanium alloys in the 80's: proceedings of the symposium, Atlanta, GA, United States. (1984) 19–67.

[75] S. Banerjee, P. Mukhopadhyay, Phase Transformations Examples from Titanium and Zirconium Alloys. Elsevier, 2007.

[76] S. Nag, Influence of β Instabilities on the Early Stages of Nucleation and Growth of α in β Titanium Alloys, in Materials Science and Engineering. The Ohio State University, 2008.

[77] D. Porter, K. Easterling, Phase transformations in metals and alloys. CRC, 2000.

[78] T. Furuhara, T. Maki, T. Makino, Microstructure control by thermomechanical processing in β-Ti-15-3 alloy, J. Mater. Process. Technol. 117 (2001) 318–323.

[79] J. Huang, Z. Wang, J. Zhou, Cyclic Deformation Response of β-Annealed Ti-5Al-5V-5Mo-3Cr Alloy Under Compressive Loading Conditions, Metall. Mater. Trans. A. 42 (2011) 2868–2880.

[80] S. V. Zherebtsov, M. A. Murzinova, M. V. Klimova, G. A. Salishchev, A. A. Popov, S. L. Semiatin, Microstructure evolution during warm working of Ti-5Al-5Mo-5V-1Cr-1Fe at 600 and 800°C, Mater. Sci. Eng. A. 563 (2013) 168–176.

[81] P. Barriobero-Vila, G. Requena, S. Schwarz, F. Warchomicka, T. Buslaps, Influence of phase transformation kinetics on the formation of α in a β-quenched Ti-5Al-5Mo-5V-3Cr-1Zr alloy, Acta Mater. 95 (2015) 90–101.

[82] A. Hall, Primary processing of beta and near beta titanium alloys, Beta Titanium Alloys in the 1980's, (1984) 129–143.

[83] H. M. Flower, Microstructural Development in Relation to Hot Working of Titanium Alloys, Mater. Sci. Technol. 6 (1990) 1082–1092.

[84] D. L. Bourell H. J. McQueen, Thermomechanical Processing of Iron, Titanium and Zirconium Alloys in the BCC Structure, J. Mater. Shaping Technol. 5 (1987) 53–73.

[85] J. K. Fan, H. C. Kou, M. J. Lai, B. Tang, H. Chang, J. S. Li. Characterization of Hot Deformation Behavior of a New Near Beta Titanium Alloy Ti-7333. Mater. Design. 49 (2013) 945–952.

[86] C. M. Sellars, W. J. Tegart. On the mechanism of hot deformation. Acta Metall. 14 (1966) 1136–1138.

[87] F. J. Humphreys, M. Hatherly, Recrystallization and Related Annealing Phenomena. London: Elsevier Science Ltd, 2004.

[88] D. G. Cram, H. S. Zurob, Y. J. M. Brechet, C. R. Hutchinson, Modelling discontinuous dynamic recrystallization using a physically based model for nucleation, Acta Mater., 57 (2009) 5218–5228

[89] S. Gourdet, F. Montheillet, A model of continuous dynamic recrystallization, Acta Mater. 51 (2003) 2685–2699

[90] S. Gourdet, F. Montheillet, An experimental study of the recrystallization mechanism during hot deformation of aluminium, Mater. Sci. Eng. A. 283 (1-2) (2000) 274–288.

[91] J. K. Fan, H. C. Kou, M. J. Lai, B. Tang, H. Chang, J. S. Li. Hot Deformation Mechanism and Microstructure Evolution of a New Near β Titanium Alloy. Mater. Sci. Eng. A. 584 (2013) 121–132.

[92] F. Warchomicka, C. Poletti, M. Stockinger, et al., Mater. Sci. Eng. A 528 (28) (2011) 8277–8285.

[93] S. Zherebtsov, M. Murzinova, G. Salishchev, S. L. Semiatin, Spheroidization of the lamellar microstructure in Ti-6Al-4V alloy during warm deformation and annealing. Acta Mater. 59(10) (2011) 4138–4150.

[94] S. Roy, S. Suwas, The influence of temperature and strain rate on the deformation response and microstructural evolution during hot compression of a titanium alloy Ti-6Al-4V-0.1B. J. Allo Compd. 548(0) (2013) 110–125.

[95] N. Stefansson, S. L. Semiatin, Mechanisms of globularization of Ti-6Al-4V during static heat treatment. Metall. Mater. Trans. A. 34(3) (2003) 691–698.

[96] M. Cabibbo, S. Zherebtsov, S. Mironov, G. A. Salishchev, Loss of coherency and interphase α/β angular deviation from the Burgers orientation relationship in a Ti-6Al-4V alloy compressed at 800°C. J. Mater. Sci. 48(3) (2013) 1100–1110.

[97] T. R. Bieler, S. L. Semiatin, The origins of heterogeneous deformation during primary hot working of Ti-6Al-4V. International Journal of Plasticity, 18(9) (2002). 1165–1189.

[98] L. Germain, N. Gey, M. Humbert, P. Bocher, M. Jahazi, Analysis of sharp microtexture heterogeneities in a bimodal IMI 834 billet. Acta Mater. 53(13) (2005) 3535–3543.

[99] T. Grosdidier, C. Roubaud, M. J. Philippe, Y. Combres. The deformation mechanisms in the β-metastable β-Cez titanium alloy. Scripta Mater. 36 (1997) 21–28.

[100] D. Banerjee, J. C. Williams, Perspectives on titanium science and technology. Acta Mater. 61(3) (2013) 844–879.

[101] S. Hanada, M. Ozeki, O. Izumi, Deformation characteristics in B phase Ti-Nb alloys. Metallurgical Transactions A, 16(5) (1985) 789–795.

[102] S. Hanada, O. Izumi, Transmission electron microscopic observations of mechanical twinning in metastable beta titanium alloys. Metallurgical Transactions A, 17(8) (1986) 1409–1420.

[103] S. Hanada, O. Izumi, Deformation and Fracture of Metastable Beta Titanium Alloys (Ti-15Mo-5Zr and Ti-15Mo-5Zr-3Al). Transactions of the Japan Institute of Metals, 23 (1982) 85–94.

[104] Z. Wyatt, S. Ankem, The effect of metastability on room temperature deformation behavior of β and α+ β titanium alloys. J. Mater. Sci. 45 (2010) 5022–5031.

[105] W. Xu, K. B. Kim, J. Das, M. Calin, J. Eckert. Phase stability and its effect on the deformation behavior of Ti-Nb-Ta-In/Cr β alloys.Scripta Mater. 54 (2006) 1943–1948.

[106] D. Doraiswamy, S. Ankem. The effect of grain size and stability on ambient temperature tensile and creep deformation in metastable beta titanium alloys. Acta Mater. 51 (2003) 1607–1619.

[107] A. G. Paradkar, S. V. Kamat, A. K. Gogia, B. P. Kashyap, Various stages in stress–strain curve of Ti-Al-Nb alloys undergoing SIMT. Mater. Sci. Eng. A. 456(1) (2007) 292–299.

[108] A. Paradkar, S. V. Kamat, A. K. Gogia B. P. Kashyap, Effect of Al and Nb on the trigger stress for stress-induced martensitic transformation during tensile loading in Ti-Al-Nb alloys. Mater. Sci. Eng. A. 487(1) (2008) 14–19.

[109] Y. Liu, H. Xiang, Apparent modulus of elasticity of near-equiatomic NiTi. J. Allo Compd. 270(1) (1998) 154–159.

[110] X. H. Min, S. Emura, K. Tsuchiya, T. Nishimura, K. Tsuzaki, Transition of multi-deformation modes in Ti-10Mo alloy with oxygen addition. Mater. Sci. Eng. A. 590 (2014) 88–96.

[111] G. Welsch, R. Boyer, E. W. Collings, Materials properties handbook: titanium alloys. ASM international. 1994.

[112] S. Hanada, O. Izumi, Correlation of tensile properties, deformation modes, and phase stability in commercial β-phase titanium alloys. Metallurgical Transactions A, 18(2) (1987) 265–271.

[113] R. Prakashkolli, W. Jjoost, S. Ankem, Phase Stability and Stress-Induced Transformations in Beta Titanium Alloys. JOM, 67(6) (2015) 1273–1280.

[114] V. Petříček, M. Dušek, L. Palatinus, Crystallographic computing system JANA2006: general features. Zeitschrift für Kristallographie-Crystalline Materials, 229(5) (2014). 345–352.

[115] A. Morawiec, Automatic orientation determination from Kikuchi patterns, J. Appl. Crystallogr. 32 (1999) 788–798.

[116] A. Morawiec, J. J. Fundenberger, E. Bouzy, J. S. Lecomte, EP–a program for determination of crystallite orientations from TEM Kikuchi and CBED diffraction patterns, J. Appl. Crystallogr. 35 (2002) 287–287.

[117] H. J. Bunge, C. Esling, J. Muller, The influence of crystal and sample symmetries on the orientation distribution function of the crystallites in polycrystalline materials, Acta Crystallogr. A. 37 (1981) 889–899.

[118] H. J. Bunge, C. Esling, J. Muller, The role of the inversion centre in texture analysis, Journal of Applied Crystallography, 13 (1980) 544–554.
[119] H. J. Bunge, Texture analysis in materials science-mathematical methods. ,Gottingen: Cuvillier Press, (1993) 1–593.
[120] B. Yang, Fabrication and crystallographic features ofepitaxial NiMnGaferromagnetic shape memory alloy thin films. Ph. D thesis. 2014, Université de Lorraine.
[121] M. Humbert, F. Wagner, H. Moustahfid, C. Esling, Determination of the Orientation of a Parent β Grain from the Orientations of the Inherited α Plates in the Phase Transformation from Body-Centred Cubic to Hexagonal Close Packed, Journal of Applied Crystallography, , 28 (1995) 571–576.
[122] Y. Zhang, S. Wang, C. Esling, J. S. Lecomte, C. Schuman, X. Zhao, L. Zuo, A method to identify dislocations in a known crystal structure by transmission electron microscopy, J. Appl. Crystallogr. 44 (2011) 1164–1168.
[123] http://www.mediacy.com.cn/cn/index/index.asp.
[124] http://www.crystalmaker.com/software/index.html.
[125] http://www.mathworks.com/products.
[126] H. Tobe, H. Y. Kim, T. Inamura, H. Hosoda, S. Miyazaki, Origin of {332} twinning in metastable β-Ti alloys, Acta Mater. 64 (2014) 345–355.
[127] Y. Al-Zain, Y. Sato, H. Y. Kim, H. Hosoda, T. H. Nam, S. Miyazaki, Room temperature aging behavior of Ti–Nb–Mo-based superelastic alloys, Acta Mater. 60 (2012) 2437–2447.
[128] M. J. Lai, C. C. Tasan, D. Raabe, Deformation mechanism of ω-enriched Ti–Nb-based gum metal: Dislocation channeling and deformation induced ω–β transformation, Acta Mater. 100 (2015) 290–300.
[129] Y. Chen, B. Tang, G. Xu, C.Y. Wang, H.C. Kou, J.S. Li, Y.W. Cui, Diffusion Research in BCC Ti-Al-Mo Ternary Alloys, Metall. Mater. Trans. A. 45 (2014) 1647–1652.
[130] P. Laheurte, A. Eberhardt, M. J. Philippe, Influence of the microstructure on the pseudoelasticity of a metastable beta titanium alloy, Mater. Sci. and Eng. A. 396 (2005) 223-230.
[131] S. Zaefferer, R. A. Schwarzer, Microstructure and Local Texture of Partially Recrystallized Titanium Sheet, Mater. Sci. Forum. 113 (1993) 721–724.
[132] L. Lu, X. Chen, X. Huang, K. Lu, Revealing the maximum strength in nanotwinned copper, Science. 323 (2009) 607–610.
[133] D. Phelan, M. Reid, N. Stanford, R. Dippenaar, In-situ observations of phase transformations in titanium, JOM. 58 (2006) 67–69.
[134] L. E. Tanner, Diffraction contrast from elastic shear strains due to coherent phases, Philos. Mag. 14 (1966) 111–130.
[135] K. Inaekyan, V. Brailovski, S. Prokoshkin, V. Pushin, S. Dubinskiy, V. Sheremetyev, Comparative study of structure formation and mechanical behavior of age-hardened Ti-Nb-Zr and Ti-Nb-Ta shape memory alloys, Mater. Charact. 103 (2015) 65–74.

[136] W. G. Burgers, On the process of transition of the cubic-body-centered modification into the hexagonal-close-packed modification of zirconium, Physica. 1 (1934) 561–586.
[137] I. M. Robertson, C. M. Wayman, Tweed microstructures I. Characterization in β-NiAl, Philos. Mag. A. 48 (1983) 421–442.
[138] J. W. Edington, Practical Electron Microscopy in Materials Science, Monograph 3: Interpretation of Transmission Electron Micrographs, Macmillan Press. (1975).
[139] N. G. Jones, R. J. Dashwood, D. Dye, M. Jackson, Understanding the behavior of Ti-5Al-5Mo-5V-3Cr during subtransus isothermal forging, Ti-2011, Proceedings of the 12th World Conference on Titanium, Ⅰ (2011) 226–230.
[140] S. Suri, G. B. Viswanathan, T. Neeraj, D. H. Hou, M. J. Mills, Room temperature deformation and mechanisms of slip transmission in oriented single-colony crystals of an α/β titanium alloy, Acta Mater. 47 (1999) 1019–1034.
[141] S. Zherebtsov, G. Salishchev, S. L. Semiatin, Loss of coherency of the alpha/beta interface boundary in titanium alloys during deformation, Phil. Mag. Lett. 90 (12) (2010) 903–914.
[142] D. He, J. C. Zhu, S. Zaefferer, D. Raabe, Y. Liu, Z. L. Lai, X. W. Yang, Influences of deformation strain, strain rate and cooling rate on the Burgers orientation relationship and variants morphology during β→α phase transformation in a near α titanium alloy. Mater. Sci. and Eng. A. 549 (2012) 20–29.
[143] O. M. Ivasishin, P. E. Markovsky, Y. V. Matviychuk, S. L. Semiantin, Precipitation and RecrystellizationBehavior of Beta TitaniumAlloys during Continuous Heat Treatment, Metall. Mater. Trans. A, 34 (2003) 147–158.
[144] H. S. Zurob, Y. Brechet, G. Purdy, A model for the competition of precipitation and recrystallization in deformed austenite. Actamaterialia, 49(20) (2001) 4183–4190.
[145] C. Poletti, L. Germain, F. Warchomicka, M. Dikovits, S. Mitsche, Unified description of the softening behavior of beta-metastable and alpha+beta titanium alloys during hot deformation. Mater. Sci. and Eng. A. 651 (2016) 280–290.
[146] C. Sauer, G. Luetjering, Thermo-mechanical processing of high strength β-titanium alloys and effects on microstructure and properties. Journal of materials processing technology, 117(3) (2001) 311–317.
[147] H. Matsumoto, M. Kitamura, Y. Li, Y. Koizumi, A. Chiba, Hot forging characteristic of Ti-5Al-5V-5Mo-3Cr alloy with single metastable β microstructure. Mater. Sci. and Eng. A. 611 (2014) 337–344.
[148] T. Furuhara, J. M. Howe, H. I. Aaronson, Interphase boundary structures of intragranular proeutectoid α plates in a hypoeutectoid Ti-Cr alloy. Acta metallurgica et materialia, 39(11) (1991) 2873–2886.
[149] G. G. E. Seward, S. Celotto, D. J. Prior, J. Wheeler, R. C. Pond, In situ SEM-EBSD observations of the hcp to bcc phase transformation in commercially pure titanium. Acta Mater. 52(4) (2004) 821–832.
[150] L. Germain, N. Gey, M. Humbert, Reliability of reconstructed β-orientation maps in titanium alloys. Ultramicroscopy, 107(12) (2007) 1129–1135.

[151] Q. Chao, P. D. Hodgson, H. Beladi, Ultrafine grain formation in a Ti-6Al-4V alloy by thermomechanical processing of a martensitic microstructure. Metall. Mater. Trans. A. 45(5) (2014) 2659–2671.

[152] Y. Xu, J. Zhang, Y. Bai, M. A. Meyers, Shear localization in dynamic deformation: microstructural evolution. Metall. Mater. Trans. A. 39(4) (2008) 811–843.

[153] S. L. Semiatin, D.U. Furrer, Fundamentals of modeling for metals processing, ASM Handbook, ASM International, Materials Park, Ohio, (2009) 536–552.

List of Publications

I. Publications in international journals

1. **J. K. Fan**, H. C. Kou, M. J. Lai, B. Tang, H. Chang, J. S. Li. Hot Deformation Mechanism and Microstructure Evolution of a New Near β Titanium Alloy. **Materials Science and Engineering: A.** 2013. 584, 121–132.
2. **J. K. Fan**, H. C. Kou, M. J. Lai, B. Tang, H. Chang, J. S. Li. Characterization of Hot Deformation Behavior of a New Near Beta Titanium Alloy Ti-7333. **Materials & Design**. 2013. 49, 945–952.
3. **J. K. Fan**, H. C. Kou, M. J. Lai, B. Tang, H. Chang, J. S. Li. High Temperature Discontinuous Yielding in a New Near β Titanium Alloy Ti-7333. **Rare Metal Material and Engineering**. 2014, 43(4): 808-812.
4. **J. K. Fan**, J. S. Li, H. C. Kou, K. Hua, B. Tang. The Interrelationship of Fracture Toughness and Microstructure in a New Near β Titanium Alloy Ti-7Mo-3Nb-3Cr-3Al. **Materials Characterization**. 2014, 96: 93–99.
5. **J. K. Fan**, J. S. Li, H. C. Kou, K. Hua, B. Tang, Y. D. Zhang. Influence of solution treatment on microstructure and mechanical properties of a near β titanium alloy Ti-7333. **Materials & Design**, 2015, 83: 499-507.
6. **J. K. Fan**, J. S. Li, H. C. Kou, K. Hua, B. Tang, Y. D. Zhang. Microstructure and mechanical property correlation and property optimization of a near β titanium alloy Ti-7333. **Journal of Alloys and Compounds**. 2016, 682: 517–524.
7. **J. K. Fan**, H. C. Kou, M. J. Lai, B. Tang, H. Chang, J. S. Li. Relationship between Fracture Toughness and Microstructure of a New Near β Titanium Alloy. In PRICM: 8 Pacific Rim International Congress on Advanced Materials and Processing (pp. 3371-3378). John Wiley & Sons, Inc. 2013.
8. **J. K. Fan**, J. S. Li, Y. D. Zhang, H. C. Kou, J. Ghanbaja, W. M. Gan, L. Germain, C. Esling. Distortion induced striations in β phase in metastable β titanium alloy. **Journal of Applied Crystallography**. Under review.
9. H. C. Kou, X. Zhang, **J. K. Fan**, M. J. Lai, B. Tang, H. Chang, J. S Li. The Precipitation Behavior of α Phase in a New Near β Titanium Alloy Ti‐7333 during Aging Process. In PRICM: 8 Pacific Rim International Congress on Advanced Materials and Processing (pp. 1175-1182). John Wiley & Sons, Inc. 2013.
10. H. C. Kou, K. Hua, **J. K. Fan**, B. Tang, J. S. Li, Characterization of α Phase in A Near β Titanium Alloy Ti-7Mo-3Nb-3Cr-3Al During Hot Deformation. In Proceedings of the 13th World Conference on Titanium (pp. 775-778). John Wiley & Sons, Inc. 2015.

11. K. Hua, X. Y. Xue, H. C. Kou, **J. K. Fan**, B. Tang, J. S. Li. High temperature deformation behaviour of Ti-5Al-5Mo-5V-3Cr during thermomechanical processing. **Materials Research Innovations**. 2014 18(S4), 202-206.
12. K. Hua, X. Y. Xue, H. C. Kou, **J. K. Fan**, B. Tang, J. S. Li. Characterization of hot deformation microstructure of a near beta titanium alloy Ti-5553. **Journal of Alloys and Compounds**. 2014, 615: 531-537.
13. K. Hua, J. S. Li, H. C. Kou, **J. K. Fan**, M. Sun, B. Tang. Phase precipitation behavior during isothermal deformation in β-quenched near beta titanium alloy Ti-7333. **Journal of Alloys and Compounds**. 2016, 671, 381-388.

II. Contributions to International Conferences

1. **J. K. Fan**, H. C. Kou, M. J. Lai, B. Tang, H. Chang, J. S. Li. *Relationship between Fracture Toughness and Microstructure of a New Near β Titanium Alloy*. **8th Pacific Rim International Congress on Advanced Materials and Processing (PRICM)**. 08. 2013, Hawaii, USA. (**Oral presentation**)
2. H. C. Kou, K. Hua, **J. K. Fan**, B. Tang, J. S. Li. *The characteristic of α phase in Ti-5Al-5Mo-5V-3Cr alloy during thermomechanical processing.* **12th IUMRS International Conference on Advanced Materials (IUMRS-ICAM)**. 09. 2013, Qingdao, China. (**Oral presentation**)
3. Y. D. Zhang, **J. K. Fan**, J. S. Li, H. C. Kou, J. Ghanbaja, L. Germain, Claude Esling. *Identification of pre-transformations of beta phase in metastable beta titanium alloy.* **THERMEC 2016 International Conference on Processing and Manufacturing of Advanced Materials Processing, Fabrication, Properties, Applications**. 05. 2016, Graz, Austria. (**Invited lecture**)